Title
Mass, Spin, and Physics Beyond the Standard Model at Colliders

Author
Klemm, William Lathrop

Publication Date
2011

Peer reviewed|Thesis/dissertation

Mass, Spin, and Physics Beyond the Standard Model at Colliders

by

William Lathrop Klemm

A dissertation submitted in partial satisfaction of the
requirements for the degree of
Doctor of Philosophy

in

Physics

in the

GRADUATE DIVISION
of the
UNIVERSITY OF CALIFORNIA, BERKELEY

Committee in charge:
Professor Hitoshi Murayama, Chair
Professor Lawrence Hall
Professor Alexei Filippenko

Spring 2011

Mass, Spin, and Physics Beyond the Standard Model at Colliders

William Lathrop Klemm

Abstract

Mass, Spin, and Physics Beyond the Standard Model at Colliders

by

William Lathrop Klemm

Doctor of Philosophy in Physics

University of California, Berkeley

Professor Hitoshi Murayama, Chair

The Standard Model of particle physics has thus far proven extremely effective at describing the composition and interactions of matter we observe. However, theoretical considerations, such as the large hierarchy between the weak and Planck scales, and experimental evidence, such as the observation of non-baryonic dark matter, suggest the possibility of new physics beyond the Standard Model (BSM). In many scenarios, such new physics would occur around the TeV scale, and therefore has an excellent chance of being seen at current and future collider experiments.

Following a review of the standard model, its problems, and some new physics scenarios, we explore a number of ways in which colliders may be used to study such new physics. We first discuss a technique for determining the masses of new particles in single-step decay chains, a task which is typically complicated by missing energy associated with discrete symmetries prevalent in BSM models. We then address the determination of the spins of new particles at colliders, developing a model-independent technique and demonstrating how it could be used to distinguish two specific models, supersymmetry and universal extra dimensions, at a future linear collider. We further demonstrate that the effectiveness of this technique could be realized experimentally using existing data from both e^+e^- and hadron colliders. Finally, we turn away from model-independent techniques and propose a search for color sextet scalars, which could be copiously produced at the Large Hadron Collider. Pair production of such particles could potentially be seen in the relatively clean same-sign dilepton + jets + missing energy channel, for which we propose an effective reconstruction of the sextet pair.

Contents

Acknowledgments

I would like to thank my parents and siblings, who have always been supportive throughout my education and understanding of my stay far from home.

I would also like to thank my adviser Hitioshi Murayama, who is a great teacher and gave me wonderful opportunities. Thanks also to all of my collaborators and the scientific staff at IPMU, especially Kai Wang and Jason Evans, who always found time for interesting discussions. I greatly appreciate the support I received from my coursemates and housemates in Berkeley.

Many people have been extremely helpful in helping me survive in Japan, especially Yuuko Enomoto, Hisami Kuboshima, Takeshi Kobayashi, and Fuminobu Takahashi. I would also like to thank Daniel Perley, Victor Acosta, Benjamin Hagenhofer-Daniell, and Christie Toth for their visits.

Finally, I would like to thank Chiew Yoon Lin for her care, company, and support.

Chapter 1

Introduction

The standard model (SM) of particle physics has been one of the great successes of theoretical physics and has withstood the rigors of extensive experimental testing. However, an increasing number of questions are proving to be beyond the scope of the SM. Some of these are observational, such as the nature of the dark matter which accounts for a large fraction of the energy in our universe. Theoretical considerations, such as the large hierarchy between the gravitational and electroweak scales, also remain unsolved puzzles. A vast array of theoretical scenarios have been formulated to deal with these issues, and many of them predict new physics at the TeV scale, which is currently being probed at the CERN Large Hadron Collider (LHC). This thesis presents a number of novel techniques for studying such new physics at collider experiments.

In this introduction, Section 1.1 provides a brief review the SM and electroweak symmetry breaking. Section 1.2 then discusses two of the major shortcomings of the SM – the hierarchy problem and non-baryonic dark matter – and demonstrates the connection between these questions and the TeV scale. Finally, Section 1.3 discusses two scenarios of physics beyond the standard model (BSM), supersymmetry and extra dimensions, and how they relate to the aforementioned questions. In each case, a new symmetry is introduced which produces a dark matter candidate and has important phenomenological implications.

Producing new particles at a collider is only useful if we are able to relate the data to the properties of those particles, and therefore the underlying theory. One of the most basic properties of any particle is its mass, knowledge of which is useful not only for understanding the underlying model, but also for performing event reconstruction in other analyses. Mass measurement may be complicated in many BSM scenarios by stable particles (usually a dark matter candidate) which go unseen in the detector. Chapter 2 discusses a new method for mass measurement in such cases for certain event topologies. The effectiveness of this technique is demonstrated for a particular supersymmetric model, but the method is generally applicable to many BSM models.

Determining the masses of new particles is an important step, but as we elaborate in Section 1.3, determination of spins can play an important role in differentiating BSM models. Chapters 3 and 4 present a novel, model-independent technique for measuring parti-

cle spins. Chapter 3 introduces this technique and demonstrates its ability to distinguish between models (comparing supersymmetry with universal extra dimensions for concreteness) at a future linear collider. Further support for the efficacy of this technique is presented in Chapter 4, which demonstrates that it may be implemented using existing data from both lepton and hadron colliders to determine the spins of weak gauge bosons.

Identifying channels where new physics may appear and determining how best to use data from those channels is also important for BSM studies at colliders. This approach is taken in Chapter 5, which considers pair production of color sextet scalars. Such new particles, which are not present in the standard model, appear in a number of theories, including unification schemes, and could be produced in large numbers at the LHC if present at the TeV scale. After a brief review of color sextet scalars, a search channel and reconstruction scheme for the LHC are presented.

The conclusions of this thesis are summarized in Chapter 6.

1.1 The Standard Model

The standard model is constructed by selecting a set of gauge symmetries under which the Lagrangian must remain locally invariant. The matter content is then specified and assigned charges under the gauge groups, and the interactions of those particles are defined by writing down all possible renormalizable terms which respect the symmetries of the theory.

Experimental observation has led us to the fermionic particle content and charge assignments shown in Table 1.1, with interactions governed by the gauge group $SU(3)_C \times SU(2)_L \times U(1)_Y$. With each symmetry comes an associated gauge field, denoted G^a_μ, W^i_μ, and B_μ, respectively. Each fermion apparently comes in three generations. Of the fermions, only the quarks are charged under the color $SU(3)$ symmetry; together, the quarks and gluons compose the very successful theory of chromodynamics. Only the left-handed fermions are charged under the $SU(2)_L$ symmetry, which has the effect of forbidding bare fermion mass terms in the Lagrangian. Their masses can be generated when the scalar Higgs field, $\phi = \binom{\phi^+}{\phi^0}$, an $SU(2)_L$ doublet with weak hypercharge $y_\phi = 1/2$, acquires a vacuum expectation value (vev) at low energies (see Section 1.1.2), spontaneously breaking the SM symmetry to $SU(3)_C \times U(1)_{EM}$. In this section we describe the details of the SM Lagrangian and the consequences of spontaneous symmetry breaking of the electroweak theory.

1.1.1 The Standard Model Lagrangian

Here we describe the SM Lagrangian as a sum of four parts,

$$\mathcal{L}_{SM} = \mathcal{L}_f + \mathcal{L}_{\text{gauge}} + \mathcal{L}_\phi + \mathcal{L}_{\text{Yuk.}}, \tag{1.1}$$

where the fermionic kinetic term is $\mathcal{L}_f$, the Yang-Mills terms for gauge fields $\mathcal{L}_{\text{gauge}}$, the Higgs term $\mathcal{L}_\phi$, and the Yukawa interactions between fermionic and Higgs fields $\mathcal{L}_{\text{Yuk.}}$. The

Name	$SU(3)_C$	$SU(2)_L$	$U(1)_Y$
$Q_i = \binom{u}{d}_L, \binom{c}{s}_L, \binom{t}{b}_L$	**3**	**2**	$+1/6$
$\bar{u}_i = u_R^c, c_R^c, t_R^c$	$\bar{\mathbf{3}}$	**1**	$-2/3$
$\bar{d}_i = d_R^c, s_R^c, b_R^c$	$\bar{\mathbf{3}}$	**1**	$+1/3$
$L_i = \binom{\nu_e}{e}_L, \binom{\nu_\mu}{\mu}_L, \binom{\nu_\tau}{\tau}_L$	**1**	**2**	$-1/2$
$\bar{e}_i = e_R^c, \mu_R^c, \tau_R^c$	**1**	**1**	$+1$

Table 1.1: Fermionic content of the SM, listed as left-handed Weyl spinors.

first is given by

$$\mathcal{L}_f = \sum_j \bar{\psi}_{j\alpha} i \not{D}^\alpha_\beta \psi^\beta_j, \tag{1.2}$$

where the sum j is over all fermions (given in Table 1.1); a sum over $SU(3) \times SU(2)$ gauge numbers, α and β, is implied. The gauge covariant derivative is given by

$$D^\beta_{\mu\alpha} = \partial_\mu \delta^\beta_\alpha + i g_s G^a_\mu (T^a)^\beta_\alpha + i g W^i_\mu (T^i)^\alpha_\beta - i g' Y B_\mu \delta^\alpha_\beta, \tag{1.3}$$

where T^a and T^i denote the generators of the $SU(3)$ and $SU(2)$ groups, respectively. This term describes the propagation of fermions as well as their interactions with gauge fields.

The gauge fields each contribute a Yang-Mills term to the Lagrangian,

$$\mathcal{L}_{\text{gauge}} = -\frac{1}{4} G^a_{\mu\nu} G^{\mu\nu a} - \frac{1}{4} W^i_{\mu\nu} W^{\mu\nu i} - \frac{1}{4} B_{\mu\nu} B^{\mu\nu}, \tag{1.4}$$

where their field strength tensors are given by

$$\begin{aligned} G^a_{\mu\nu} &= \partial_\mu G^a_\nu - \partial_\nu G^a_\mu - g_s f_{abc} G^b_\mu G^c_\nu, \\ W^i_{\mu\nu} &= \partial_\mu W^i_\nu - \partial_\nu W^i_\mu - g \epsilon_{ijk} W^j_\mu W^k_\nu, \\ B_{\mu\nu} &= \partial_\mu B_\nu - \partial_\nu B_\mu. \end{aligned} \tag{1.5}$$

The self interactions of the $SU(3)_C$ and $SU(2)_L$ gauge fields are governed by their group structures, with structure constants f_{abc} and ϵ_{ijk} defined in terms of the group operators, e.g.,

$$\left[T^a, T^b\right] = i f_{abc} T^c. \tag{1.6}$$

Because $U(1)$ is an Abelian group, the structure constant is zero, and there are no self interactions of the B_μ gauge field.

The Lagrangian describing the yet to be observed Higgs scalar field is given by

$$\mathcal{L}_\phi = (D^\mu \phi)^\dagger D_\mu \phi - V(\phi). \tag{1.7}$$

Here, the requirements of $SU(2) \times U(1)$ invariance and renormalizability limit the form of the Higgs potential $V(\phi)$ to

$$V(\phi) = +\mu^2 \phi^\dagger \phi + \lambda(\phi^\dagger \phi)^2. \tag{1.8}$$

The parameters must satisfy $\mu^2 < 0$ for spontaneous symmetry breaking to occur, and $\lambda > 0$ for vacuum stability.

Finally, the Yukawa term describes the interaction of the Higgs field with the matter fields. Because of the different weak hypercharge assignments for the up and down-type quarks, gauge invariance necessitates representations of the Higgs field with both $y = 1/2$ and $y = -1/2$. The representation $\phi^\dagger$ satisfies $y = -1/2$, but transforms as a conjugate $\mathbf{2}^*$ under $SU(2)_L$. However, the fundamental and conjugate representations of $SU(2)$ are equivalent, allowing us to use a single Higgs doublet[1] by using the representation $\tilde{\phi} = i\tau_2 \phi^\dagger$, which transforms as a $\mathbf{2}$ with $y = -1/2$. This allows us to write the Yukawa term as

$$\mathcal{L}_{\text{Yuk.}} = -Y_u^{ij} \bar{Q}_i \tilde{\phi} u_j - Y_d^{ij} \bar{Q}_i \phi d_j - Y_l^{ij} \bar{L}_i \phi e_j + h.c., \tag{1.9}$$

where the Y^{ij} are the Yukawa matrices. These are the the terms which give rise to fermion masses, as described in Section 1.1.2.

Finally, if we keep with the idea of including in our Lagrangian every renormalizable term which is locally invariant under SM symmetries, there is additional term, the CP violating

$$\mathcal{L}_\theta = -\frac{g_s^2 \theta}{32\pi^2} G^a_{\mu\nu} \tilde{G}^{\mu\nu a}. \tag{1.10}$$

However, experimental effects of such a term have not been observed, and limits on the neutron electric dipole moment [1] imply that $\theta < 10^{-10}$. While the smallness of this parameter has prompted a considerable amount of theoretical speculation, a detailed discussion is beyond the scope of this thesis.

1.1.2 Electroweak Symmetry Breaking

Gauge invariance prevents us from including mass terms in the Lagrangian for the gauge bosons or chiral fermions. If the gauge invariance is broken spontaneously in the vacuum state, effective masses may be induced for the particles propagating through it while maintaining the renormalizability of the theory. When $\mu^2 < 0$, such symmetry breaking occurs as the Higgs field acquires a vev. The Higgs potential (Eq. 1.8) contains and $O(4)$ symmetry which gives us the freedom to choose the direction of the vev; the canonical choice is

$$\langle \phi \rangle = \frac{1}{\sqrt{2}} \begin{pmatrix} 0 \\ \sqrt{-\mu^2/\lambda} \end{pmatrix} = \frac{1}{\sqrt{2}} \begin{pmatrix} 0 \\ v \end{pmatrix}, \tag{1.11}$$

[1] This is a consequence of the specific structure of $SU(2)$, and many extensions of the SM require multiple Higgs fields.

which corresponds to a minimum of the potential. This vev breaks the T^1, T^2, and $T^3 - Y$ symmetries but leaves $Q = T^3 + Y$ unbroken. Thus our $SU(2)_L \times U(1)_Y$ symmetry is broken to $U(1)_{EM}$.

We next quantize our Higgs field around the classical vacuum, which in unitary gauge gives

$$\phi = \frac{1}{\sqrt{2}} \begin{pmatrix} 0 \\ v + H \end{pmatrix}. \tag{1.12}$$

In this gauge, the Higgs kinetic term becomes

$$\begin{aligned} (D_\mu \phi)^\dagger D^\mu \phi &= \frac{1}{2}(0 \;\; v) \left(\frac{g}{2} \sigma_i W_\mu^i + \frac{g'}{2} B_\mu \right)^2 \begin{pmatrix} 0 \\ v \end{pmatrix} + H \text{ terms} \\ &= M_W^2 W^{+\mu} W_\mu^- + \frac{M_Z^2}{2} Z^\mu Z_\mu + H \text{ terms} \end{aligned} \tag{1.13}$$

Here we introduce the states corresponding to the broken generators

$$\begin{aligned} W^\pm &= \frac{1}{\sqrt{2}}(W^1 \mp i W^2) \\ Z &= -\sin\theta_W B + \cos\theta_W W^3, \end{aligned} \tag{1.14}$$

where the weak mixing angle relates the gauge couplings: $\tan\theta_W = g'/g$. The degrees of freedom corresponding to Nambu-Goldstone bosons for a broken global symmetry are eaten by these gauge bosons, giving rise to the mass terms in Eq. 1.13, with

$$\begin{aligned} M_W &= \frac{gv}{2}, \\ M_Z &= \sqrt{g^2 + g'^2}\frac{v}{2} = \frac{M_W}{\cos\theta_W}. \end{aligned} \tag{1.15}$$

Because the $U(1)_{EM}$ symmetry remains intact, the corresponding linear combination, $A_\mu = \cos\theta_W B + \sin\theta_W W^3$, the photon, is massless and does not appear in Eq. 1.13. The H terms suppressed in Eq. 1.13 contain the Higgs kinetic energy and the interactions of the $W^\pm$ and Z bosons with the Higgs field. We note that the weak boson masses depend only on the vev $v = (-\mu^2/\lambda)^{1/2}$; independent determination of the parameters μ^2 and λ requires consideration of the Higgs field itself.

When the Higgs acquires a vev, the Yukawa term for up-type quarks in Eq. 1.9 becomes, in the unitary gauge,

$$Y_u^{ij} \bar{Q}_i \tilde{\phi} u_j \to Y_u^{ij} \bar{u}_{Li} \left(\frac{v + H}{\sqrt{2}} \right) u_{Rj}. \tag{1.16}$$

The down-type quarks and lepton terms transform in an equivalent fashion. We see that this gives both the mass matrix, $M^u = Y^u v/\sqrt{2}$, as well as the Yukawa matrix, $h^u = M^u/v$, which determines the strength of the interaction of the fermions with the Higgs field. Because the Yukawa matrix is proportional to the mass matrix, heavy quarks have stronger couplings, and consequently take on a more important role in Higgs searches.

In general, the mass matrix is not diagonal, hermitian, or symmetric. If we wish to understand the theory in terms of the mass eigenstates, we may diagonalize the mass matrix with two unitary matrices,

$$A_L^{u\dagger} M^u A_R^u = M_D^u = \begin{pmatrix} m_u & & \\ & m_c & \\ & & m_t \end{pmatrix}. \tag{1.17}$$

We perform an equivalent diagonalization for the down-type quarks and leptons,

$$\begin{aligned} A_L^{d\dagger} M^d A_R^d &= M_D^d, \\ A_L^{e\dagger} M^e A_R^e &= M_D^e. \end{aligned} \tag{1.18}$$

These unitary transformations cancel out of neutral current interactions; however, the mismatch between weak and mass eigenstates becomes relevant for the weak charged current. From Eqs. 1.2 and 1.3, after symmetry breaking the $W^\pm$ bosons interact with the fermions according to

$$\mathcal{L}_{\rm cc} = -\frac{g}{2\sqrt{2}} \left(J_W^\mu W_\mu^- + J_W^{\mu\dagger} W_\mu^+ \right), \tag{1.19}$$

where the weak charge raising current is

$$J_W^{\mu\dagger} = \bar{\nu}_L^i \gamma^\mu e_L^i + \bar{u}_L^i \gamma^\mu d_L^i. \tag{1.20}$$

We focus on the second (quark) term. In order to see this in terms of the mass eigenstates, we perform the unitary transformations

$$u_L^i \to A_L^{uij} u_L^j, \qquad d_L^i \to A_L^{dij} d_L^j. \tag{1.21}$$

This term then becomes

$$\bar{u}_L^i \gamma^\mu d_L^i \to \bar{u}_L^i \gamma^\mu V_{\rm CKM}^{ij} d_L^j, \tag{1.22}$$

where we have introduced the *Cabibbo-Kobayashi-Maskawa* (CKM) mixing matrix,

$$V_{\rm CKM} \equiv A_L^{u\dagger} A_L^d = \begin{pmatrix} V_{ud} & V_{us} & V_{ub} \\ V_{cd} & V_{cs} & V_{cb} \\ V_{td} & V_{ts} & V_{td} \end{pmatrix}. \tag{1.23}$$

Consequently, the weak charged current allows for flavor-changing processes in the SM.

A unitary 3×3 matrix has nine real degrees of freedom, but in the CKM matrix, five of these are unobservable relative phases of the six quark fields. This leaves four parameters: 3 mixing angles and one CP violating phase. Experimentally, the CKM matrix is found to have a highly hierarchical structure, with mixing among the first two generations the strongest. This is made evident by the Wolfenstein parameterization [2],

$$V_{\rm CKM} = \begin{pmatrix} 1 - \lambda^2/2 & \lambda & A\lambda^3(\rho - i\eta) \\ -\lambda & 1 - \lambda^2/2 & A\lambda^2 \\ A\lambda^3(1 - \rho - i\eta) & -A\lambda^2 & 1 \end{pmatrix} + \mathcal{O}(\lambda^4), \tag{1.24}$$

where all parameters are $\mathcal{O}(1)$ and $\lambda \sim 0.22$.

We have thus far not discussed the small neutrino masses, for which there is clear evidence, so in this description there is no equivalent mixing matrix. However, for describing processes for which neutrino masses are relevant, particularly neutrino oscillations, the analogous PontecorvoMakiNakagawaSakata (PMNS) matrix is required. In processes for which neutrino mass is negligible, the neutrinos are defined entirely by their weak interactions, so there are no physically observable effects.

Finally, we turn to the Higgs potential, which after symmetry breaking, becomes in the unitary gauge

$$V(\phi) = -\frac{\mu^2}{4\lambda} - \mu^2 H^2 + \lambda\nu H^3 + \frac{\lambda}{4} H^4. \tag{1.25}$$

The first term is a constant which reflects the definition of the potential and is of no consequence to physics in the absence of gravity. The final two terms represent the Higgs self-couplings. The second gives a tree-level Higgs mass of $m_H = \sqrt{-2\mu^2} = \sqrt{2\lambda}v$, and represents the final unmeasured parameter of the SM. Direct searches at the CERN LEP and Tevatron colliders exclude the mass ranges $m_H < 114.4\,\mathrm{GeV}$ [3] and $158 < m_H < 173\,\mathrm{GeV}$ [4], respectively, for the SM Higgs.

We have begun with a set of symmetries, written all possible renormalizable terms respecting those symmetries, and assigned charges for the experimentally observed matter content. After spontaneous symmetry breaking in the Higgs sector, we are left with a rich theory with 19 physical parameters: 9 fermion masses, 3 gauge couplings, 4 CKM parameters, 2 parameters of the Higgs sector, and a tightly constrained strong CP violating phase. This theory has been remarkably consistent with experiment, but is not sufficient for describing all phenomena observed in nature. We discuss few of the possible issues and potential solutions in the following sections.

1.2 Shortcomings of the Standard Model

While the SM has proven effective at describing most of the phenomena we observe, there is growing evidence that it alone is not sufficient for describing the universe in which we live. A number of observations such as the following suggest that new ingredients must be added to the model.

- The observation of neutrino oscillations indicates that neutrinos have nonzero masses, which are absent in the SM.
- Several observations indicate the existence of non-baryonic dark matter in abundances that cannot be explained by SM particles alone.
- Supernova observations indicate that the expansion of the universe is accelerating. Together with fits of the cosmic microwave background power spectrum, the data indicate that the majority of the energy in our current universe is attributed to a "dark energy," with negative pressure.

- Our universe is dominated by matter, not antimatter, and the SM does not provide a mechanism for generating such a baryon asymmetry.

Additionally, the SM contains many unsettling theoretical issues, as follows.

- The great disparity between the gravitational ($\sim 10^{19}\,\mathrm{GeV}$) and weak ($\sim 10^{3}\,\mathrm{GeV}$) scales is unexplained, and leads to large divergent corrections to the Higgs mass, which must be remedied with an extremely finely-tuned cancellation. This is referred to as the hierarchy problem.
- The CP violating term (Eq. 1.10) allowed by gauge invariance and renormalizability appears to be extremely small, and the SM provides no explanation for why.
- The SM provides no explanation for why the matter content must be repeated with three generations.

This list is by no means exhaustive, and in this section we focus on two issues – dark matter and the hierarchy problem, both of which point to the possibility of new physics at the TeV scale. In Sec. 1.3 we discuss a few examples of such new physics.

1.2.1 The Hierarchy Problem

While the Higgs mechanism provides an elegant way of providing masses to SM particles, the Higgs boson has yet to be observed experimentally. Regardless, there is good reason to expect to find a Higgs or other physics around the weak scale. In the absence of Higgs boson exchange, calculation of the scattering probability for the longitudinal modes of W bosons, $W_L^+W_L^- \to W_L^+W_L^-$, blows up at high energies and exceeds unity above the TeV scale. If the electroweak theory is to remain perturbative above this scale, exchange of another particle below this scale is necessary to counteract the divergent behavior. Indeed, in the SM, the Higgs boson serves this role, as long as it is sufficiently light. Including SM Higgs boson exchange, the high-energy behavior of the $J = 0$ partial wave amplitude for longitudinal W scattering is given by [5]

$$\left|a_0(W_L^+W_L^- \to W_L^+W_L^-)\right| \to \frac{m_H^2}{8\pi v^2}. \tag{1.26}$$

Partial wave unitarity then places an upper limit on the Higgs mass set by the electroweak scale,

$$m_H \leq \sqrt{8\pi}v \simeq 1\ \mathrm{TeV}. \tag{1.27}$$

Consideration of other gauge boson scattering processes provides a slightly stricter, but still $\mathcal{O}$(TeV), constraint [5][6].

Additionally, if we take the view that the SM must only be valid up to some scale, Λ, above which there is a new physical description, we must ensure that the quartic coupling λ remains finite up to that scale. Calculation of the running of λ shows that the SM breaks

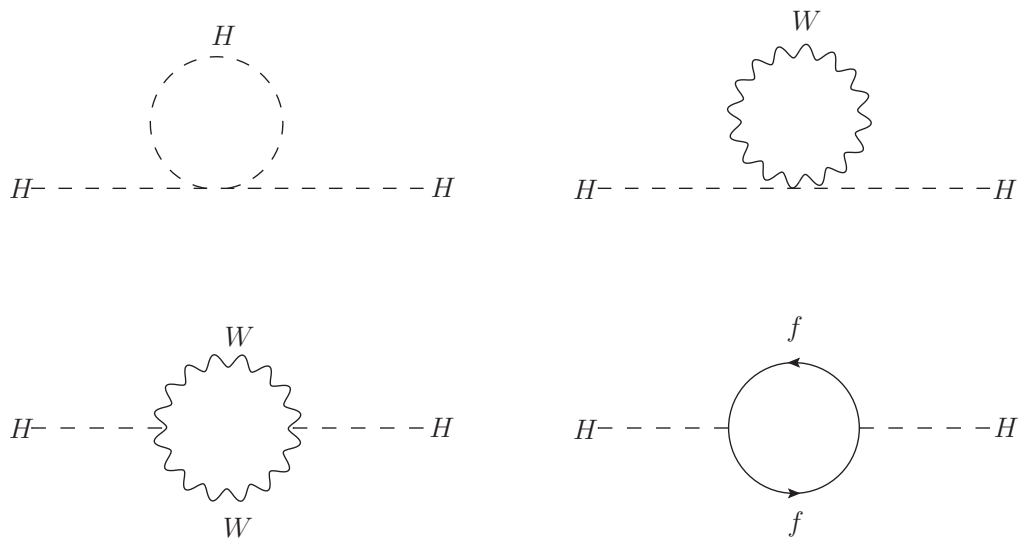

Figure 1.1: Radiative corrections to the Higgs mass.

down before the next known mass scale, the Planck scale, for $m_H \lesssim 180$ GeV [7]. If we assume that some new physics lies between the weak and Planck scales and take the conservative case of $\Lambda \approx 2m_H$, the constraint on the Higgs mass is still below the TeV scale, $m_H \lesssim 700$ GeV [8]. Furthermore, a SM Higgs mass in this range is suggested by experiment – a global fit to precision electroweak data favors a Higgs mass below the TeV scale [9].

In addition to the implications for the feasibility of experimental searches, a sub-TeV Higgs mass poses theoretical concerns. Fermion masses and dimensionless couplings are sensitive only to corrections logarithmic in the scale of new physics. Scalar masses, however, are quadratically sensitive to the scale Λ. The 1-loop radiative corrections to the SM Higgs mass are shown in Fig. 1.1, and produce such a quadratic divergence,

$$m_H^2 = (m_H^2)_{\text{bare}} + \mathcal{O}(\lambda, g^2, h^2)\Lambda^2. \tag{1.28}$$

If Λ is much larger than the weak scale, as is the case with the Planck and GUT scales, then by Eq. 1.28 the natural scale for the Higgs mass is Λ. This is of course contrary to the expectation of a weak scale Higgs mass. There then must be a very precise cancellation between the bare mass and the radiative corrections, a cancellation to about 30 digits in the case of $\Lambda \sim M_P$. Such fine-tuning is theoretically undesirable and reveals our ignorance as to why the weak and Planck scales are so many orders of magnitude apart. This is known as the hierarchy problem.

There are a few different approaches to the hierarchy problem. One is to replace the elementary Higgs field with a dynamical symmetry breaking mechanism based on new

strong dynamics, as in the case of technicolor. Other models introduce new symmetries to the theory which eliminate the divergent behavior, as in the case of the little Higgs. TeV scale supersymmetric theories contain canceling quadratic divergences between fermions and bosons. Another approach is to reduce the Planck scale by introducing additional dimensions. We discuss the last two of these approaches in Sec. 1.3.1 and Sec. 1.3.2, respectively. Finally, one might also take the view that the hierarchy problem is indeed not a problem at all, and the seemingly fine-tuned cancellation is simply present because it is required for our universe to exist as it does. While such "anthropic" arguments have proven compelling in other contexts (e.g., [10]), we shall not discuss them further here.

1.2.2 Dark Matter

While the SM effectively describes most of the matter we see, there is increasing evidence that ordinary matter accounts for only a small fraction of the total energy budget of the universe. In particular, a number of observations suggest the existence of an abundance of matter which is non-luminous, and therefore dubbed "dark." As we will see, the SM particle content is unable to account for this matter, suggesting the existence of a new type of particle. Here we review some of the evidence for dark matter and possible dark matter candidates.[2]

Some of the most direct evidence for the existence of cold dark matter (CDM, meaning it is not relativistic) comes at the galactic scale, where observation of the rotation of spiral galaxies is inconsistent with the expectation from visible matter. In the outskirts of a galaxy, there are very few stars, but there is cold neutral hydrogen gas, which emits $\lambda = 21\ \mathrm{cm}$ photons as a result of the hyperfine splitting of Hydrogen's energy levels. By examining spiral galaxies which are viewed edge on, the speed of the rotating gas can be measured from the redshift of the 21 cm line. The expected rotation speed is given by Newtonian dynamics as

$$v = \sqrt{G_N \frac{M(r)}{r}}, \tag{1.29}$$

where $M(r)$ is the total mass contained within a radius r. In the outer regions where only gas is expected to be present, $M(r)$ is expected to be approximately constant, which would lead to a rotation curve $v(r) \propto r^{-1/2}$. The observed behavior, however, is flat at large radius. This suggests that the profile of the mass density of the galaxy is $\rho(r) \propto r^{-2}$ in this region. Such behavior is consistent with a spherical halo of dark matter containing the disk of the galaxy. While the exact dark matter profile, especially near galactic centers, remains uncertain, the behavior of rotation curves provides compelling evidence for the presence of dark matter in galaxies.

The scale of galactic clusters is where evidence for dark matter first appeared. In 1933, Zwicky determined the velocities of galaxies in the Coma cluster by measuring the Doppler

[2]For a more complete review of dark matter, see [11][12][13], on which much of this section is based.

shifts of spectral lines. Assuming the motion of the galaxies was virialized [14],

$$mv^2 = 2\langle E_{\text{kin.}}\rangle = -\langle E_{\text{grav.}}\rangle = G_N m\langle M/r\rangle, \tag{1.30}$$

he was able to determine the mass of the cluster, which he found far exceeded the luminous matter. This large discrepancy suggested the presence of a significant amount of dark matter. As observational techniques have advanced, more sophisticated methods of measuring cluster masses have been developed. X-ray telescopes, for example, make it possible to see the hot gas that accounts for much of the baryonic matter in clusters, and gravitational lensing of light from distant galaxies by a cluster allow its total mass to be estimated; these techniques corroborate the dark matter claims of virial mass observations.

Some of the most important recent observations for understanding the matter content of the universe come from cosmology. The standard model of cosmology contains three ingredients: the relationship between the geometry and energy/matter content, given by the Einstein equations; symmetries, as reflected by the metric; and the properties of the matter/energy content, given by their equations of state. The universe is observed to be largely homogeneous and isotropic; this implies a specific form for the metric, which when combined with some components of the Einstein equations, gives the Friedmann equation,

$$H^2 + \frac{k}{a^2} = \frac{8\pi G_N}{3}\rho_{tot}. \tag{1.31}$$

Here a is the scale factor of the universe, ρ_{tot} is the total energy density, and $k = -1, 0, \text{ or } 1$ describes the spatial curvature. The Hubble parameter, $H = \dot{a}/a$, is often expressed as $H = 100\, h\ \text{km s}^{-1}\ \text{Mpc}^{-1}$, where $h \approx 0.7$ is a dimensionless parameter. There is a critical density,

$$\rho_c = \frac{3H^2}{8\pi G_N}, \tag{1.32}$$

for which the universe is flat $(k = 0)$. For a specific species of energy or matter, we define $\Omega_i \equiv \rho_i/\rho_c$. Because the different components of matter and energy have different equations of state, their evolutions over time vary, leading to a general expression for the expansion of the universe as a function of redshift (z):

$$\frac{H^2(z)}{H_0^2} = -\frac{k}{a_0^2 H_0^2}(1+z)^2 + \Omega_\Lambda + \Omega_M(1+z)^3 + \Omega_R(1+z)^4, \tag{1.33}$$

where M refers to matter, R is radiation, and Λ is the vacuum energy, here taken to be a cosmological constant.

These parameters can be fit to the power spectrum of the cosmic microwave background (CMB) recorded by the Wilkinson Microwave Anisotropy Probe (WMAP) collaboration. Because the acoustic peaks of the CMB arise from gravity driven oscillations of photons which were coupled with baryons, their form is separately sensitive to both the total matter component (which determines the gravitational potential) and baryonic component. The

WMAP 7-year data alone, with a six-parameter ΛCDM fit, finds a large discrepancy between the total matter $\Omega_M h^2 = 0.1345^{+0.0056}_{-0.0055}$ and baryonic matter $\Omega_b h^2 = 0.02249^{+0.00056}_{-0.00057}$ [15]. This not only indicates the presence of a non-baryonic dark matter component, but also gives a measure of its size. These values are consistent with those required for correct elemental abundances in Big Bang neucleosynthesis [16] and for the imprint of baryon acoustic oscillations on the galaxy-galaxy correlation function [17].

While the evidence for non-baryonic dark matter is well established, the true nature of dark matter is still unknown. What is known is that it must be stable on cosmological time scales, it must be produced with the correct relic abundance, and it must interact only very weakly with electromagnetic radiation.

A natural candidate for a dark matter particle within the SM would be the neutrino, due to its weak coupling to other SM particles. However, the relic abundance of SM neutrinos is known to be

$$\Omega_\nu h^2 = \sum_{i=1}^{3} \frac{m_i}{93 \text{ eV}}, \tag{1.34}$$

where m_i are the masses of the three generations of neutrinos. But tritium beta decay experiments put an upper limit on the neutrino masses[3] of about 2 eV [18], giving $\Omega_\nu \lesssim 0.07$, which is not sufficient to account for the total dark matter abundance. Furthermore, neutrinos are bound by the Tremaine-Gunn limit [19][20]. The idea is that if neutrinos are too light, packing them densely enough to provide enough mass for certain galactic dark matter halos would violate the Pauli exclusion principle; to avoid this violation, the mass must be raised to $\gtrsim 500$ eV, giving $\Omega_\nu > 1$, which would over-close the universe. Neutrino dark matter runs into further problems with structure formation [21] and fits to the CMB power spectrum [15].

Another possible dark matter candidate is a massive astronomical object, such as a star or planet which is too dark to be seen, or an exotic object such as a primordial black hole. Such candidates are referred to as MAssive Compact Halo Objects (MACHOs), and have been searched for by their gravitational microlensing effects. These searches have determined that for a large range of masses, there are not enough such objects to account for the mass in the galactic halo [22].

Perhaps the most currently viable dark matter candidates are weakly interacting massive particles, or WIMPs. Such particles are stable and heavy enough to have escaped our detection, but light enough to have been generated in the early universe. The current expected abundance of a WIMP candidate is determined by its mass and interactions. In the early hot universe, WIMPs would have been created until the temperature dropped below their mass. At that point they would begin to annihilate with one another, producing lighter particles. However, as the universe expanded, annihilations would become less common and eventually cease at the "freeze-out temperature," when the expansion rate becomes comparable to

[3] Although the determination of this bound is specific to electron neutrinos, the relatively smaller mass splittings observed in neutrino oscillation experiments indicate that other species are also bounded by this limit.

the annihilation rate. This sets the abundance, as we are requiring our WIMPs to be stable on cosmological time scales; the current density is then determined by the expansion of the universe since freeze-out. Calculation of this process gives an estimate for the annihilation cross section of a WIMP candidate χ, assuming its present-day abundance to account for the dark matter we see, of

$$\langle \sigma_{\text{ann.}} v \rangle \approx 10^{-9}\ \text{GeV}, \tag{1.35}$$

where the brackets denote a thermal average. Comparing this to a typical annihilation cross section for an interaction of electromagnetic strength,

$$\sigma_{\text{ann.}} v \approx \frac{\pi \alpha^2}{m_\chi^2}, \tag{1.36}$$

we get an estimate for our WIMP mass,

$$m_\chi \approx 300\ \text{GeV}. \tag{1.37}$$

This is an interesting result, as it coincides with the scale of the hierarchy problem, and it lies beyond the reach of past collider experiments, but within reach of the LHC. We will discuss two examples of theories with WIMP candidates in Section 1.3.

1.3 Beyond the Standard Model

As discussed in Section 1.2, a number of questions are left unanswered by the standard model, and both the hierarchy problem and WIMP dark matter scenario suggest that new physics may appear at the TeV scale. In this section we discuss two of the most widely studied ideas for answering these questions, supersymmetry and extra dimensions. Both have TeV-scale realizations which provide a dark matter candidate, along with a large spectrum of new particles that may be seen in future collider experiments. Some of the challenges of using colliders to measure and distinguish such models will be addressed in Chapters 2−5.

1.3.1 Supersymmetry

One approach to solving the hierarchy problem is to take a note from history[4] – in particular, if we consider the case of classical electromagnetism, we find that the electron mass receives a correction from its self-energy which is quadratically divergent. In order to explain the electron mass we observe, a negative bare mass term would be required to precisely cancel the self-energy contribution; otherwise, the theory would break down at a scale $\mathcal{O}(10^{-13}\ \text{cm})$. This problem is solved by doubling the degrees of freedom with the introduction of another particle, the positron, whose contribution to the electron mass is

[4] We note, however, that this argument did not provide the original motivation for studying supersymmetry. See [13] for a more detailed calculation, and [23] for a more thorough review of supersymmetry.

also quadratically divergent, but with a negative sign. This leaves only a logarithmically divergent term, which dramatically reduces the need for tuning.

This type of quadratic divergence is just what we have in the hierarchy problem, and the idea of supersymmetry (SUSY) as a solution is very much the same – we cancel the divergence by doubling the degrees of freedom. If we consider, for example, a fermion loop contribution generated by an interaction $-\lambda_f f \bar{f} H$ in Fig. 1.2, we get the correction

$$\Delta(m_H^2)_f = -\frac{|\lambda_f|^2}{8\pi^2}\Lambda^2 + \dots. \tag{1.38}$$

If our theory also contained a scalar S which interacted with the Higgs as $-\lambda_S |H|^2 |S|^2$ as in Fig. 1.2, we would get an additional correction of

$$\Delta(m_H^2)_S = +\frac{\lambda_S}{16\pi^2}\Lambda^2 + \dots \tag{1.39}$$

The key here is the sign difference between Eqs. 1.38 and 1.39; because fermions and bosons contribute corrections with opposite signs, if there is a symmetry which properly relates them, and therefore their couplings, their contributions will cancel, thereby eliminating the divergent behavior. This is exactly what supersymmetry provides.

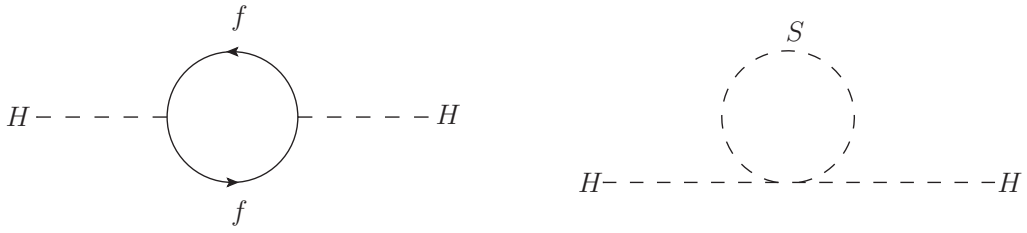

Figure 1.2: Radiative corrections to the Higgs mass from a fermion (left) and scalar (right).

A supersymmetric theory then contains supermultiplets with both bosonic and fermionic components. The supersymmetric theory with minimal additional matter content, the so-called minimal supersymmetric standard model (MSSM), assigns a partner to each of the SM fields. The chiral supermultiplets contain SM fermions and new scalar counterparts, which are named by adding an "s" to the SM name, e.g. squarks and sleptons. The gauge supermultiplets contain the SM gauge bosons and new fermionic partners, denoted by the suffix "-ino," e.g. Wino and Bino. All new partners are denoted with a tilde, so a sneutrino is written $\tilde{\nu}$. In addition to the usual SM fields, in the MSSM the Higgs sector must be expanded to two Higgs doublets, which separately give rise to up-type quarks (H_u) and down-type quarks (H_d), which allows the theory to be anomaly-free.[5] Because of the effects of electroweak symmetry breaking, the superpartners of SM gauge bosons will in

[5]Apart from the anomaly condition, two Higgs doublets are necessary due to the requirement that the superpotential be a holomorphic function of the superfields.

general mix with one another. We denote the mass eigenstates of charged gauginos as charginos ($\tilde{\chi}_1^{\pm}$,$\tilde{\chi}_2^{\pm}$), and the mass eigenstates of neutral gauginos as neutralinos ($\tilde{\chi}_1^0$, $\tilde{\chi}_2^0$, $\tilde{\chi}_3^0$, $\tilde{\chi}_4^0$).

If all interactions obeyed supersymmetry, then the generation of masses to SM particles would impart equal masses to their superpartners. Clearly this is not the case, as they would have been produced and detected at collider experiments. Therefore, SUSY must be broken at some higher scale, which sets the fermion masses. Here we do not discuss the different SUSY breaking scenarios, but note the implications of mass differences between SM particles and their superpartners. In particular, returning to the hierarchy problem, the main fermion contribution to quadratic divergence of the Higgs mass will come from the top quark, due to its large Yukawa coupling. If its mass were the same as that of its partner, the stop, the two diagrams in Fig. 1.2 would cancel each other completely. Because we expect their masses to be different, while the quadratic divergence cancels, a logarithmic divergence remains,

$$(\Delta m_H^2)_{\text{top}} + (\Delta m_H^2)_{\text{stop}} = -\frac{3h_t^2}{4\pi^2}(m_{\tilde{t}}^2 - m_t^2)\log \Lambda/m_{\tilde{t}} + \dots \tag{1.40}$$

While this divergence is much milder than what we started with, a stop mass of $\sim 1\ \text{TeV}$ already requires a tuning of the cancellation with the bare mass at the 1% level. This suggests that if SUSY is responsible for solving the hierarchy problem, the SUSY-breaking scale, and therefore the superpartner masses, should not lie too far above the TeV scale.

One of the main concepts behind constructing the SM Lagrangian is that once the symmetries are specified, the Lagrangian must contain all renormalizable terms which respect those symmetries. If we take this approach with the MSSM, however, we are left with several possible terms which violate either lepton number or baryon number, both of which are conserved by accidental symmetries in the SM. One consequence is that processes violating both lepton and baryon number, such as proton decay, could occur. Fig. 1.3 shows an example of such a process, $p \to e^+\pi^0$. If the relevant couplings were $\mathcal{O}(1)$ and the SUSY partners had $\mathcal{O}(\text{ TeV})$ masses, this would give a decay rate for this process of around $\tau \sim m_{\tilde{s}}^4/m_p^5 \approx 10^{-12}$ s, which is in clear violation of the current bound of over 10^{33} years [24].

These types of interactions can be avoided by introducing a new $\mathbb{Z}_2$ symmetry known as "R parity," defined as

$$P_R = (-1)^{3B+L+2s}, \tag{1.41}$$

which must be conserved by all interactions. Under this, all SM particles have $P_R = +1$, and all superpartners have $P_R = -1$. This means that there can be no mixing between SM particles and superpartners, and there can be no interaction vertices with an odd number of superpartners. An important consequence of this is that if R-parity is exactly conserved, the lightest particle with $P_R = -1$, known as the lightest supersymmetric particle (LSP), will be stable. This is especially interesting because if the LSP is a neutral particle, such as a sneutrino or neutralino, then it could be a dark matter candidate. R-parity conservation

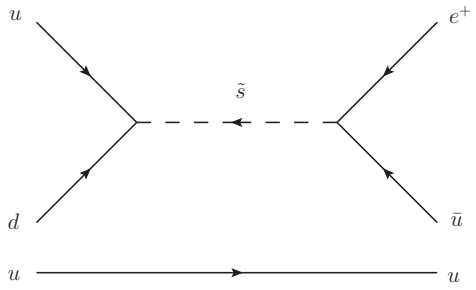

Figure 1.3: A possible interaction leading to proton decay via a supersymmetric particle.

also has implications for collider physics: superpartners may only be produced in pairs, and any superpartner produced will have a decay chain which includes an odd number of LSPs, which would not be seen by a detector.

One additional attractive feature of SUSY is its role in unification. One appealing idea in particle physics is that at some high scale, the gauge couplings of the three SM symmetries all converge on a single value, at which point the three interactions are all merged into one under a single larger symmetry. In the SM, the running of the coupling constants does not result in a single intersection. However, the addition of superpartners modifies the runnings and causes the couplings to converge at a single point at a scale of $\Lambda_{\rm GUT} \approx 10^{16}$ GeV. As a consequence, many models of unification assume supersymmetry.

1.3.2 Extra Dimensions

In the previous section we discussed how the large $\mathcal{O}(\Lambda^2)$ correction to the Higgs mass could be remedied by introducing a symmetry which caused the cancellation of this term. An alternate approach is to reduce the scale at which this term is evaluated. Normally, we take the next scale of physics to be the Planck scale, $M_{\rm Pl} = G_N^{-1/2} \approx 10^{19}\,{\rm GeV}$, at which the size of the gravitational force becomes comparable to the other forces, and the effects of quantum gravity can no longer be safely ignored. Here, however, we consider a scenario in which gravity becomes relevant at much lower energies.[6]

One idea for explaining the apparent relative weakness of the gravitational force is the introduction of additional, compact, large extra dimensions [28]. The basic idea is that we introduce n additional dimensions of radius R, so that at distances $r \ll R$, two masses m_1 and m_2 would have a gravitational potential energy given by Gauss's law in $3+n$ spatial dimensions,

$$V(r) = \frac{m_1 m_2}{M_D^{n+2}} \frac{1}{r^{n+1}} \qquad (r \ll R), \tag{1.42}$$

where M_D is the Planck mass in $D = n+3$ spatial dimensions. The changed dependence

[6] Much of this section was based on the reviews of [25][26][27].

on r is a consequence of the field lines spreading out in these additional dimensions. At large distances, $r \gg R$, however, the spread of the field lines in the extra dimensions is confined by the size, so the usual $1/r$ behavior is restored,

$$V(r) = \frac{m_1 m_2}{M_{\rm Pl}^2} \frac{1}{r} \qquad (r \gg R). \tag{1.43}$$

Continuity at $r = R$ then gives us the true D-dimensional scale,

$$M_D^{n+2} R^n = M_{\rm Pl}^2. \tag{1.44}$$

If we wish to reduce the scale of gravity to be comparable to the electroweak scale, $M_D \approx 1\,\mathrm{TeV}$, then we find that our extra dimensions must have $R \approx 10^{15},\ 10^{-1},\ 10^{-6}\,\mathrm{cm}, \ldots$ for $n = 1, 2, 3, \ldots$. The $n = 1$ case would cause deviations on the scale of the solar system, and is clearly ruled out. The $n = 2$ case is ruled out by a sensitive test of the inverse square force law, which finds that such extra dimensions are limited to $R \leq 44\mu\mathrm{m}$ [29]. Larger numbers of extra dimensions, however, are consistent with this bound.

Apart from the question of whether the extra dimensions are consistent with tests of gravity, we must also consider the effects of allowing particles to propagate in additional dimensions. We take x to be the usual $3 + 1$ dimensional coordinates and y to be the additional coordinates, which we take to lie on an n-dimensional torus of radius R. Then a bosonic field, for example, can be expanded into Fourier modes of the new coordinates, which is a discrete sum due to the finite size of the additional dimensions,

$$\phi(x, y) \sim \sum_{\vec{n}} \phi^{(\vec{n})}(x) \exp\left(i \frac{\vec{n} \cdot \vec{y}}{R}\right). \tag{1.45}$$

The component of the momentum in the extra dimensions of a mode is then $\vec{n}/R$, so we see each mode as a particle propagating in $3 + 1$ dimensions with a mass

$$m_{\vec{n}}^2 = m_0^2 + \frac{|\vec{n}|^2}{R}, \tag{1.46}$$

where m_0 is the mass of the zero mode. Thus we see a tower of particles, referred to as Kaluza Klein (KK) states.

However, if our SM particles are propagating in extra dimensions of this size, we should have seen KK states by now, as we have already probed up to scales of order $R \approx (1\,\mathrm{TeV})^{-1} \approx 10^{-17}\,\mathrm{cm}$. This issue can be averted by preventing SM particles from propagating in the extra dimensions, which is often done by restricting them to a $3 + 1$-dimensional brane, which may imply a connection with string theory. In such models, only gravity is allowed to propagate freely in the extra dimensions.

An alternate approach is to choose much smaller extra dimensions, $R^{-1} \approx 1\,\mathrm{TeV}$, in which the KK modes are heavy enough to avoid detection thus far,[7] allowing us to

[7] From Eq. 1.46, it would appear that with R^{-1} much larger than most SM masses, the KK spectrum is highly degenerate. Loop corrections modify the masses given by of Eq. 1.46, generating some small mass splittings.

freely choose which fields propagate in the additional dimensions. One notable way of having such small extra dimensions while still providing an explanation to the hierarchy problem is to introduce an exponential, not flat, metric on a single extra dimension [30]. In this scenario, the graviton wavefunction becomes warped, and the hierarchy problem may be solved if the Higgs field lives on or near the "IR" brane, where the gravitational scale is exponentially suppressed relative to the "UV" brane on the other end of the extra dimension.

Another popular option for small extra dimensions is to choose a flat metric and allow all SM fields to propagate freely throughout, a setup known as universal extra dimensions (UED) [31]. Because the dimensions are TeV scale and flat, UED alone does not a provide an explanation for the hierarchy problem, but it has many appealing phenomenological features. In particular, because all of the fields propagate in the extra dimension, they will have TeV scale KK modes. This is similar to the setup supersymmetry, where each SM particle has a heavy superpartner, with one notable exception – in UED, the heavy partners have the same spins as their SM counterparts. This similarity has given UED the nickname "bosonic supersymmetry," and demonstrates the importance of spin determination as a means of distinguishing models of new physics. We will discuss this situation in further detail in Chapter 3.

Allowing fermions to propagate in an additional dimension introduces a new difficulty in creating chiral fermions. In the case of one extra dimension, we have five-dimensional fermions, which are necessarily vector-like. The Clifford algebra of five dimensions is created by five anti-commuting matrices, Γ^α ($\alpha = 0, 1, 2, 3, 4$), which can be written in terms of the usual gamma matrices of four dimensions as $\Gamma^\mu = \gamma^\mu$ ($\mu = 0, 1, 2, 3$) and $\Gamma^4 = i\gamma^5$. Because $\Gamma^4 \propto \Gamma^0\Gamma^1\Gamma^2\Gamma^3$, it is impossible to create an operator analogous to γ^5 in four dimensions – that is, a matrix with unit norm that commutes with all Γ^α. This means that a bilinear term necessary for an axial current is not invariant under 5D Lorentz transformations, and we cannot create chiral fermions. This is clearly a problem, because the SM distinguishes left and right-handed fermions, so we must be able to generate chiral zero modes.

One approach to this issue is to introduce a process called orbifolding. If we suppose that our fifth dimension is compactified on a circle S^1, with $y \in [-\pi R, \pi R]$, then if we identify points y and $-y$, we are left with a half circle, $S^1/\mathbb{Z}_2$, with fixed points at $y = 0$ and $y = \pi R$. The 5D action of a fermion ψ,

$$S_\psi = \int d^4x \int_0^{\pi R} dy \, \frac{i}{2} \left(\bar{\psi}\Gamma^\alpha \partial_\alpha \psi - (\partial_\alpha \bar{\psi})\Gamma^\alpha \psi \right), \tag{1.47}$$

must be stationary under an arbitrary variation of the field, both between and at the fixed

points, giving

$$\begin{aligned}\delta S_\psi^v &= -\int d^4x \int_0^{\pi R} dy\; i(\partial_\alpha \bar{\psi})\Gamma^\alpha \delta\psi = 0, \\ \delta S_\psi^s &= \int d^4x \int_0^{\pi R} dy\; \frac{i}{2}(\bar{\psi}\Gamma^4\delta\psi|_{y=\pi R} - \bar{\psi}\Gamma^4\delta\psi|_{y=0}) = 0. \end{aligned} \tag{1.48}$$

If we define our 5D fermion in terms of 4D chiral fermions,

$$\psi(x^\mu, y) = \frac{1+i\Gamma^4}{2}\psi(x^\mu, y) + \frac{1-i\Gamma^4}{2}\psi(x^\mu, y) = \psi_L(x^\mu, y) + \psi_R(x^\mu, y), \tag{1.49}$$

then the first stationary condition of Eq. 1.48 can be decomposed into

$$\begin{aligned}\Gamma^\mu \partial_\mu \psi_L &= -\Gamma^4 \partial_4 \psi_R, \\ \Gamma^\mu \partial_\mu \psi_R &= -\Gamma^4 \partial_4 \psi_L. \end{aligned} \tag{1.50}$$

The second condition of Eq. 1.48, which is a consequence of the existence of fixed points, allows us to generate chiral zero modes with a judicious choice of boundary condition. In particular, if we wish to generate a left-handed SM fermion, we may choose the boundary conditions

$$\begin{aligned}\partial_4 \psi_L(x^\mu, 0) = \partial_4 \psi_L(x^\mu, \pi R) = 0, \\ \psi_R(x^\mu, 0) = \psi_R(x^\mu, \pi R) = 0. \end{aligned} \tag{1.51}$$

This allows us to write the KK decomposition of our fermion field as

$$\psi(x^\mu, y) = \frac{1}{\sqrt{\pi R}}\left\{\psi_L^{(0)}(x^\mu) + \sqrt{2}\sum_{n\geq 1}\left[\psi_L^{(n)}(x^\mu)\cos\left(\frac{ny}{R}\right) + \psi_R^{(n)}(x^\mu)\sin\left(\frac{ny}{R}\right)\right]\right\}. \tag{1.52}$$

We see that the condition of Eq. 1.51 forces our right-handed modes to be $\sim \sin(ny/R)$, which eliminates the right-handed component from the SM. Thus we have chiral SM fermions along with a tower of heavier KK states with both chiralities.

The process of orbifolding has consequences beyond allowing chiral 4D fermions. Because KK number is a measure of a particle's momentum in the extra dimension, one might expect conservation of momentum to lead to conservation of KK number. The translational symmetry of the dimension is broken by the orbifolding process, and so therefore is the conservation law. However, a $\mathbb{Z}_2$ symmetry remains under $y \to \pi R - y$, which leads to a new conserved quantity, called KK parity, which carries a value of $(-1)^n$ for the n^{th} KK mode. This has phenomenological implications quite similar to R-parity in supersymmetry – the lightest new particles $n = 1$ have KK parity opposite their SM counterparts, and so may only be produced in pairs at colliders. Furthermore, the lightest such KK partner (LKP) cannot decay into SM particles, making it a good, stable dark matter candidate.

As with the LSP, the LKP will appear at the end of any decay chain of a $n = 1$ partner, resulting in large missing energy signatures.

We now turn to a discussion in Chapter 2 of how to extract information from these events where multiple heavy particles go unseen, and we discuss how the phenomenologically similar theories of SUSY and UED could be distinguished in Chapter 3.

Chapter 2

Mass Measurement in Boosted Decay Systems at Hadron Colliders

One of the most important steps in understanding new physics accessible at a collider is to determine the masses of new particles. In this chapter, we report a new possibility of using the M_{CT2} (Constransverse mass) variable for mass measurement of single step decay chains involving missing particles with moderate transverse momentum. We show that its experimental feasibility is enhanced compared to the corresponding M_{T2}-kink method and apply this method to reconstruct the masses in a chargino decay into a sneutrino, which was not possible previously.

2.1 Introduction

As discussed in Section 1.3, many theories of new physics beyond the Standard Model (SM) are expected to provide a rich invisible energy signal from their Lightest New Particles (LNP), which are stable dark matter candidates, missing in the detector. In this situation only the so-called "M_{T2}-kink" method can provide the information necessary to determine the masses of both mother particle and missing LNP simultaneously for the events with a pair of single step decay chains [32, 33].

The origin of the M_{T2}-kink is the variety of "Extreme Kinematic Configurations (EKCs)" in the events which can contribute to the maximum of the M_{T2} distribution. In general, for a given trial LNP mass, χ, the different EKCs will take on different values, so in different regions of χ, $M_{T2}^{max}(\chi)$ will follow different functional forms. At the true value, $\chi = m_X$, all of the EKCs should provide the same M_{T2} maximum value as the true mother particle mass, m_Y, by the definition of M_{T2} [34]. Consequently, $M_{T2}^{max}(\chi)$ shows a slope discontinuity at the kink point, $M_{T2}^{max}(\chi = m_X) = m_Y$.

Let us consider the system of a pair of single step decay chains at the LHC: $p + p \to \delta_T + Y_1/Y_2(\to \alpha X_1/\beta X_2)$, where $Y_{1,2}$ are the two mother particles with identical masses, each decaying to visible $\alpha(\beta)$ and missing LNP ($X_{1(2)}$). Here δ_T denotes the other remnants

(and its transverse momentum) not from Y_i decays, i.e., from the Initial State Radiation (ISR) or decays before Y_i, so that they provide the total transverse momentum of the Y_{1+2} system of $-\delta_T$. In this event topology, there are two physical degrees of freedom that can generate the variety of EKCs developing the kink. One is the invariant mass of visible particles $m_{\alpha,\beta}$ in $N(\geq 3)$-body decays, generating a so-called "Mass Kink" [32], and the other one is non-zero transverse momentum (δ_T) leading to a "Boosted Kink (BK)" [33] of the Y_{1+2} system of our interest. When $\alpha(\beta)$ consists of a single visible particle and has a fixed invariant mass, then only the BK provides enough constraints for simultaneous mass measurement.

However, the BK is not easy to identify [33]. This is because it requires very large δ_T to have a clear kink structure, and with the highest practical values of $\delta_T/m_Y \sim O(1-10)$ at the LHC, the kink structure is not clear enough to be reliably measured. Additionally, since the real profiles of the δ_T distribution must be sharply decreasing for large values at the LHC, the endpoint structure of the $M_{T2}(\chi)$ distribution becomes worse with a long tail if we require large δ_T. This may introduce significant systematic errors in fitting the endpoint.

2.2 The M_{CT2} Boosted Kink

In this section we present the maximal endpoint behavior of the $M_{CT2}(\chi)$ distribution [35] for single step decay chains with non-zero δ_T. $M_{CT2}^{max}(\chi)$ is sensitive to changes in δ_T, which can enhance the experimental feasibility of measuring the masses of both mother and missing LNP simultaneously. In particular, for systems with near degenerate mass spectra, $m_X/m_Y \approx 1$, the shift of M_{CT2} endpoint can be magnified significantly compared to that of the M_{T2} endpoint. The amount of the shift can easily be beyond the region of experimental uncertainties; one can have a good opportunity to measure both of the masses by reconstructing the functional value of $M_{CT2}^{max}(\chi)$ for several values of δ_T. As an example, we demonstrate a way to measure the $\tilde{\chi}_1^{\pm}$ and $\tilde{\nu}$ masses in a SUSY model using the properties of M_{CT2}.

M_{CT2} (Constransverse mass) [35] for the Y_{1+2} system is defined as follows:

$$\begin{aligned} M_{CT2}(\chi) &= \min_{k_{1T}+k_{2T}=\not{E}_T} \left[\max\left\{M_{CT}^{(1)}, M_{CT}^{(2)}\right\}\right] \\ M_{CT}^{(1)}(\chi)^2 &= \chi^2 + 2(|\alpha_T|e_1 + \alpha_T \cdot k_{1T}), \end{aligned} \tag{2.1}$$

where $k_{1,2T}$ and $e_{1,2}$ are the transverse (Tr) momenta and Tr energy, respectively, of missing $X_{1,2}$, with total missing Tr momentum, $\not{E}_T = -(\alpha_T + \beta_T) - \delta_T$. The $\alpha_T(\beta_T)$ are the Tr momenta of visible particles from $Y_1(Y_2)$ decays, and $-\delta_T$ is the total Tr momentum of the Y_{1+2} system. For the Y_2 decays, $M_{CT}^{(2)}$ is defined with β_T and k_{2T}. Here χ denotes the trial test mass of X_i, and visible particle masses are assumed to be zero, but the definition of the M_{CT2} can be easily generalized for massive visible particle events. Basically, the M_{CT2} variable is a mixture of M_{T2} (Stransverse Mass) [34] and M_{CT} (Contransverse Mass) [36].

In [35] it was found that the endpoint structure of the M_{CT2} distribution can be amplified depending on the value of trial mass, χ, and M_{CT2} was employed to measure some physical constraints involving squark and gluino masses with fewer systematic errors in pinpointing the endpoint than with the M_{T2} analysis.

When $\delta_T = 0$, the $M_{CT2}(\chi)$ has a one-to-one correspondence with $M_{T2}(\chi)$, and its maximum value is given as follows [35] :

$$M_{CT2}^{max2}(\chi) = \chi^2 + 2(\alpha_0 E_X^0 - \alpha_0^2), \tag{2.2}$$

where $\alpha_0 = \frac{m_Y^2 - m_X^2}{2m_Y}$ and $E_X^0 = \sqrt{\chi^2 + \alpha_0^2}$. However, if $\delta_T \neq 0$, the maximum profile of the $M_{CT2}(\chi)$ distribution shows a 2nd-order Boosted Kink, ${}^2BK$, structure which is different from the BK of M_{T2}. As investigated in [32, 33], the $M_{T2}^{max}(\chi, \delta_T)$ value of the Y_{1+2} system is the same as the $M_T^{max}(\chi, \delta_T/2)$ of single Y_i decay system, and the EKC for the M_{T2}^{max} can be characterized by a pair of identical EKCs corresponding to the M_T^{max} of single Y_i decays although they have to be combined to produce the event with general $\sqrt{s} \geq 2m_Y$. Then, in the language of single Y_i decay, the BK of $M_{T2}^{max}(\chi)$ is provided by two EKCs of the single Y_i decay events, characterized as follows:

$$\textbf{a)}\ \phi^{max} = 0 \text{ for } \chi \leq m_X \quad \textbf{b)}\ \phi^{max} = \pi \text{ for } \chi \geq m_X$$

where ϕ^{max} is the azimuthal angle between visible Tr momentum and δ_T in the rest frame of the Y_i with vanishing $\Delta\eta(\equiv \eta_{vis} - \eta_{inv})$. Similarly, the EKCs for $M_{CT2}^{max}(\chi)$ with ${}^2BK$ can be also characterized by single Y_i decays, but the azimuthal angle dependence is different:

1) $\cos\phi^{max} = \frac{m_X^2 m_Y^2}{|\bar{\delta}_T| E_Y (m_Y^2 - m_X^2)} \left[\frac{\chi^2}{m_X^2} + \frac{|\bar{\delta}_T|^2}{m_Y^2}\right]$ for $\chi \leq \chi_*$

2) $\cos\phi^{max} = -1$ for $\chi \geq \chi_*$,

where $|\bar{\delta}_T| = |\delta_T|/2$ and $E_Y = \sqrt{m_Y^2 + |\bar{\delta}_T|^2}$. Fig. (2.1a) shows $M_{CT2}(\chi) - \chi$ vs. χ for $(m_Y, m_X) = (130, 100)\,\text{GeV}$ with $\delta_T = 20\,\text{GeV}$. In the plot, the $M_{CT2}^{max}(\chi)$ is described by the two curves in the two regions of χ divided by ${}^2BK$, $\chi_* = 21.8\,\text{GeV}$. For $\chi \leq \chi_*$, $M_{CT2}^{max}(\chi)$ follows the blue curve; it switches to the red one for $\chi \geq \chi_*$ with a continuous slope at $\chi = \chi_*$, where the χ_* is given by

$$\chi_*^2 = |\bar{\delta}_T| \left(2\alpha - |\bar{\delta}_T|\right), \tag{2.3}$$

with $\alpha = |\alpha_0|(\frac{|\bar{\delta}_T|}{m_Y} + \frac{E_Y}{m_Y})$. It is not hard to see that whenever χ_* is real, a ${}^2BK$ appears and the EKC $-$ **1**) contributes to the $M_{CT2}^{max}(\chi < \chi_*)$. Then the M_{CT2}^{max} for the full χ range is given as follows:

$$\begin{aligned} M_{CT2}^{max2} &= 2\chi^2 + |\bar{\delta}_T|^2 \qquad \text{for } \chi \leq \chi_* & (2.4)\\ &= \chi^2 + 2\alpha(|\bar{\delta}_T| - \alpha) + 2\alpha\sqrt{\chi^2 + (|\bar{\delta}_T| - \alpha)^2} \\ &\qquad\qquad \text{for } \chi \geq \chi_* & (2.5) \end{aligned}$$

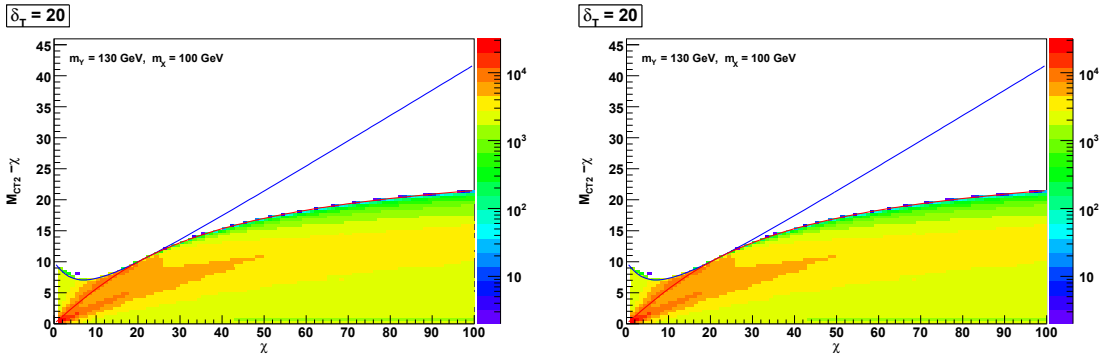

Figure 2.1: a) $M_{CT2}^{max}(\chi)$ for $(m_Y, m_X) = (130, 100)\,\mathrm{GeV}$ and $\delta_T^* = 247.9\,\mathrm{GeV}$ with $\delta_T = 20$ ($\chi_* = 21.8\,\mathrm{GeV}$). b) $M_{CT2}(\chi)$ distribution for $\delta_T = 250\,\mathrm{GeV}$ (no ${}^2BK$).

On the other hand, if χ_* is imaginary, $M_{CT2}^{max}(\chi)$ just follows the line given by Eq. (2.5). The two maximal curves of Eq. (2.4,2.5) come into contact at χ_* with the same inclination, but the curvature of $M_{CT2}^{max}(\chi)$ is discontinuous at $\chi = \chi_*$. For given parameters (m_Y,m_X,δ_T), χ_* is real and observable if

1. $\frac{m_X}{m_Y} \leq \frac{1}{\sqrt{2}}$, then $\chi_* \in \mathbf{R}$.
2. $\frac{1}{\sqrt{2}} < \frac{m_X}{m_Y} < 1$, then $\chi_* \in \mathbf{R}$ if $\delta_T \leq \delta_T^*$,
   where $\delta_T^* \equiv 4|\alpha_0|/\sqrt{1 - \frac{4|\alpha_0|}{m_Y}}$.

Although the reality condition of χ_* for the existence of a ${}^2BK$ is not always met, it can be made to appear by concentrating on events with relatively small values of $|\delta_T|$. Since $\delta_T^* > 4|\alpha_0|$, the ${}^2BK$ appears with a conservative choice of $\delta_T < 4|\alpha_0|$. The spectrum for Fig. (2.1) belongs to the second category of reality condition with $\delta_T^* = 247.9\,\mathrm{GeV}$. For the choice of events with small $\delta_T = 20\,\mathrm{GeV}$, there is a ${}^2BK$ present at $\chi_* = 21.8\,\mathrm{GeV}$. In Fig. (2.1b), $\delta_T = 250\,\mathrm{GeV} > \delta_T^*$, so no ${}^2BK$ arises. Whenever a ${}^2BK$ exists, there is a boost-trapped distribution with $\chi < \chi_*$ for which the boundaries are independent of any physical masses in the decay system, as shown in Eq. (2.4).

The shift of $M_{CT2}^{max}(\chi)$ for a change in δ_T can be sizable even for moderate values of non-zero δ_T. This is the most significant property of $M_{CT2}^{max}(\chi)$ for mass measurement. The rates of $M_{CT2/T2}^{max}(\chi)$ shift with respect to a change in δ_T are given as follows:

$$\frac{\partial M_{CT2R/T2R}^{max}}{\partial|\bar{\delta}_T|} \quad \text{for } \chi > \chi_* \text{ or } \chi > m_X \tag{2.6}$$
$$= \frac{\alpha E_\chi}{M_{CT2R/T2R}^{max} E_Y} \left\{1 \pm \frac{|\bar{\delta}_T| - \alpha}{E_\chi}\right\} \left\{1 \pm \frac{E_Y - \alpha}{E_\chi}\right\},$$

for $M_{CT2/T2}$, respectively, with $E_\chi \equiv \sqrt{\chi^2 + (|\bar{\delta}_T| - \alpha)^2}$ and $M_{T2R}^{max2} = \chi^2 - 2\alpha(|\bar{\delta}_T| - \alpha) + 2\alpha E_\chi$. Here the subscript letter R denotes the maximum curves for the χ values larger than the corresponding kink position, χ_*/m_X. The M_{T2R}^{max} results from the EKC $-$ **b**) [33] and the only difference with Eq. (2.5) is the flipped sign of the second momentum product terms. This sign-flipped maximum of M_{CT2} originates from the definition (2.1), and in [35] it has been utilized to get a compact distribution in which the endpoint singularity structures are highly amplified and accentuated for the case of $\delta_T = 0$. The flipped sign also provides an interesting result for the $\delta_T \neq 0$ case: the δ_T-shift of the maximal point can be magnified as indicated in Eq. (2.6). *In particular, when the mass difference between M_Y and M_X is small enough* so that $|\bar{\delta}_T| > \alpha$ for a moderate value of $|\bar{\delta}_T|$, the shift can be large. Fig. (2.2a) shows how much the δ_T-shift of the M_{CT2}^{max} can be amplified compared to

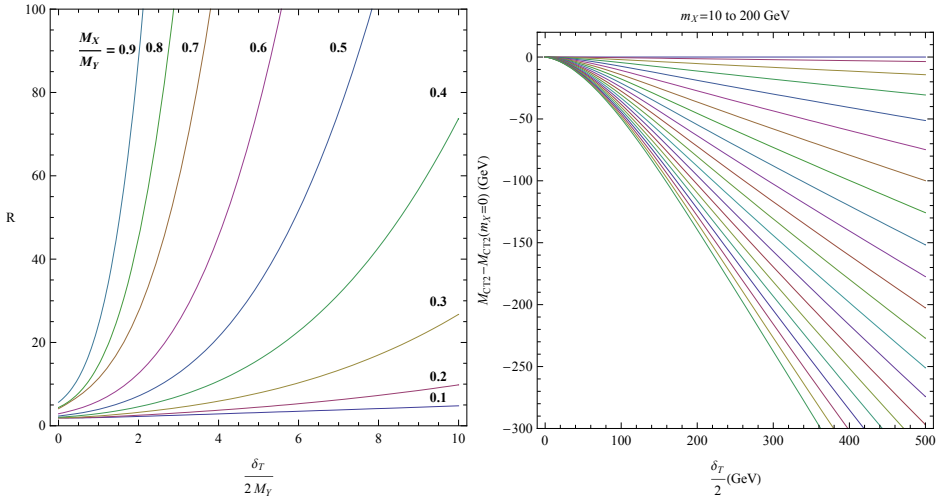

Figure 2.2: a) Ratios of δ_T-shift between M_{CT2}^{max} and M_{T2}^{max} with respect to δ_T/M_Y for various mass spectra, M_X/M_Y. b) δ_T-shift of $M_{CT2}^{max} - M_{CT2}^{max}(m_X = 0)$ for $m_X = (10 - 190)\,\mathrm{GeV}$ with the $\alpha_0 = 62.4\,\mathrm{GeV}$ and the trial LNP mass, $\chi = \chi_* + 50\,\mathrm{GeV}$.

that of M_{T2}^{max}. We define R as

$$R(\frac{|\bar{\delta}_T|}{M_Y}, \frac{M_X}{M_Y}) \equiv \frac{M_{CT2}^{max}(\chi_1, |\bar{\delta}_T| + \Delta) - M_{CT2}^{max}(\chi_1, |\bar{\delta}_T|)}{M_{T2}^{max}(\chi_2, |\bar{\delta}_T| + \Delta) - M_{T2}^{max}(\chi_2, |\bar{\delta}_T|)}.$$

We take $\Delta = M_Y/2$, χ_1 =(2χ_* calculated for $|\bar{\delta}_T| = |\bar{\delta}_T| + \Delta$ for $M_X/M_Y = 0.1 - 0.7$, $M_X + M_Y/2$ for $M_X/M_Y = 0.8 - 0.9$). χ_2 is set to $M_X + M_Y/2$ in Fig. (2.2a). This clearly shows a δ_T-shift enhancement in $M_{CT2}^{max}(\chi, \delta_T)$. The optimal choices of $\chi_{1,2}$, for which each of the shifts is maximized and well-measured, are ambiguous. We chose $\chi_1 \sim O(\chi_*)$ because it is always observed to provide sizable shift with sharp endpoint structures of the M_{CT2} distributions. However, a practical choice of χ_2 was quite difficult. Indeed, as we take larger value of χ_2, the denominator of R increases up to some value in principle,

reducing R down to $O(1)$ in some cases. However, as seen in Fig. (2.3d), there are usually faint long tails near the expected endpoint for the M_{T2} distribution with large δ_T, making it difficult to measure the endpoint and the shift even with large χ and sizable Δ.

It is also worthwhile to check some real scale values of the shift in $M^{max}_{CT2/T2}(\chi)$. For $(M_Y, M_X, |\bar{\delta}_T|, \Delta) = (150, 100, 100, 100)|(500, 100, 100, 100)$, $\Delta M^{max}_{CT2}(\chi = \chi_*) = 73.5|38.4\,\mathrm{GeV}$, while $\Delta M^{max}_{T2}(\chi = 200\,\mathrm{GeV}) = 12.7|11.6\,\mathrm{GeV}$. Fig. (2.2b) also shows the δ_T-shift of $M^{max}_{CT2} - M^{max}_{CT2}(m_X = 0)$ for various missing LNP masses, $m_X = (10 - 190)\,\mathrm{GeV}$ while the α_0 is fixed by $62.4\,\mathrm{GeV}$ and the trial LNP mass, $\chi = \chi_* + 50\,\mathrm{GeV}$. For $\delta_T = 0$, no resolution power exists as expected; however, one can see that the δ_T-shift of M^{max}_{CT2} can be large enough to measure the new particle masses with the resolution of $O(1 - 10)\,\mathrm{GeV}$ for $\delta_T \sim O(10 - 100)\,\mathrm{GeV}$. It is also enhanced for the large m_X/m_Y case. We fixed the α_0 because it is the basic momentum scale we can observe in detector regardless of the mass spectra. It can be also measured by $M^{max}_{T2/CT2}$ for $\delta_T = 0$.

These illustrations indicate that the M_{CT2} shifts might be experimentally feasible with clear endpoint structures, because the shifts can be well beyond typical experimental uncertainties. This is the power of using the M_{CT2} variable. By projecting events in the $M_{CT2}(\chi \sim O(\chi_*), \delta_T \neq 0)$ basis, one can get a more sharper edged and δ_T-sensitive event distribution. The flipped sign in the definition of the M_{CT2} variable makes the distribution compact with respect to the internal momentum scale of the system, while being much more sensitive for the external boost momentum δ_T, like a flubber ball. This means that one can have a better chance to measure both of the masses in a boosted decay system at hadron colliders, by observing the $M^{max}_{CT2}(\chi)$ for several (at least two) different δ_T values.

2.3 A SUSY Example

Having explained the properties of $M_{CT2}(\chi, \delta_T \neq 0)$ distribution, let us now check and employ it for the mass measurement of a pair of $\tilde{\chi}_1^\pm$ decay system in a SUSY model. Here we focus on the decay channel, $\tilde{\chi}_1^\pm \to \tilde{\nu} + \ell^\pm$. The chargino decay is rather difficult to reconstruct in usual methods because of the missing neutrinos in the cascade decay following the process. In mSUGRA prejudice, $\tilde{\chi}_1^\pm$ decays dominantly into $\tilde{\tau}$, through its left-right mixing and branching ratio into the decay mode is small. However, the $\tilde{\chi}_1^\pm$ can be heavier than the $\tilde{\nu}$ in non-minimal models. For example, a model where 3rd generation sfermions are heavy and left-handed sleptons are lighter than $\tilde{\chi}_1^\pm$ was proposed recently in [37] to solve the SUSY flavor problem. We take a benchmark point of the paper where $(m_{\tilde{g}}, m_{\tilde{q}_R}, m_{\tilde{q}_L}, m_{\tilde{\chi}_1^\pm}, m_{\tilde{\chi}_2^0}, m_{\tilde{l}_L}, m_{\tilde{\nu}}, m_{\tilde{\chi}_1^0})$ = (724.9, 624.1, 645.6, 231.5, 231.4, 175.9, 157.2, 123.3) GeV. For this point, $BR(\tilde{\chi}_1^\pm \to \tilde{\nu} + \ell^\pm | \tilde{l}_L^\pm + \nu_\ell) \sim (0.63|0.34)$.

We simulated SUSY event production of $25 fb^{-1}$ at the LHC energy of 14 TeV using the PYTHIA Monte Carlo event generator [38] with ISR/final state radiation turned on. Fully showered and hadronized events were passed to the PGS4 [39] detector simulator. The energy resolution parameter in the hadronic calorimeter was given by $\Delta E/E = 0.6/\sqrt{E}$, and jets were reconstructed using a cone algorithm with $\Delta R = 0.5$. We chose same sign

(SS) dileptonic events with $N(\geq 2)$-jets + $\not{E}_T$. The SS dilepton condition can efficiently remove various dileptonic backgrounds from SUSY neutralino decays and SM processes such as $t\bar{t}$, WW, $W/Z + jets$. The event selection cuts are as follows: SS dilepton with $P_T(\ell_{1,2}) > 20\,\mathrm{GeV}$, $P_T(jet_{1,2}) > (100, 80)\,\mathrm{GeV}$, $\not{E}_T > 100\,\mathrm{GeV}$. Using these cuts, the signal to background ratio becomes high and the endpoint is expected to appear clearly without pollution from the SM process and neutralino decays [40]. Since $\tilde{\chi}_1^\pm$ has large branching ratios in two different channels, there exist three types of dilepton signal from a pair of $\tilde{\chi}_1^\pm$ decay chains. The 1st type is the case where the both leptons come from $\tilde{\chi}_1^\pm \to \tilde{\nu} + \ell^\pm$ decays and the 2nd type is when both are from $\tilde{\chi}_1^\pm \to \tilde{l}_L^\pm + \nu_\ell$ with $\tilde{l}_L^\pm \to \ell^\pm + \tilde{\chi}_1^0$, subsequently. The 3rd is the mixed case of 1st and 2nd type leptons. Thus, we can expect that there are 3 types of different endpoints in the inclusive dileptonic M_{CT2} distribution. However, in this benchmark point it was found that the 1st type of dilepton provides the largest endpoint for $M_{CT2}(\chi, \delta_T)$ [41], and here we simply applied our method to determine both the $m_{\tilde{\chi}_1^\pm}$ and $m_{\tilde{\nu}}$. Using the dileptons M_{CT2} was calculated by its definition, Eq. (2.1), with extra jets considered as δ_T. Fig. (2.3a) shows the δ_T distribution for the dilepton + $\not{E}_T$ system in the benchmark point. The first peak in the distribution is from direct weakly interacting gaugino pair production and most of the large δ_T values are from decays of colored superparticles. The δ_T profile shows that the event statistics of $\delta_T \sim O(100)\,\mathrm{GeV}$ are quite rich so that one might practically observe the endpoints and their shifts in the M_{CT2} distribution using events with few hundred GeV of δ_T. We made plots of the M_{CT2} distributions with various χ values using events with δ_T bounded by some maximal value, δ_T^{max}. Because the endpoint increases with respect to δ_T, it is given by $M_{CT2}^{max}(\chi, \delta_T^{max})$ with inclusive event samples. Fig. (2.3c) illustrates such $M_{CT2}(\chi, \delta_T < \delta_T^{max})$ distributions. Here two values of $\delta_T^{max} = (200|400)\,\mathrm{GeV}$ cuts are used, and each corresponds to dashed and solid distributions, respectively. The ${}^2BK$ position for each δ_T^{max} cases are calculated as $\chi_* = (94.8|120.7)\,\mathrm{GeV}$, and we include several plots of $\chi = (0_{(green|green)}, \chi_* + 10_{(magenta|yellow)})\,\mathrm{GeV}$ for $\delta_T^{max} = (200|400)\,\mathrm{GeV}$, respectively. As seen in the plot, the M_{CT2} endpoints for various (χ, δ_T^{max}) values are found clearly near the expected position (arrows) so that we could reconstruct the $M_{CT2}^{max}(\chi, \delta_T^{max})$ with tolerable errors. The shift between the M_{CT2} distributions for different δ_T^{max} cuts is visibly apparent. For example, in the $\chi = \chi_* + 10\,\mathrm{GeV}$ case, $M_{CT2}^{max}(\chi, 200)$ and $M_{CT2}^{max}(\chi, 400)$ show clearly measurable shifts larger than about $60\,\mathrm{GeV}$. It is also true for the other values of $\chi \sim \chi_*$. We also tested the $M_{T2}(\chi, \delta_T^{max})$ distribution with same event sample and cuts. Fig. (2.3d) presents the result of M_{T2} case. It had larger ambiguities in pinpointing the expected endpoints, $(87.8|112.2)\,\mathrm{GeV}$, and measuring the shift so that it was hard to reconstruct $M_{T2}^{max}(\chi, \delta_T^{max})$ precisely. Based on the plots of $M_{CT2}(\chi, \delta_T^{max})$, we fitted the endpoints with simple linear functions, and $M_{CT2}^{max}(\chi, \delta_T^{max})$ was reconstructed by segmented-fitting with Eq. (2.4,2.5). Fig. (2.3b) shows the reconstructed lines (Green) and expected maximal lines (Red, Blue) for two $\delta_T^{max} = (200|400)$ cases. The two α values could be extracted quite precisely by $\alpha^{(1,2)} = (132.6 \pm 3.4,\ 92.4 \pm 2.5\,\mathrm{GeV})$. Using this result, the masses of $\tilde{\chi}_1^\pm$ and $\tilde{\nu}$ were resolved to be $(m_{\tilde{\chi}_1^\pm}, m_{\tilde{\nu}}) = (231.2 \pm 9.9, 159.3 \pm 5.9\,\mathrm{GeV})$. Systematic errors were not considered in this analysis.

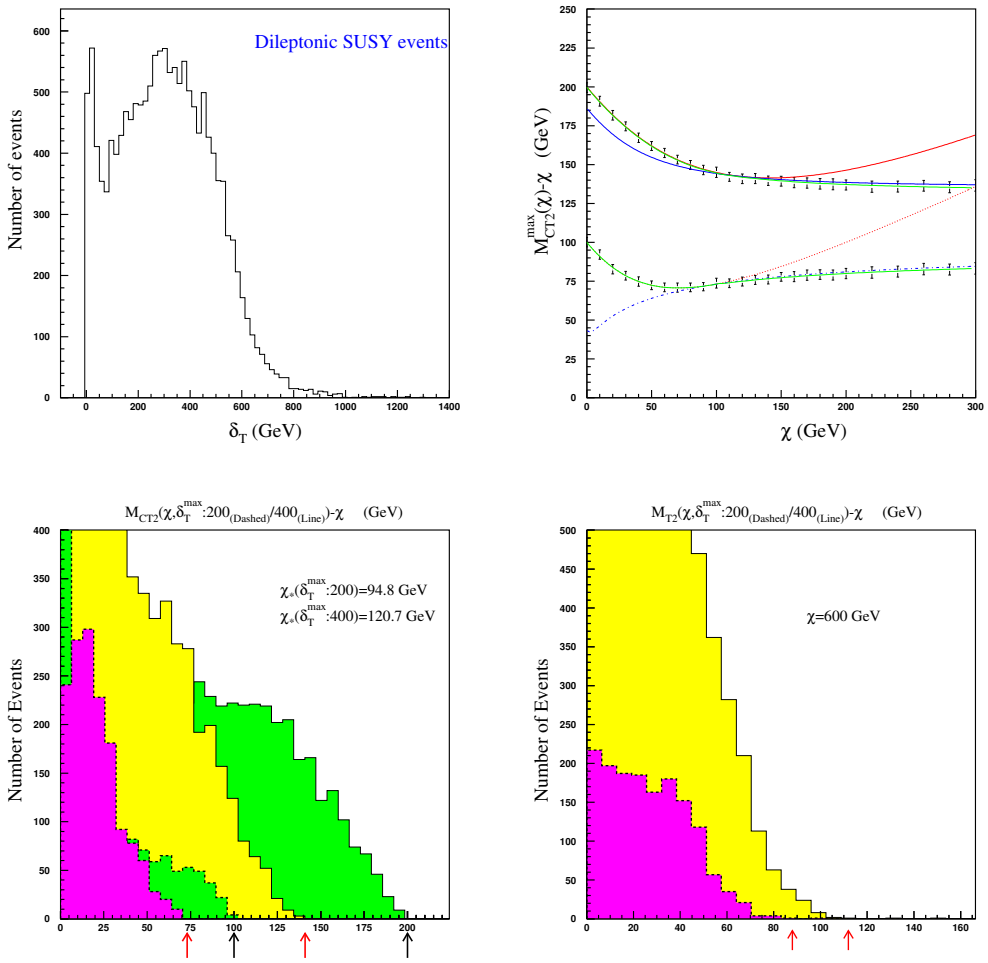

Figure 2.3: Top: a) δ_T distribution for dilepton + $\not{E}_T$ system b) Reconstructed $M_{CT2}^{max}(\chi, \delta_T^{max} = 200|400\,\text{GeV})$ Bottom: c) M_{CT2} and d) $M_{T2}(\chi = 600)$ distributions for $\delta_T^{max} = (200_{dashed}|400_{solid})\,\text{GeV}$. The χ for $M_{CT2}(\delta_T^{max} = 200|400)$ are $0_{(green|green)}, \chi_* + 10_{(magenta|yellow)}\,\text{GeV}$, respectively.

2.4 Conclusion

We have demonstrated the effectiveness of the M_{CT2} variable for mass determination in boosted single-step decay chains. The M_{CT2} projection makes the distribution compact with respect to the internal momentum scale, and it is sensitive to the external momentum. This can be utilized to measure the masses in boosted decay systems with a pair of symmetric decay chains, which we have demonstrated for a particular SUSY model. The

technique also works for a single mother particle decay system with non-zero transverse momentum. We now turn from our discussion of mass measurement to a new technique for spin determination in Chapter 3.

Chapter 3

Discriminating Spin Through Quantum Interference

Many of the proposed solutions to the hierarchy and naturalness problems postulate new "partner" fields to the Standard Model (SM) particles, as discussed in Section 1.3. Determining the spins of these new particles will be critical in distinguishing among the various possible SM extensions, yet proposed methods rely on the underlying models. We propose a new model-independent method for spin measurements which takes advantage of quantum interference among helicity states. We demonstrate that this method will be able to discriminate scalar particles from higher spin states at the ILC, and discuss application to higher spins and possible uses at the LHC.

3.1 Introduction

The Large Hadron Collider (LHC) is now up and running, granting us at long last access to the scale of electroweak symmetry breaking and beyond. One of the major puzzles we hope the LHC may provide answers to is the hierarchy problem [42][43][44][45]: the origin and stability of the orders of magnitude gulf between the Higgs vev at ~ 300 GeV and the Planck scale at $\sim 10^{19}$ GeV. Without experimental results, theorists over the years have collected an impressive array of possible solutions to this problem. Arguably, the leading contender is supersymmetry [46], but there are many others: extra dimensions [28][47][48][49][50][30][51], technicolor [52][43][44], and little Higgs [53] to name a few. Many of these models also provide a long-lived, weakly coupled particle suitable to be a dark matter candidate.

In many of these possibilities the immediate experimental signature from the LHC would be the presence of beyond the Standard Model particles partnered with some or all of the known particles. For example, the minimal supersymmetric standard model (MSSM) doubles the number of particles by adding a new field with the same gauge quantum numbers and Yukawa couplings as in the SM, but spins differing by one half of a unit. Alter-

natively, the minimal universal extra dimensions (UED) model [31] has compactified extra dimensions which solve the hierarchy problem by "ending physics" at the scale of electroweak symmetry breaking. That is, the Planck scale of the true $4+d$ dimensional theory is not far above a TeV, but appears much larger in 4D once the compactification occurs. This results in a tower of KK states, each containing a heavier version of the SM particles with identical quantum numbers, including spin.

It is well known that, due to the similarities in the particle spectrum and quantum numbers, it may be difficult to distinguish the signatures of MSSM particles from the KK=1 modes of UED at future collider experiments [54][55]. The existence of the KK=2 modes could serve as a discriminator between supersymmetry and extra dimensions, but their high masses may make them kinematically inaccessible. Even if produced, they typically decay through KK=1 states, and so their presence would only be felt through an increase in the KK=1 production cross section [56][57]. Determining the spin of the new particles will be necessary to confirm the theory underlying any new particles.

There have been several proposals for measuring spin in future collider experiments. The possibilities at a linear collider are far more numerous, due to the control over the center of mass energy in each event. Threshold scans can distinguish scalars from spinors or vector bosons, as the former cross section rises like β^3 while the latter two are proportional to β [58]. However, such a method cannot be used at a hadron collider, and cannot discriminate between spin 1/2 and spin 1. The differential cross section with respect to production angle in s-channel pair produced scalars is proportional to $\sin^2\theta$, while for spinors it is $1+\frac{E^2-m^2}{E^2+m^2}\cos^2\theta$. Model dependence may be present in the form of t-channel diagrams, which introduce a forward peak which is similar for both spin statistics [58]. Such diagrams make the production angle measurement of spin more difficult, but may be possible in some cases [59].

The polar angular dependence in decays can also be used for spin measurements. However, extracting spin from these measurements assumes knowledge of the final state spins and also requires chiral couplings, introducing a model dependence on the spin measurement [60]. While this method was originally proposed for the International Linear Collider (ILC), it was shown that, with sufficiently long decay chains and exploitation of the asymmetry in production of squarks versus antisquarks, supersymmetric spinors could be distinguished from phase space decays at the LHC [56][60][61][62][63][64]. Yet this method relies heavily on the underlying models as the entire decay chain must be considered.

Clearly, determination of spin is a problem still requiring novel solutions. In this paper we investigate a model-independent method to determine the spin of new particles at the ILC, first proposed in [65]. Through interference between the different helicity states in a coherent sum, the cross section of pair produced particles decaying to two-body final states develops a non-trivial dependence on the azimuthal angle ϕ of the decay. By extracting this dependence, one can determine which helicity states entered into the sum, and thus the spin of the decaying particle. This method is similar to (and was inspired by) the determination of the quark spin measurement at SPEAR [66]. At the end of this paper, we will discuss how this general method may be extended to the LHC.

This chapter is organized as follows. In Section 3.2 we derive the angular dependence of the cross section as a function of particle spin. We then determine appropriate experimental quantities and develop the necessary measurement techniques. In Section 3.3 we apply our method to distinguish scalars in pair production at the ILC from production of higher spin states. Spin 1/2 and 1 measurements are considered in Section 3.4, and we conclude in Section 3.5. Additional calculations are supplied in the Appendices.

3.2 Azimuthal Angular Dependence

To determine the azimuthal dependence of the cross section for pair production followed by decay, we start with a particle of helicity h moving in the $\hat{z}$ direction. When this decays into a two-body final state, the momenta of the daughter particles are confined to a decay plane. If we consider the rotation of this plane about the $\hat{z}$ axis by an angle ϕ, it is clear that the action of the rotation on the matrix element of the decay must be equivalent to the action of the rotation on the parent particle.

Rotations of the particle about the $\hat{z}$ axis introduce a phase $e^{-iJ_z\phi}$, where J_z is the total angular momentum in the $\hat{z}$ direction. However, as the momentum is defined to be in the $\hat{z}$ direction, the orbital component is zero, and J_z reduces to h:

$$J_z = \frac{(\vec{s} + \vec{x} \times \vec{p}) \cdot \vec{p}}{|\vec{p}|} = \frac{\vec{s} \cdot \vec{p}}{|\vec{p}|} = h. \tag{3.1}$$

Therefore, the dependence of the decay matrix element $\mathcal{M}_{decay}$ on ϕ must be

$$\mathcal{M}_{decay}(h, \phi) = e^{ih\phi}\mathcal{M}_{decay}(h, \phi = 0). \tag{3.2}$$

Were we to produce particles in only one helicity state, then the total cross section (proportional to the square of $\mathcal{M}_{prod.}\mathcal{M}_{decay}$) would be independent of ϕ. However, if two or more helicity states are produced and then decay, the total cross section is proportional to the coherent sum squared:

$$\sigma \propto \left| \sum_h \mathcal{M}_{prod.}(h) e^{ih\phi} \mathcal{M}_{decay}(h, \phi = 0) \right|^2 . \tag{3.3}$$

This expression is true only within the validity of the narrow-width approximation. However, for "weakly-coupled" physics, such an approximation is justified [67].

As a result of this interference among the various helicity states, the cross section develops a $\cos(n\phi)$ dependence, where n is an integer running from zero to twice the largest value of h for the decaying particle. That is to say, the ϕ dependences for a scalar, spinor, and massive vector boson can be written as

$$\sigma(s = 0) = A_0 \tag{3.4}$$

$$\sigma(s = 1/2) = A_0 + A_1 \cos(\phi) \tag{3.5}$$

$$\sigma(s = 1) = A_0 + A_1 \cos(\phi) + A_2 \cos(2\phi), \tag{3.6}$$

where the A_i are not functions of ϕ (though they are non-trivial functions of the other kinematics of the problem). The exact forms of the cross section must be worked out from the standard rules of constructing matrix elements from Feynman diagrams, in which case the ϕ dependence will become apparent. However, from this general argument the relationship between spin and ϕ dependence is made clear.

To exploit this ϕ dependence, we consider pair production of particles from e^+e^- at the future ILC. As motivated by solutions to the dark matter problem, we expect the production of beyond the SM particles to cascade down to some weakly coupled particle which will escape the detector. Such WIMPs are present in the supersymmetric spectrum as the lightest supersymmetric particle (LSP), typically the lightest neutralino, or in universal extra dimensions as the lightest Kaluza-Klein odd particle (LKP), typically the B_1. Examples of such event topologies in the UED and SUSY models are shown in Fig. 3.1. However, our methods do not rely on such specific models.

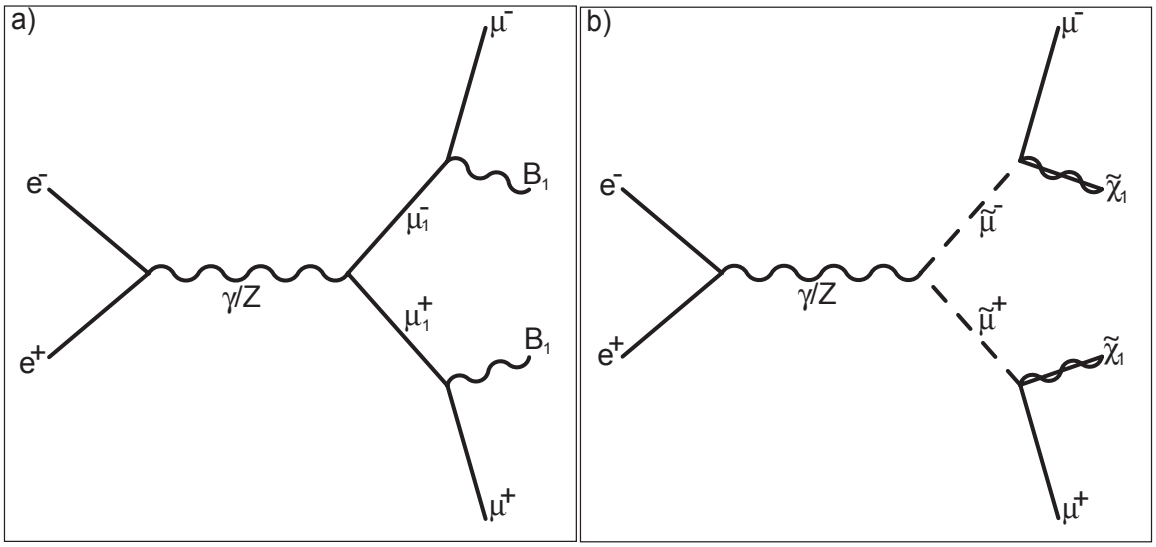

Figure 3.1: a) Pair production of $\mathrm{KK} = 1$ muons in universal extra dimensions decaying to opposite-sign muons and missing energy in the form of two B_1 gauge bosons (the LKP). b) Pair production of smuons in supersymmetry decaying to opposite-sign muons and the lightest neutralinos as LSP missing energy.

Measuring the azimuthal dependence of the cross section requires that we are able to reconstruct the momentum of the parent particle. For simplicity, we specialize to cases where the pair produced particles each decay to a charged lepton and missing energy, in which case the events of interest consist of $\ell^{\pm}\ell^{\mp}\not{E}$. While we risk losing some model independence at this stage, such signatures are fairly generic in many extensions to the SM.

Let the pair produced particles whose spin we wish to measure (μ_1 in Fig. 3.1a or $\tilde{\mu}$ in Fig. 3.1b) have 4-momenta p_A and p_B and mass M . These particles each decay to visible

(effectively massless) leptons and a weakly coupled particle with mass m (the $\tilde{\chi}_1^0$ or B_1 in Fig. 3.1). We label the visible lepton momenta p_1 and p_2, and assume that the particles running in each leg are identical. The production angle θ and decay angles θ_i and ϕ_i ($i = 1$ for the decay of A and $i = 2$ for the decay of B) defined relative to the production plane are shown in Fig. 3.2.

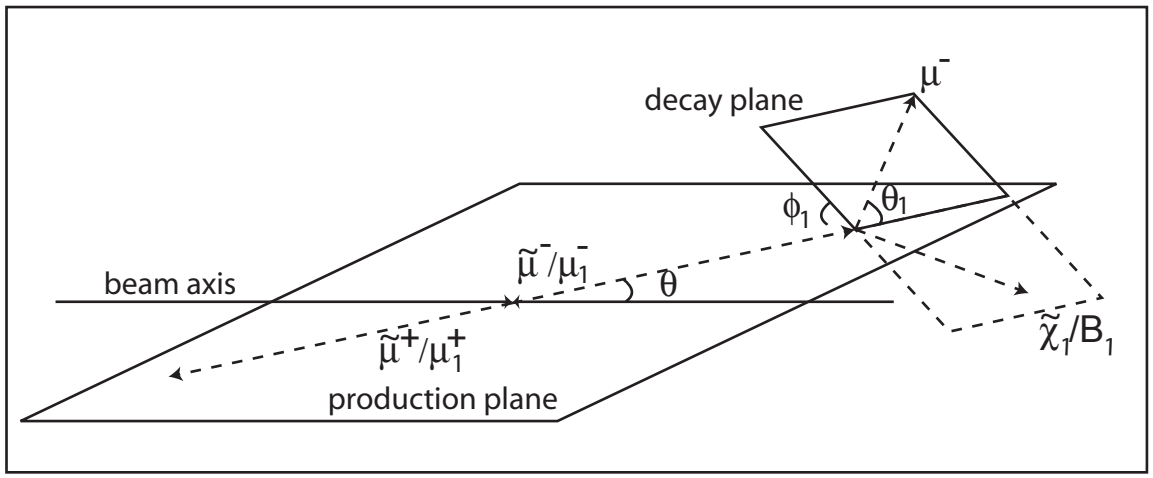

Figure 3.2: The pair produced $\tilde{\mu}$ or μ_1 in the lab frame. The beam axis is defined as the z axis, with the production angle θ in the $x-z$ plane. The $\hat{z}$ axis is defined to point along the production axis. The decay angle ϕ_1 is invariant to boosts along $\hat{z}$, and so may be defined in either the lab frame or the frame of the decaying particle. The angle θ_1 is defined in the rest frame of $\tilde{\mu}^-/\mu_1^-$. Decay angles θ_2 and ϕ_2 (not shown) are defined equivalently for the $\tilde{\mu}^+/\mu_1^+$.

At the ILC, assuming knowledge of the masses M and m, it is possible to completely reconstruct the 4-momenta p_A and p_B (and thus the angles ϕ_1 and ϕ_2) up to a two-fold ambiguity [68][69]. We note that there are 4 unknown values for both of the missing particles in the decay, for a total of 8 unknowns. There are 4 measured values of the total missing 4-momentum $\not{p}$; and for each massive particle in the diagram there is a mass relation, for a total of 4 constraints. Therefore, one would expect this event to be completely reconstructible. When solving the mass relations, however, one finds an ambiguity in sign when taking a square root, leading to the two-fold ambiguity in the reconstructed momentum. For the details of the reconstruction, see Appendix A.1.

With less than perfect knowledge of the masses, muon momenta, and center of mass energy (from beamstrahlung [70] and initial state radiation), the true solution will not be reconstructed perfectly. At the ILC, masses of lepton and gaugino partners are expected to be measured to one part per mille [71][72], the tracking resolution as good as $\sim 5 \times 10^{-5}(p_T/\text{GeV})$ [73], and beamstrahlung/initial state radiation (ISR) should be a few percent [74]. As such, we expect that the errors introduced in ϕ from these effects will be minimal.

As we have two solutions for the momenta p_A and p_B, this leads to two solutions each for ϕ_1 and ϕ_2. The extracted signal in the azimuthal distribution is therefore obtained in the combination of the true and false solutions and compared to the expected values given in Eqs. (3.4), (3.5), and (3.6). In particular, a particle of spin $n/2$ should have $A_i = 0$ for all $i > n$.

3.3 Scalars vs. Spinors

To demonstrate the utility of this method of spin determination, we consider the pair production of scalar right-handed smuons in supersymmetry which decay to muons and LSP $\tilde{\chi}_1^0$s ($e^-e^+ \to \tilde{\mu}_R^-\tilde{\mu}_R^+ \to \mu^-\mu^+\tilde{\chi}_1^0\tilde{\chi}_1^0$). We compare the azimuthal distributions of ϕ_1 and ϕ_2 in this scenario to that in the pair production of μ_{1R}s decaying to muons and LKP B_1s in a UED model ($e^-e^+ \to \mu_{1R}^-\mu_{1R}^+ \to \mu^-\mu^+B_1B_1$). The Feynman diagrams for these processes are shown in Fig. 3.1. Analytic formulae for the production and decay cross sections for both models are presented in Appendix A.2. We stress that SUSY and UED are chosen only as benchmark models with differing spins and similar final states; the method used to determine spin can in principle work equally well for any other scenario.

Representative spectra are required for both supersymmetry and universal extra dimensions. In addition, we wish to avoid any possible model-specific effects on the azimuthal distributions arising from different choices of spectra for supersymmetry and extra dimensions. Therefore, as the masses of the $\tilde{\mu}/\mu_1$ and $\tilde{\chi}_1^0/B_1$ are assumed to be known, we perform our analysis twice for each model. In the first case we assign the masses of the μ and B partners as per a SUSY spectrum, and then repeat the processes with the UED case.

As a representative supersymmetry point, we chose SPS 3 [75][76] in mSUGRA parameter space, which has $m_0 = 90$ GeV, $m_{1/2} = 400$ GeV, $A_0 = 0$, $\tan\beta = 10$, and a positive μ parameter. Universal extra dimensions are represented by the minimal version (MUED) [77], which requires only four parameters: the number and radius R of the extra dimensions, the scale Λ to set flavor-universal boundary terms equal to zero, and the Higgs mass. We chose one extra dimension with $R^{-1} = 300$ GeV, $\Lambda = 20R^{-1}$, and a Higgs mass of 120 GeV. The resulting particle spectra at the TeV scale are shown in Table 3.1.

Backgrounds consist of the standard model production of W^-W^+ pair production with leptonic decays to muons and neutrinos, ZZ production with decays to muons and neutrinos, and model-background of $\tilde{\chi}_1^+\tilde{\chi}_1^-/W_1^+W_1^-$ production decaying to muons and $\tilde{\nu}/\nu_1$. While kinematic cuts on the invariant mass of the muon pairs can greatly reduce the SM background, more efficient cuts can be obtained by requiring successful reconstruction of the $\tilde{\mu}_R/\mu_{1R}$ momentum as outlined in Appendix A.1.

The reconstruction algorithm assumes that the masses of the produced and escaping particles are known. By assuming that the signature of $\mu^-\mu^+\not{E}$ arises from pair production of $\tilde{\mu}_R$ (or μ_{1R}) decaying to LSP or LKP, all other events with the same signature but different particle masses develop inconsistencies in their reconstruction. That is, the visible momenta are not compatible with the pair production of particles with masses other than

	SPS 3	MUED
$\tilde{\chi}_1^0/B_1$	161 GeV	302 GeV
$\tilde{\ell}_R/\ell_{1R}$	181 GeV	304 GeV
$\tilde{\ell}_L/\ell_{1L}$	289 GeV	309 GeV
$\tilde{\chi}_1^\pm/W_1^\pm$	306 GeV	327 GeV
$\tilde{\nu}_\ell/\nu_{1\ell}$	276 GeV	309 GeV

Table 3.1: Relevant particle spectra for the mSUGRA parameter point SPS 3 and the minimal universal extra dimension parameters $R^{-1} = 300$ GeV, $\Lambda = 20R^{-1}$ and $m_H = 120$ GeV. The MUED spectrum was derived using the MUED package [78] for CalcHEP [79]. Here ℓ refers to the light charged leptons: electrons or muons.

that for the $\tilde{\mu}_R/\mu_{1R}$ decaying into particles with masses other than that of the LSP/LKP. In practice, the parameter y defined in Eq. (A.11) becomes imaginary.

With perfect knowledge of masses and muon momentum, requiring reconstruction to succeed cuts nearly all of the background events. Once detector smearing and mass measurement errors are included, it is inevitable that some background will survive the reconstruction cut. Again, with the small errors in mass measurements to be available at the ILC, we do not expect large backgrounds to pollute the data set.

The total center of mass energy at the ILC is expected to reach up to 1 TeV, and an integrated luminosity of 500 fb^{-1} is not unrealistic. For the mass spectra chosen, the resulting cross sections times branching ratios are shown in Fig. 3.3 for $\sqrt{s}$ running from threshold up to 1 TeV. As a result, we expect several thousand to several hundreds of thousands of events available.

To simulate the effects of necessary cuts due to the geometry of the detector, we place cuts on the pseudo-rapidity η. We require η to be less than 2.5 for both visible muons, as otherwise the leptons would vanish unseen down the beam. Also, if the missing momentum also points down the beam pipe, we cannot be sure that the missing energy is truly in the form of WIMPs and not merely unobserved SM particles, so we cut on η for missing $\vec{p}_T$ as well.

Using HELAS [80] the production and decay matrix elements were calculated at tree level for each helicity state. Using the narrow width approximation, the cross sections as a function of θ, ϕ_1, θ_1, ϕ_2, and θ_2 were obtained. BASES [81], an adaptive Monte Carlo program was used to integrate over the other kinematic angles to determine the differential cross sections with respect to ϕ_1 and ϕ_2. As both decaying particles have the same spin statistics, the differential distributions are the same for both of the ϕ, and so, to increase statistics, the distributions for ϕ_1 and ϕ_2 were added.

Representative distributions for scalars and spinors (including rapidity cuts) are shown in Fig. 3.4. As can be clearly seen in Fig. 3.4a, both the true and false UED distributions have clear $\cos\phi$ dependence, as expected from spinor decay (Eq. (3.5)). The true distributions for the scalar SUSY decay in Fig. 3.4b is flat, as expected from Eq. (3.4). It is

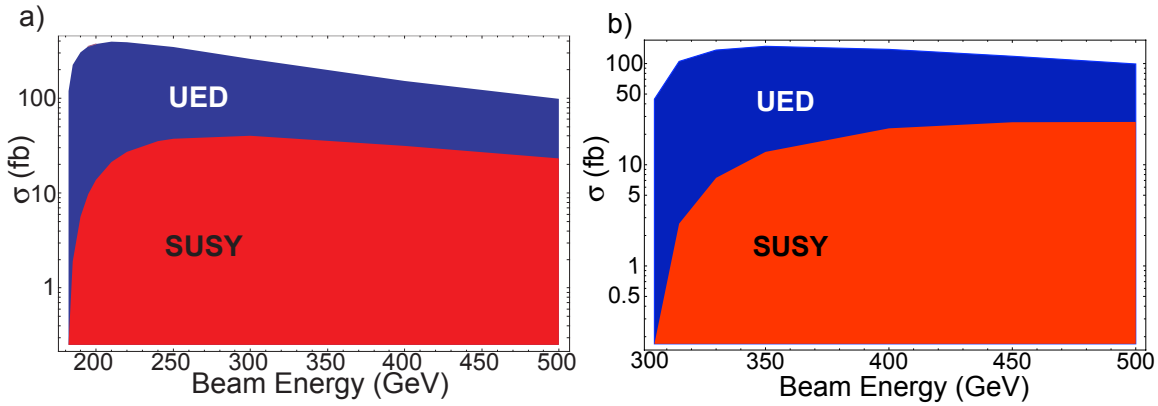

Figure 3.3: Cross sections times branching ratios as a function of the beam energy for the UED process $e^-e^+ \to \mu^-_{1R}\mu^+_{1R} \to \mu^-\mu^+ B_1 B_1$ and the SUSY process $e^-e^+ \to \tilde{\mu}^-_R\tilde{\mu}^+_R \to \mu^-\mu^+\tilde{\chi}^0_1\tilde{\chi}^0_1$. Figure a) uses the SPS 3 spectrum, while b) uses the MUED spectrum (see Table 3.1).

therefore apparent even at this level of analysis that the ϕ dependence of the distribution contains the spin information necessary for our method.

Considering the combined true and false distribution in Fig. 3.4, a systematic issue for our method becomes readily apparent. An unexpected $\cos 2\phi$ dependence develops due to the false distribution and rapidity cuts, a situation we regard as an indication of practical limitations to our method, not a fundamental flaw. Whereas the $\cos 2\phi$ dependence may be unimportant for the discrimination of scalar versus higher spin states, it will become important in distinguishing spinors from vectors (Section 3.4). Though harder to see by eye, the UED distribution also develops a $\cos 2\phi$ dependence in the false solution. As such, we fit not to $A_0 + A_1 \cos\phi$ but rather to $A_0 + A_1 \cos\phi + A_2 \cos 2\phi$.

The overall scaling of the A_i parameters in Eqs. (3.4), (3.5), and (3.6) depends on the total number of events, which is a function of the total cross section. To remove this model-dependent effect, the parameter of interest in spin determination is not A_1, but A_1/A_0, which is independent of the scaling due to total cross section.

Using the least-squares method the generated distributions were fit to $A_0 + A_1 \cos\phi + A_2 \cos 2\phi$. The errors for each parameter A_i were obtained after marginalizing over the other two parameters. The ratio A_1/A_0 for the scalar $\tilde{\mu}_R$ and spinor μ_{1R} are shown in Fig. 3.5. As can be seen, for both the SPS3 and MUED spectra the values of A_1/A_0 for $\tilde{\mu}_R$ are consistent with zero for all energies and for both the true and false distributions. For the spinor μ_{1R}, the ratio is manifestly non-zero, allowing us to distinguish scalars from higher spin states.

Several aspects of Fig. 3.5 require closer examination. The large error bars for the supersymmetric particles in both spectra are due to the relatively poor statistics compared to the pair production of the spinor KK modes in universal extra dimensions. This is especially apparent near threshold. For the spinor particles we also note that, near threshold, the signal

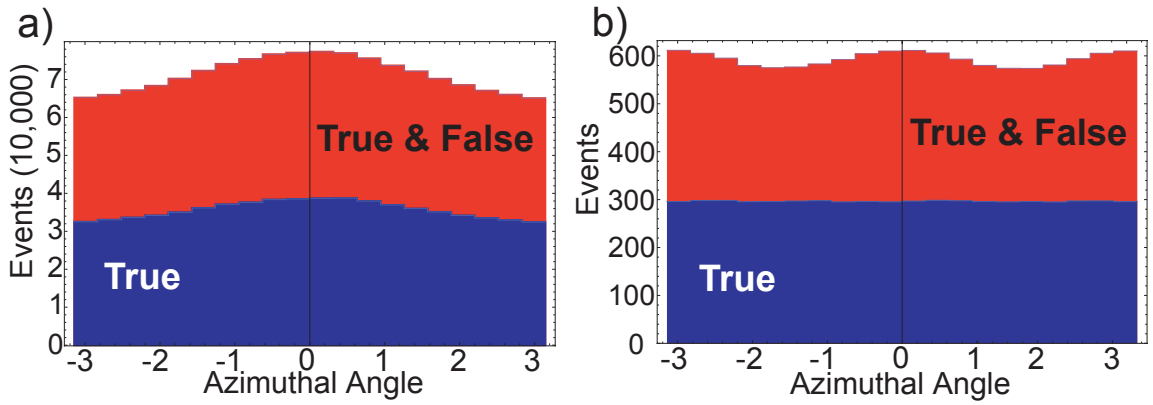

Figure 3.4: Histograms of number of events per azimuthal angle ϕ for both the true solution to the reconstruction algorithm and the combined true and false distribution. The center of mass energy is $\sqrt{s} = 370$ GeV and the luminosity if 500 fb^{-1}. Figure a) shows the UED distribution for $e^-e^+ \to \mu^-_{1R}\mu^+_{1R} \to \mu^-\mu^+B_1B_1$ while b) is the SUSY distribution for $e^-e^+ \to \tilde{\mu}^-_R\tilde{\mu}^+_R \to \mu^-\mu^+\tilde{\chi}^0_1\tilde{\chi}^0_1$.

is on the order of 10%, and decreases toward zero at progressively higher energies. This decrease can be readily explained as follows. Far from threshold, the mass of the pair produced particles becomes less relevant, and so their spins become more correlated due to chirality conservation. To determine the distribution of ϕ_1 (ϕ_2), we integrate over all other angles in the problem, including ϕ_2 (ϕ_1). Due to the correlation of spins in this energy regime, this integration results in decoherence of the sum of matrix elements. That is, rather than considering $|\sum_h \mathcal{M}(h)|^2$, at high energies the cross section becomes proportional to $\sum_h |\mathcal{M}(h)|^2$, which has no azimuthal angle dependence due to the lack of interference between terms.

Finally, in considering the distribution of true solutions versus that of the combined solutions, we note that for the spinor case the signal is less once the false solutions are added in. At low energies the difference between the two is comparatively small, but grows as we move away from threshold. This agrees well with the naive intuition that the false distribution should be flat in ϕ_1 and ϕ_2; however, we stress that at higher frequencies such intuition fails us and the flat distribution may develop non-trivial $\cos 2\phi$ dependences.

To demonstrate this effect we plot in Fig. 3.6 the ratio A_2/A_0 for the decay of spinor μ_{1R} (using SPS3 parameters). As can be seen in the top plot, the true solution without cuts has a coefficient of zero for the $\cos 2\phi$ term, as predicted by Eq. (3.5) for spinor decay. However, once cuts and the false solutions are added a non-zero value is generated. Clearly, this can cause confusion between a spin-1/2 particle and a vector or higher spin state.

To attempt to correct for this effect we generate events in which the particles decay according to phase space. This flat distribution is reconstructed using the method outlined in Appendix A.1 and rapidity cuts are applied just as in the SUSY and UED cases. As a result, the flat distributions also develop a $\cos 2\phi$ dependence. The resulting values for

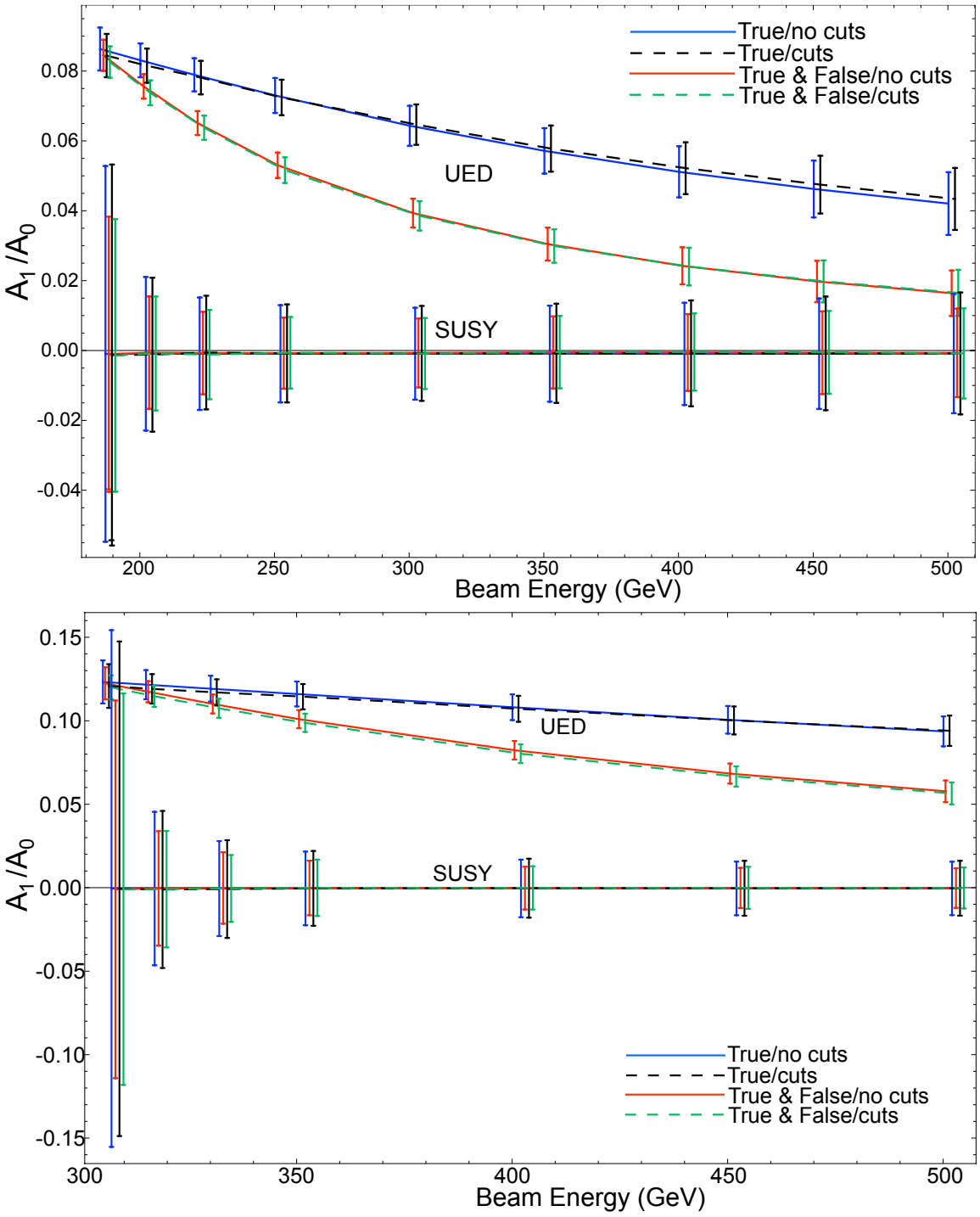

Figure 3.5: Top: Ratio A_1/A_0 for mSUGRA parameter point SPS3 as a function of energy for both scalar (SUSY) and spinor (UED) pair production with 500 fb^{-1} luminosity. Error bars correspond to 95% exclusion region. Blue lines correspond to true solution only with no rapidity cuts, black dashed lines are true solutions with rapidity cuts, red lines are true and false solutions without cuts, and green are true and false solutions with cuts. Bottom: Ratio A_1/A_0 for MUED parameters as in Table 3.1 for both scalar (SUSY) and spinor (UED) production. Color labeling identical to the above.

A_2/A_0 using only true solutions (with and without cuts) and then both solutions (with and without cuts) are subtracted from the appropriate spinor ratios to isolate the spin-dependent effect. The resulting corrected A_2/A_0 values are displayed in the lower plot in Fig. 3.6. As can be seen, the flat distribution corrects the $\cos 2\phi$ contribution due to cuts but does not remove the false distribution's effect, leaving a $\sim 0.5\%$ spurious signal at high energies. For reasons we do not yet fully understand, at low energies the false distribution's effects are minimal, allowing for the possibility of accurate spin measurements. However, it is exactly in this regime that statistics are poor due to the proximity of the threshold.

3.4 Spinor vs. Vector

Due to the large A_1/A_0 signal for non-scalars (on the order of 10%) and minimal effect of rapidity cuts and false distributions on this ratio, the ILC should have little difficulty discerning that a particle is spin-0. However, for higher spins the cuts and false solutions introduce potentially dangerous higher frequency contributions, as has been demonstrated.

As a result, the question still remains whether this method may be practically applied to discriminate spinors from vectors in general cases. We therefore consider a case of pair production of massive vector bosons in UED contrasted with spinor production in SUSY. In particular, we consider $e_L^- e_L^+ \to W_1^- W_1^+ \to \ell^- \ell'^+ \bar{\nu}_{1\ell} \nu_{1\ell'}$ in universal extra dimensions and $e_L^- e_L^+ \to \tilde{\chi}_1^- \tilde{\chi}_1^+ \to \ell^- \ell'^+ \tilde{\nu}_\ell^* \tilde{\nu}_{\ell'}$ in supersymmetry where the leptons ℓ and ℓ' can be either muon or electron type (see Fig. 3.7). Even though the $\nu_1/\tilde{\nu}$ are not the LSP/LKP, they decay to neutrinos and the LSP, neither of which is visible in the detector.

For these final states, the total cross sections times branching ratios as a function of energy are shown in Fig. 3.8. Once again, the supersymmetric cross section is considerably less than that in extra dimensions. Furthermore, the small mass splittings in the MUED spectrum lead to small cross sections compared to the SPS 3 case. Backgrounds include SM $W^\pm$ and ZZ production, and model backgrounds from $\tilde{\chi}_2^0 \tilde{\chi}_2^0 / W_1^3 W_1^3$, and $\tilde{\ell}^- \tilde{\ell}^+ / \ell_1^- \ell_1^+$ pair production decaying to charged leptons and missing energy. However, we once again find that demanding successful reconstruction effectively cuts the background to negligible levels. In addition, we apply the $\eta \leq 2.5$ cuts on the charged leptons and missing momentum.

We perform fits to $A_0 + A_1 \cos\phi + A_2 \cos 2\phi$ as in Section 3.3 and consider the ratio A_2/A_0, using 1 ab^{-1} of integrated luminosity (due to the smaller cross sections). The results for the SPS3 spectrum are displayed in Fig. 3.9, and those of the MUED spectrum are shown in Fig. 3.10. Note that the true solutions for the vector bosons consist of an approximately 1% signal in the SPS3 spectrum and $\sim 0.5\%$ in MUED. In both spectra the true solution for spinors is consistent with zero. As with the production of μ_{1R}, however, the presence of the false distribution introduces significant spurious values of A_2/A_0, dwarfing the true signal by a factor of ~ 5.

In the SPS3 spectrum, even with 1 ab^{-1} the error bars on the true solution for the vector bosons barely exclude zero at 95% confidence. For the MUED case, the situation is much

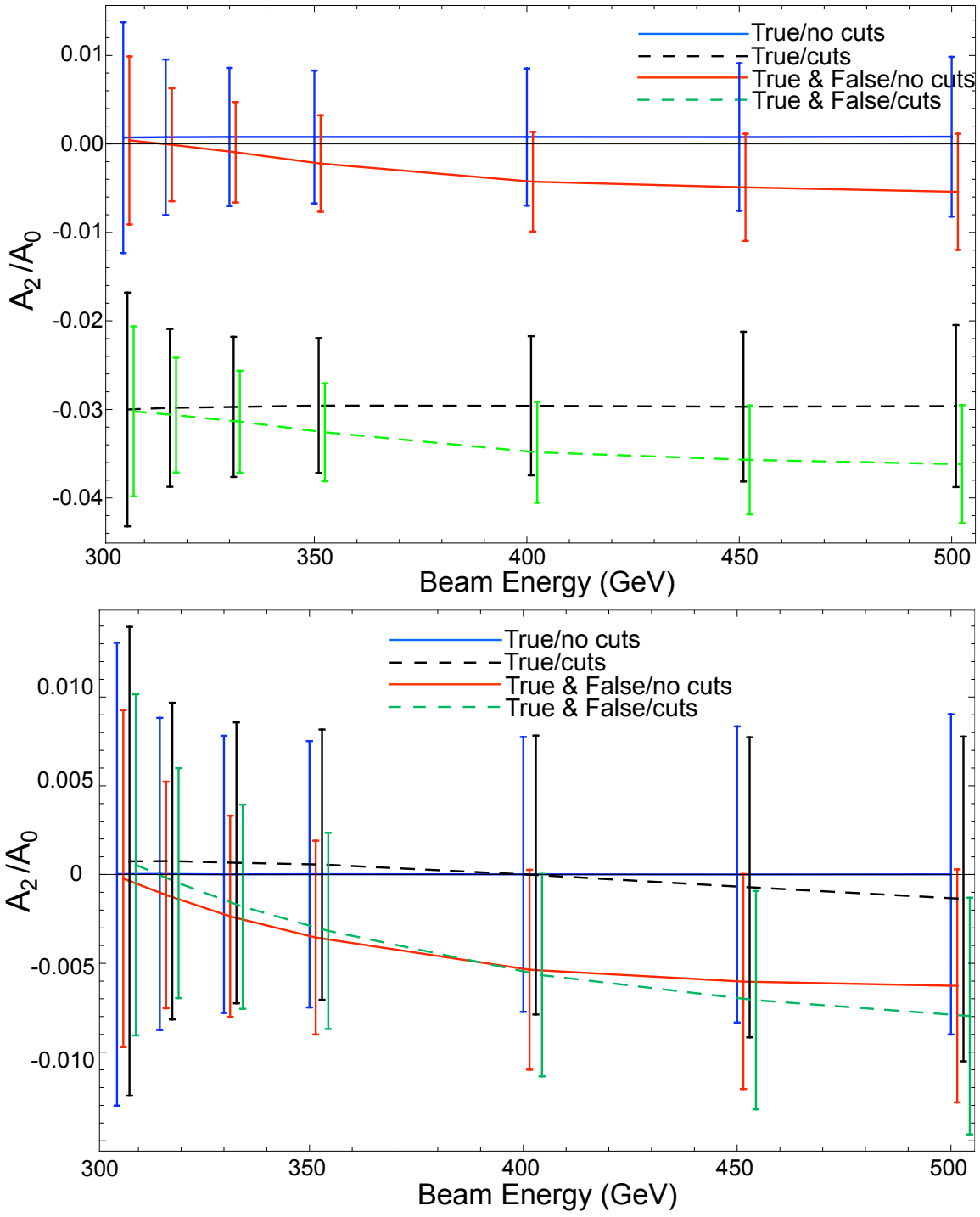

Figure 3.6: Top: Ratio A_2/A_0 for mSUGRA parameter point SPS3 as a function of energy for spinor (UED) pair production with 500 fb^{-1} luminosity. Error bars correspond to 95% exclusion region. Blue lines correspond to true solution only with no rapidity cuts, black dashed lines are true solutions with rapidity cuts, red lines to true and false solutions without cuts, and green are true and false solutions with cuts. Bottom: Ratio A_2/A_0 for SPS3 parameters for spinor (UED) production after correcting for effects of false distribution and cuts on a flat distribution. Color labeling identical to the above.

worse, as a smaller signal is combined with cross sections suppressed by nearly an order of magnitude compared to those in the SPS3 case. Thus, statistics may be a limiting factor in measuring non-zero spins.

We attempt to correct for the effects of cuts and false solutions by generating events which decay according to phase space. As the production angle may be measured up to the two-fold reconstruction ambiguity, we generate the particles with the correct θ distributions and flat θ_i, ϕ_i distributions and run the resulting events through the reconstruction and detector simulator. The resulting values for A_2/A_0 are subtracted from those in Figs. 3.9 and 3.10 in an attempt to isolate the spin effects arising from quantum interference from the non-zero A_2/A_0 coming from cuts and the false solutions. The adjusted results are shown in Fig. 3.11 for the SPS3 spectrum. Due to the small signal and poor statistics in the MUED spectrum, even the uncorrected signal in the true solution cannot be distinguished from zero, so we do not adjust for cuts or the false solutions.

Examining Fig. 3.11, we find that the flat distribution captures the effects of cuts on the ratio A_2/A_0 but does not correctly account for the false distributions. We do find that the false distributions do not contribute significantly to the ratio near threshold, as in the measurements of A_1/A_0. Once again, this behavior is not well understood and statistics in this regime are limited. It is conceivable that better results would be obtained by coupling a flat decay in ϕ_i with the *measured* distribution of θ_i to attempt to account for the false distribution. This matching has not been performed as yet.

Thus, while the quantum interference measurement for spin-0 stands on solid ground, the situation for higher spins is less certain. Even neglecting the issue of false solutions, the vector boson ratio A_2/A_0 is on the order of 1%, and so requires significant statistics in order to distinguish from spinor decays. Furthermore, the false distribution introduces a spurious A_2/A_0 value which has not been fully understood by the authors and can dwarf the signal. Finally, the case of of the MUED spectrum demonstrates that, while the method of spin measurement is model independent, it is vulnerable to model-dependent effects such as total cross section, which control the statistical error of the fit. However, note that we could do much better statistically by adding hadronic final states for one of the $\tilde{\chi}_1^{\pm}/W_1$ while requiring leptonic final states for the other. We again would have two-fold ambiguity, but the rest of the measurement remains the same as long as we can measure the hadronic energies well enough. This may be possible by using the energy-flow method that matches tracking and calorimeter information.

3.5 Conclusion

We have demonstrated that the quantum interference of multiple helicity states can provide a model-independent method of spin measurements at the ILC. Specifically, with reasonable luminosities, scalar particles can be easily distinguished from spin-1/2 or higher possibilities in pair production followed by decays to visible leptons and missing energy. Determining whether a particle is spin-1/2 or spin-1 suffers from two major problems. The

first is simply statistics: as the signal is on the order of 1%, the requisite luminosity will be a stretch for the ILC, at least in the SUSY and UED models considered.

The second issue concerns the false solution to the reconstruction of the pair produced particles' 4-momentum, and hence the derived values of the azimuthal angles ϕ_1 and ϕ_2. With 8 missing momentum components from the two weakly interacting particles escaping the detector, 4 measured total missing momenta, and 4 mass constraints, the system can be solved only up to a two-fold ambiguity. While the $\cos\phi$ distribution is flat in the false solution, non-trivial dependences on $\cos 2\phi$ develop. From explicit calculations, these dependences appear to be different for flat, spinor, and vector boson distributions, and so cannot be subtracted from the combined solutions without losing the desired model-independence.

It therefore behooves us to consider methods for full reconstruction of the event. If the decay proceeds by emitting several visible particles in a cascade of particles with known mass down to the LSP/LKP, then we may overconstrain the decay, allowing for full reconstruction. In particular, if the pair produced particles decay to the LSP through an intermediate state, then there would be 6 mass constraints on the system. With only 8 unknown quantities and 4 measured values, the false solution is no longer present. Unfortunately, all such decays considered by the authors so far have too low a cross section to provide useful spin measurements.

However, such lengthy decay chains raise the possibility of applying this method to the LHC. At a hadron collider the center of mass energy and frame of reference are unknown for a particular parton-parton level event. Thus, only 2 measured quantities may be obtained in the event: the components of the missing transverse momentum $\not{p}_T$. With a multi-step decay we obtain 6 mass constraints, and combining these with the measured $\not{p}_T$, we can solve the system of 8 missing momentum components up to the two-fold ambiguity. Additionally, the reconstruction algorithm can be used in a modified form [69] to measure the masses in the decay chain as a necessary preliminary step to determining the azimuthal angles. As the cross section for producing TeV-scale particles with color charge at the LHC is very large (e.g. ~ 1 pb for $\tilde{g}$ or $\tilde{q}$ pair production [82]), it seems likely that we may obtain enough statistics in such a case to at least measure the spin of scalar particles if not those of spin 1 or 1/2. This may possibly allow discrimination between the gluino and the KK gluon.

Note that the method proposed can be used and tested already in the Tevatron Z+jet and LEP-II W pair samples. We turn to this possibility in Chapter 4.

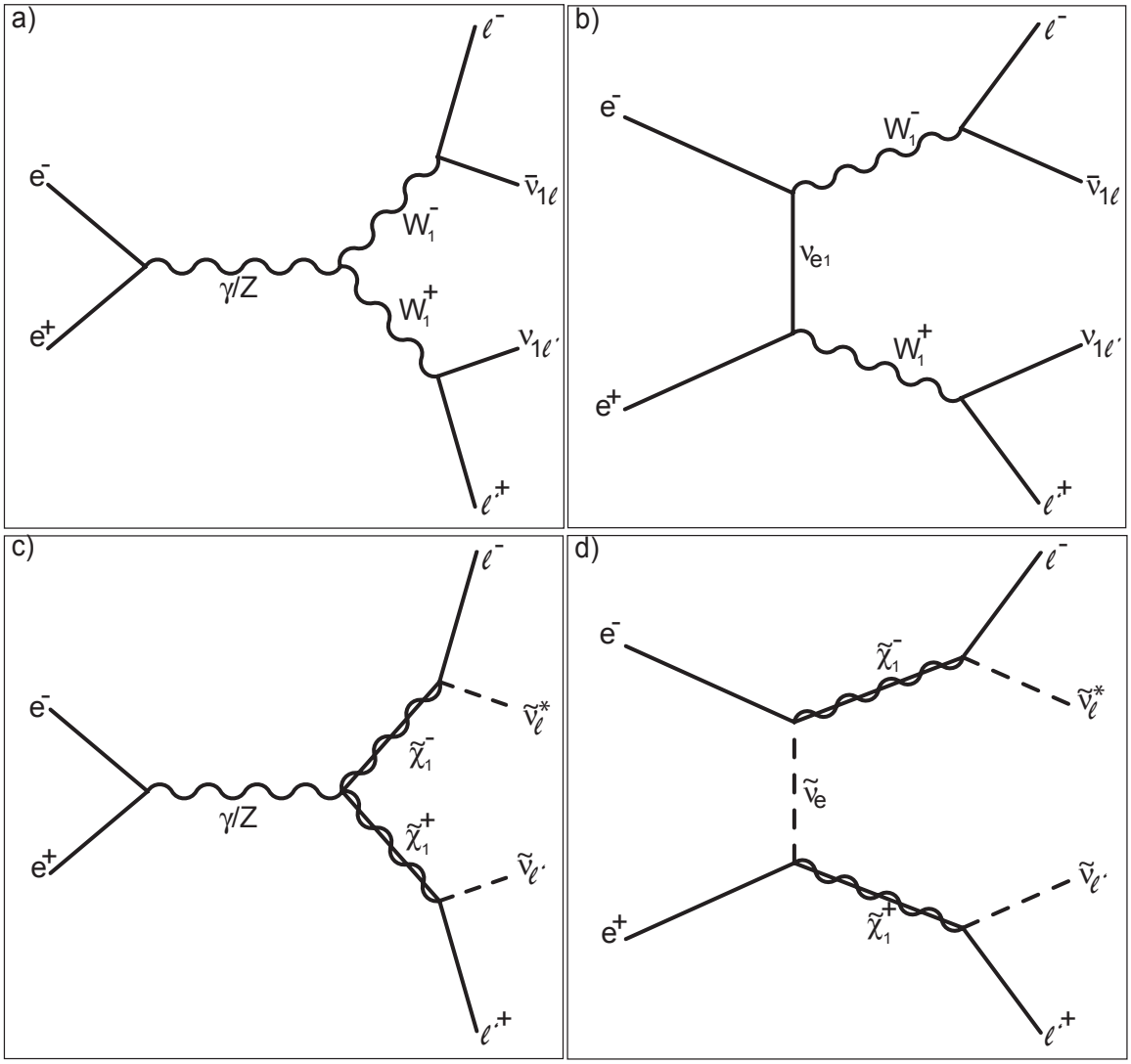

Figure 3.7: a) s-channel and b) t-channel pair production of $\mathrm{KK} = 1$ W bosons in universal extra dimensions decaying to opposite-sign leptons and missing energy in the form of two ν_1s. c) s-channel and d) t-channel pair production of charginos $\tilde{\chi}_1^{\pm}$ in supersymmetry decaying to opposite-sign leptons and sneutrino missing energy

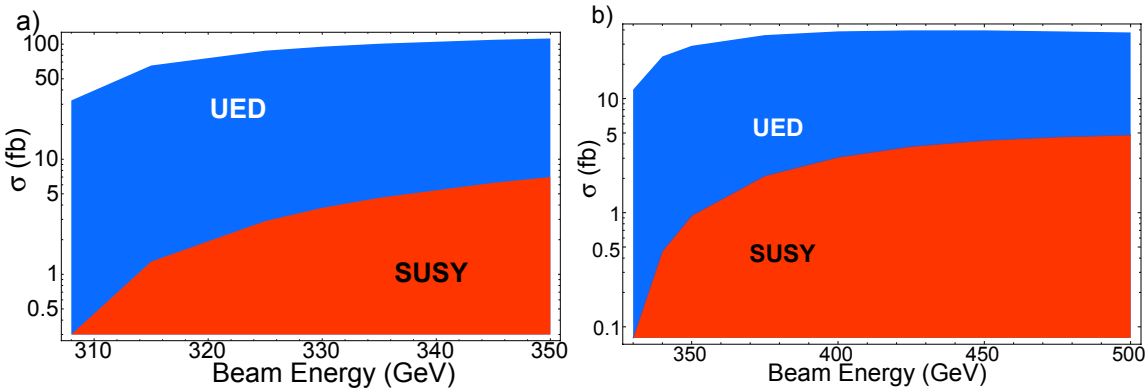

Figure 3.8: Cross sections times branching ratios as a function of beam energy for the UED process $e_L^- e_L^+ \to W_1^- W_1^+ \to \ell^- \ell'^+ \bar{\nu}_{1\ell} \nu_{1\ell'}$ and the SUSY process $e_L^- e_L^+ \to \tilde{\chi}_1^- \tilde{\chi}_1^+ \to \ell^- \ell'^+ \tilde{\nu}_{\ell'}^* \tilde{\nu}_{\ell'}$. Figure a) uses the SPS 3 spectrum, while b) uses the MUED spectrum (see Table 3.1).

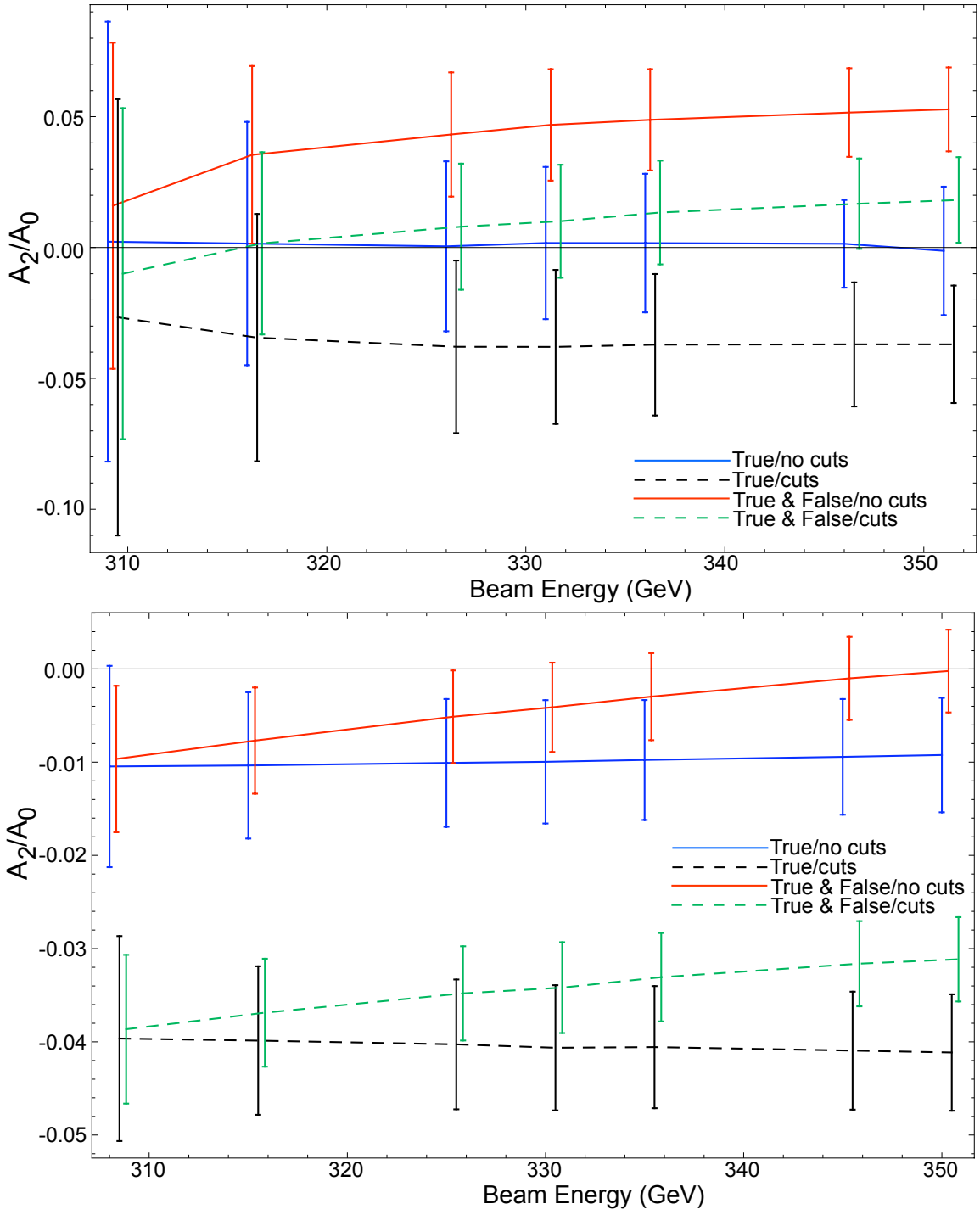

Figure 3.9: Top: Ratio A_2/A_0 versus beam energy for the supersymmetric spinor production $e_L^- e_L^+ \to \tilde{\chi}_1^- \tilde{\chi}_1^+ \to \ell^- \ell'^+ \tilde{\nu}_\ell^* \tilde{\nu}_{\ell'}$ for the SPS3 spectrum. Bottom: Ratio A_2/A_0 for the UED vector boson production $e_L^- e_L^+ \to W_1^- W_1^+ \to \ell^- \ell'^+ \bar{\nu}_{1\ell} \nu_{1\ell'}$ for the same spectrum. Color coding as in Fig. 3.5. Error bars correspond to 95% exclusion region assuming 1 ab^{-1} luminosity.

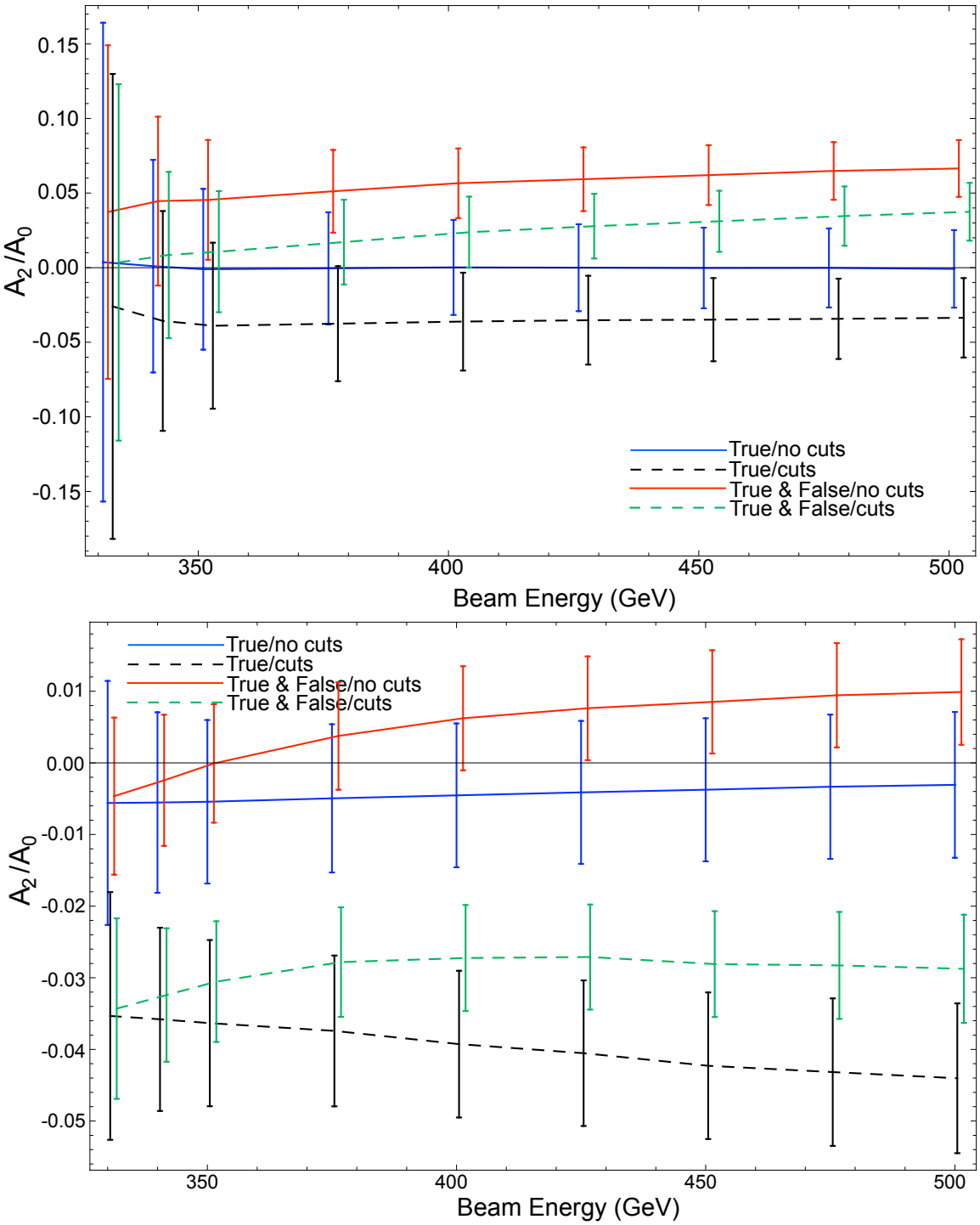

Figure 3.10: Top: Ratio A_2/A_0 versus beam energy for the supersymmetric spinor production $e_L^- e_L^+ \to \tilde{\chi}_1^- \tilde{\chi}_1^+ \to \ell^- \ell'^+ \tilde{\nu}_{\ell'}^* \tilde{\nu}_{\ell'}$ for the MUED spectrum (see Table 3.1). Bottom: Ratio A_2/A_0 for the UED vector boson production $e_L^- e_L^+ \to W_1^- W_1^+ \to \ell^- \ell'^+ \bar{\nu}_{1\ell} \nu_{1\ell'}$ for the same spectrum. Color coding as in Fig. 3.5. Error bars correspond to 95% exclusion region assuming 1 ab^{-1} luminosity.

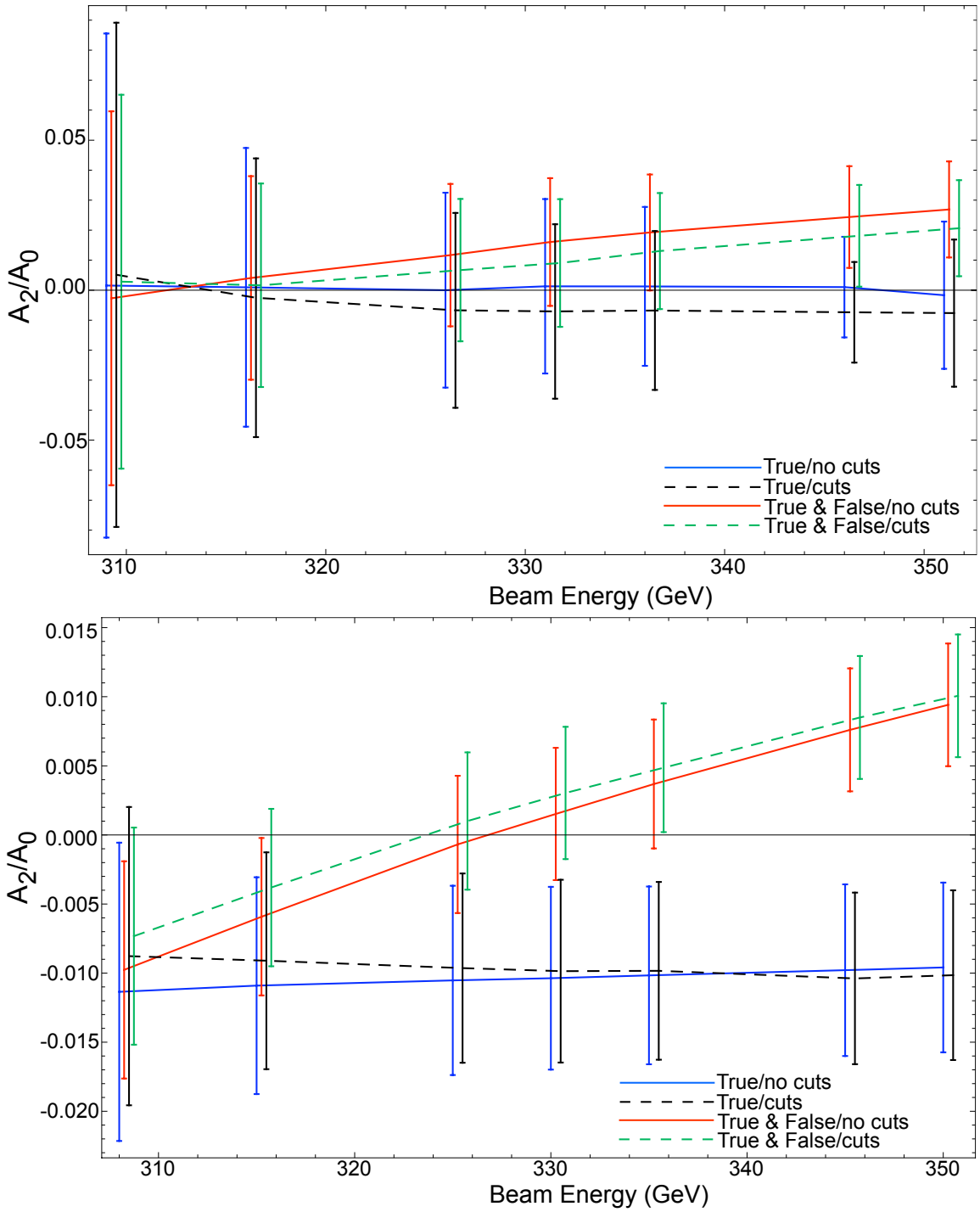

Figure 3.11: Top: Ratio A_2/A_0 versus beam energy for the supersymmetric spinor production $e_L^- e_L^+ \to \tilde{\chi}_1^- \tilde{\chi}_1^+ \to \ell^- \ell'^+ \tilde{\bar{\nu}}_{\ell'} \tilde{\nu}_{\ell'}$ for the SPS3 spectrum adjusted to account to detector and cut effects. Bottom: Ratio-adjusted values of A_2/A_0 for the UED vector boson production $e_L^- e_L^+ \to W_1^- W_1^+ \to \ell^- \ell'^+ \bar{\nu}_{1\ell} \nu_{1\ell'}$ for the same spectrum. Color coding as in Fig. 3.5. Error bars correspond to 95% exclusion region assuming 1 ab^{-1} luminosity.

Chapter 4

Quantum Interference Effects Among Helicities at LEP-II and Tevatron

A completely model-independent method of obtaining information on the spin using the quantum interference effect among various helicity states was proposed in Chapter 3. In this chapter, we point out that this effect should be demonstrable in the existing data on $e^-e^+ \to W^+W^-$ at LEP-II and $p\bar{p} \to Z^0 + j$ at the Tevatron.

4.1 Introduction

There are many reasons to expect that new particle degrees of freedom will be discovered at the TeV energy scale (Terascale), beginning with the recent start of the Large Hadron Collider (LHC). The fact that the Terascale must have interesting physics has been known since Fermi's 1933 theory of nuclear beta decay which introduced a dimensionful constant $G_F \approx (0.3 \text{ TeV})^{-1}$. In its more modern incarnation, this constant represents the size of the Bose–Einstein condensate that makes the universe a gigantic superconductor. The analog of the Meissner effect then makes the range of the weak force as short as a billionth of a nanometer.

At the least we expect the gap excitation of the superconductor, the Higgs boson, to be discovered at the LHC. In addition, the quantum instability of this energy scale suggests new particles below a TeV in order to protect it from diverging to infinity. Many theoretical frameworks have been proposed in the literature: new strongly coupled gauge theory (technicolor [43, 44]), fermionic dimensions of spacetime (supersymmetry [46]), bosonic dimensions of spacetime (extra dimensions [47, 30]), new hidden extra symmetries (little Higgs [53]), Higgsless theories [83, 84] etc. Many of these also provide candidates for the mysterious dark matter of the universe. With great anticipation the community awaits the imminent discovery of such exotic new particles in the upcoming LHC experiments.

Once new particles are discovered, determining what theoretical framework they belong to is of foremost importance. For this purpose truly basic measurements will be required:

the mass, parity, and spin of the new particles. Among these, the spin measurement is both the key and the most challenging. Numerous studies exist that try to formulate strategies for spin measurements at the LHC [61, 58, 63, 56, 62, 60, 59, 64]. Unfortunately, it is very difficult to avoid model-dependent assumptions in the proposed measurement strategies.

In Chapter 3, we proposed a completely model-independent way of obtaining information about spin at collider experiments.[1] The key element is quantum interference among various helicity states of the new particle, which, to our surprise, has not been discussed in the modern literature (see, however, [85]). We discussed how this method may work to discriminate the smuon in supersymmetry or the Kaluza–Klein muon in extra dimensions at the proposed International Linear Collider (ILC).

In this chapter, we point out that the effectiveness of our proposed method should be demonstrable in the existing data. In particular, $e^-e^+ \to W^+W^-$ at LEP-II and $p\bar{p} \to Z^0 + j$ at the Tevatron should allow highly significant studies of the quantum interference among helicities, and demonstrate the spin-one nature of the W and Z bosons without any model assumptions. As discussed in Chapter 3, this method works particularly well close to the production threshold. This is good news for the LHC, as new physics there will likely be dominated by the energy range just above threshold.

The proposed strategy is extremely simple. In order to obtain model-independent information about spin, or angular momentum in general, we resort to the general principles of quantum mechanics. The angular momentum operators generate spatial rotations; the unitary operator $U(\vec{\phi}) = e^{i\vec{J}\cdot\vec{\phi}/\hbar}$ rotates space around the axis $\vec{\phi}$ by the angle $|\vec{\phi}|$. If we choose the rotation axis to be the momentum vector of a free particle, it isolates the spin component because the orbital angular momentum is always orthogonal to the momentum vector $\vec{L}\cdot\vec{p} = (\vec{x}\times\vec{p})\cdot\vec{p} = 0$. Therefore, the angular momentum along the momentum vector is nothing but its helicity, $h = (\vec{s}\cdot\vec{p})/|\vec{p}|$. The rotation around the momentum axis by an angle ϕ therefore gives the phase $e^{ih\phi}$ to the quantum mechanical amplitudes.

Obviously a single phase factor does not lead to a physical observable since the probability does not depend on phases. However, an interference effect may pick up the *differences* in phases among interfering amplitudes. Fortunately, particles produced in collisions are often in a linear superposition of various helicity states, which interfere when they decay into a common final state. This interference of different helicity states produces a cross section dependent on the coherent sum of individual matrix elements squared:

$$\sigma \propto \left| \sum_h \mathcal{M}_{\text{prod.}}(h)\mathcal{M}_{\text{decay}}(h,\phi) \right|^2 \tag{4.1}$$
$$\mathcal{M}_{\text{decay}}(h,\phi) = e^{ih\phi}\mathcal{M}_{\text{decay}}(h,\phi=0).$$

Here $\mathcal{M}_{\text{prod.}}(h)$ and $\mathcal{M}_{\text{decay}}(h,\phi=0)$ are the production and decay matrix elements, which depend in detail on the helicity state h. However, all ϕ dependence has been factored out into the exponential. It is clear from this sum that the azimuthal angular dependance of

[1] This possibility was originally suggested in [65].

the event distributions $N = \sigma \times \mathcal{L}$ (where $\mathcal{L}$ is the luminosity) is

$$\frac{dN}{d\phi} = \frac{d\sigma}{d\phi} \times \mathcal{L} = A_0 + A_1 \cos\phi + \cdots + A_n \cos(n\phi), \tag{4.2}$$

where $n = \Delta h$ is the difference between the highest and lowest helicity states contributing to the sum in Eq. (4.1). In this way, we obtain an unambiguous lower limit on the spin of the particle, $s \geq (\Delta h)/2$. As we will see, this limit is saturated, $s = \Delta h/2$, in the examples below, and the presence of the highest mode is clearly visible in collider data given sufficient statistics.

4.2 Spin Measurement at LEP-II and Tevatron

In the cases of $e^- e^+ \to W^+ W^-$ with leptons plus jets final states and $p\bar{p} \to Z^0 + j$ with decays to electrons, spin-1 particles are produced in a superposition of helicity states.[2] In both cases, the event is fully reconstructable using the visible momentum in the event, and hence the angle ϕ can be fully determined from data.

The angle ϕ is defined in the lab frame of the event as the angle between the production plane described by the W^+W^- or $Z^0 + j$ and the decay plane containing the leptonic decay products from the vector bosons. If we define the positive z axis in the lab frame of LEP-II (Tevatron) as the direction of the e^- (proton) beam, then the cosine of ϕ at LEP-II can be calculated as follows:

$$\begin{aligned} \hat{n}_{\text{prod.}} \equiv \frac{\hat{z} \times \vec{p}_{W^\pm}}{|\hat{z} \times \vec{p}_{W^\pm}|}, \qquad \hat{n}_{\text{decay}} \equiv \frac{\vec{p}_{W^\pm} \times \vec{p}_{\ell^\pm}}{|\vec{p}_{W^\pm} \times \vec{p}_{\ell^\pm}|} \\ \cos\phi \;=\; \hat{n}_{\text{prod.}} \cdot \hat{n}_{\text{decay}}, \end{aligned} \tag{4.3}$$

where $\vec{p}_{\ell^\pm}$ is the charged lepton from the decay of the $W^\pm$ boson. The definition of ϕ at the Tevatron is the same as in Eq. (4.3) with the substitution of Z^0 for $W^\pm$. An arbitrary (but consistent) choice must be made to define which side of the production plane will contain positive ϕ. For LEP-II, we chose this positive direction to be in the direction of $\hat{z}$ crossed with the momentum of the leptonically decaying $W^\pm$. Similarly, we chose the direction of the proton beam crossed with that of the Z^0 at the Tevatron (see Fig. 4.1). Based on our argument above, we expect to see cross sections for these events as in Eq. (4.2) with $n = 2$.[3]

The LEP-II luminosities from the years 1997-2000 [86] are reported in Table 4.1. The OPAL collaboration has observed 1574 events identified as $q\bar{q}e\nu$ and an additional 1573

[2] It is for this reason we cannot consider $p\bar{p} \to Z$ without jets. In such events, the Z is produced in only one spin state, depending on the spin of the initial-state quarks. While the cross section would contain a sum over Z helicity, the sum would be incoherent.

[3] It should be noted that if the collider beams are identical, this choice of positive ϕ suffers from an ambiguity which maps $\phi \to \phi + \pi$. This may, for example, introduce difficulties in measuring A_n (n odd) parameters at the LHC.

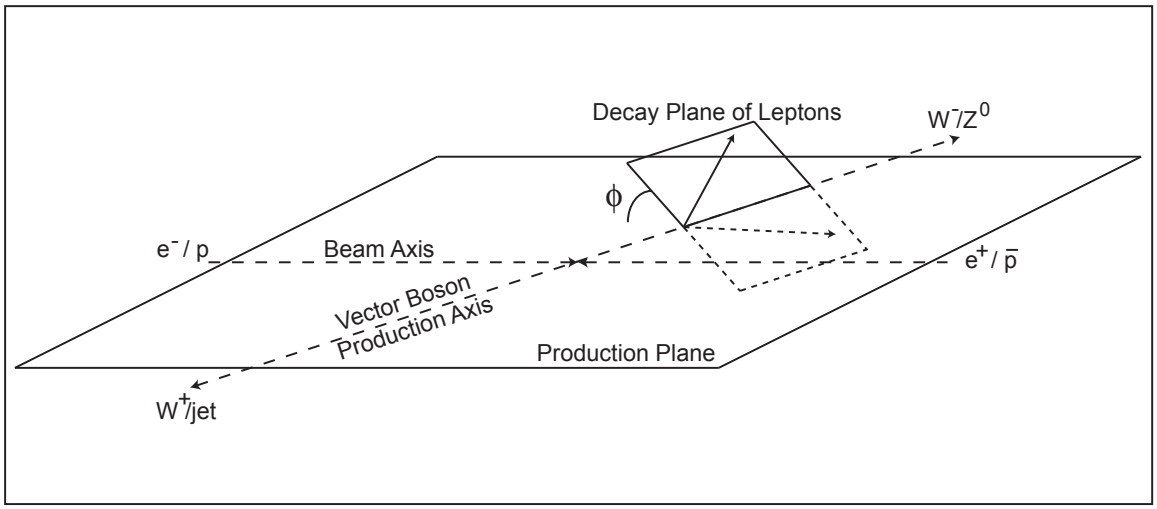

Figure 4.1: The event kinematics of $e^-e^+ \to W^+W^- \to q\bar{q}\ell^\pm\nu$ at LEP-II and $p\bar{p} \to Z^0 + j \to e^-e^+ + j$ at the Tevatron. The plane of pair produced vector bosons and the plane formed by the leptonic decay of one boson are shown. The angle ϕ is the relative azimuthal angle between these two planes, defined in the lab frame of the event, as defined in Eq. (4.3). Positive ϕ are in the direction of the e^- (p) beam momentum crossed with the W^- (Z^0) momentum for LEP-II (Tevatron).

$q\bar{q}\mu\nu$ events [87]. Due to the low purity of the $q\bar{q}\tau\nu$ sample, we ignore those events. Similar data sets are available from the ALEPH [86], DELPHI [88], and L3 [89] collaborations.

The CDF collaboration has data for Z^0+j consisting of 6203 events [90] after selection cuts from 1.7 fb^{-1} of luminosity at 1.96 TeV beam energy. DØ has a similar data set available [91]. A total luminosity of 8 fb^{-1} is expected to be available from the Tevatron at the conclusion of data collection.

Parton level matrix elements for W^+W^- and Z^0+j (where the jet consists of a gluon or first generation (anti) quark at the parton level) production were calculated in HELAS [80], while the numerical integration program BASES [81] was used to determine the differential cross section and integrate over all other kinematic variables. For the simulation of the Tevatron results, a K factor of 1.4 was used to correct for higher order QCD effects, in accordance with [90], and CTEQ5L PDFs were implemented using LHAPDF [92]. The Tevatron results and fits were confirmed using ALPGEN [93].

The generated histograms are assigned Gaussian statistical error bars based on the realistic experimental luminosities. However, no statistical fluctuations are assigned to the central values. As a consequence, the fit results correspond to an average experiment [94].

Before the application of cuts, the differential cross sections for the two processes of interest show a clear $\cos\phi$ and $\cos 2\phi$ dependence, as expected for the decays of spin-1 bosons. These distributions are shown in Fig. 4.2. We then fit the parameters $A_0, A_1, A_2, A_3,$

$\sqrt{s}$ (GeV)	$\mathcal{L}$ (pb^{-1})
182.25	56.8±0.3
188.63	174.2±0.8
191.58	28.9±0.1
195.52	79.9±0.4
199.52	86.3±0.4
201.62	41.9±0.2
204.86	81.4±0.4
206.53	133.2±0.6

Table 4.1: LEP-II integrated luminosity $\mathcal{L}$ as a function of beam energy $\sqrt{s}$ [86].

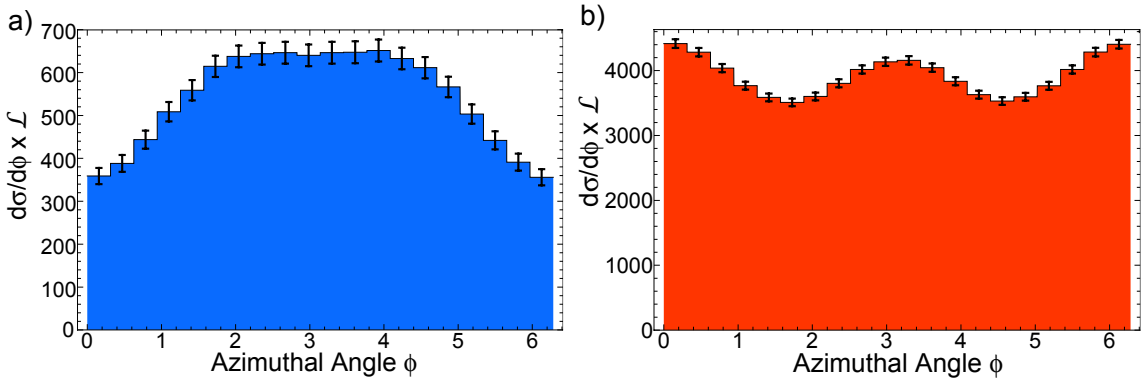

Figure 4.2: Differential distribution of events $d\sigma/d\phi \times \mathcal{L}$ for a) $e^-e^+ \to W^+W^- \to q\bar{q}\ell^\pm\nu$ using the LEP-II run data in Table 4.1 and b) $p\bar{p} \to Z^0 + j \to e^-e^+ + j$ with luminosity $\mathcal{L} = 1.7$ fb^{-1}. No cuts are applied on the LEP-II simulation; Tevatron results have $p_T > 30$ GeV and $|\eta| < 2.1$ on the jet.

and A_4 in Eq. (4.2) to the event distributions.[4] For each of the five parameters A_n, 1σ error bars are calculated after marginalizing over the other four. Results for the LEP-II and Tevatron simulations are shown in Table 4.2; in order to compare simulations with different numbers of events, values of A_n/A_0 are reported rather than A_n. It it clear at this stage that the results are consistent with the decay of spin-1 bosons.

4.3 The Effects of Cuts

However, cuts must be applied to the events recorded at LEP-II and Tevatron, both due to detector geometry and in order to reduce background. These cuts will affect the azimuthal distribution present in $d\sigma/d\phi \times \mathcal{L}$, and so can obscure the signal necessary for

[4]These fits are to the numerically integrated differential cross-section, not generated events.

	LEP-II	Tevatron
A_1/A_0	-0.267 ± 0.023	0.036 ± 0.009
A_2/A_0	-0.085 ± 0.025	0.100 ± 0.009
A_3/A_0	0.000 ± 0.025	0.000 ± 0.009
A_4/A_0	0.000 ± 0.026	0.000 ± 0.010

Table 4.2: Fits to the parameters A_n in Eq. (4.2) for the differential distributions of $e^-e^+ \to W^+W^- \to q\bar{q}\ell^\pm\nu$ (LEP-II) using the integrated luminosity in Table 4.1, and $p\bar{p} \to Z^0 + j \to e^-e^+ + j$ (Tevatron) using $\mathcal{L} = 1.7$ fb^{-1}. Errors for each parameter are obtained by marginalizing over the other four parameters in the fit. No cuts are applied on the LEP-II simulation; Tevatron results have $p_T > 30$ GeV and $|\eta| < 2.1$ on the jet.

Jet transverse momentum	$p_{T,j} > 30$ GeV
Jet η	$\lvert\eta\rvert < 2.1$
Invariant mass of lepton pair	$66 < m_{\ell\ell} < 116$ GeV
Central electron η	$\lvert\eta\rvert < 1$
Second electron η	$\lvert\eta\rvert < 1$ or $1.2 < \lvert\eta\rvert < 2.8$
Electron E_T	$E_T > 25$ GeV
Electron isolation cuts	$\Delta R_{ej} > 0.7$

Table 4.3: Event selection cuts imposed by the CDF collaboration on $p\bar{p} \to Z^0 + j \to e^-e^+ + j$ events. In each event, one electron must be central, and pass stricter cuts than the second electron. The isolation cut parameter is defined as $\sqrt{(\Delta\phi)^2 + (\Delta\eta)^2} \equiv \Delta R$ [90].

spin measurements. The Tevatron cuts (Table 4.3) were taken from the CDF experiment [90], while the OPAL [95] cuts (Table 4.4) were used to simulate the LEP-II data.

Our simulation did not include parton showers or hadronization, so we could not implement the lepton isolation cut used by OPAL, which placed a limit on the total energy deposited in a cone centered on the lepton. Instead, we used a cut on $\Delta R \equiv \sqrt{(\Delta\phi)^2 + (\Delta\eta)^2}$ between the jet and the leptons. Three values for ΔR were used: 0.2, 0.5, and 0.75, which gave total efficiencies for the cuts of 79%, 76%, and 72%, respectively. The cuts used by the OPAL collaboration had an efficiency of 85% for final states with an electron and 89% for muons. The distributions of the Tevatron and LEP-II (with $\Delta R = 0.75$) simulations after cuts are shown in Fig. 4.4.

Fitting the distributions to Eq. (4.2), we find the results in Table 4.5. These results clearly show that the imposed cuts introduce spurious high-frequency modes. The corresponding non-zero A_3 and A_4 components may naively be confused for evidence of spin-2 particles. However, the cuts are responsible for introducing new ϕ dependence by selecting out new directions relative to the production axis of the gauge bosons.

We illustrate this effect for the case of cuts in the forward direction (large $|\eta|$ and $|\cos\theta|$) in Fig. 4.3. Here we see two decays which are kinematically identical in the boson rest

Lepton momentum	$p_\ell > 25$ GeV
Polar angle θ of final state particles	$\lvert\cos\theta\rvert < 0.95$
Neutrino energy fraction	$R_\nu > 0.07$
Visible energy fraction	$R_{\text{vis}} > 0.3$
Neutrino transverse momentum	$p_{T,\nu} > 16$ GeV
Lepton isolation	$\Delta R > 0.75, 0.5, 0.2$

Table 4.4: Event selection cuts imposed by the OPAL collaboration on $e^-e^+ \to W^+W^- \to q\bar{q}\ell^\pm\nu$ events. Energy fraction is defined as $R_\alpha \equiv E_\alpha/\sqrt{s}$, where α is either the neutrino ν or the total visible energy. The lepton isolation cut was implemented using $\sqrt{(\Delta\phi)^2 + (\Delta\eta)^2} \equiv \Delta R$ with a range of ΔR values rather than limiting the total energy deposited in a cone surrounding the lepton as in [95].

frame save for azimuthal rotations. In Fig. 4.3a, the event survives the cuts, as neither lepton lies sufficiently close to the z axis. However, in Fig. 4.3b, rotating the decay plane about the axis of the boson momentum yields an event which is eliminated by the cuts. This is the source of unwanted ϕ dependences in the differential distributions with cuts. Similar problems arise due to isolation cuts, which depend on the proximity of the leptons to the other particles in the final state, as well as cuts on leptonic transverse momentum.

Since this ϕ dependence did not arise from the quantum interference of helicity amplitudes, we cannot expect the ϕ dependence of the cross section to accurately reflect the spin of the decaying particles. Thus non-zero A_3 and A_4 components do not indicate a higher spin state, but rather a breakdown of the proposed spin-measurement technique.

4.4 A Solution: Rotationally Invariant Cuts

The solution to this problem is relatively straightforward. For new azimuthal dependences to be avoided, the cuts cannot pick out "special" directions relative to the original momentum of the decaying boson. Therefore, we impose "rotationally invariant cuts" in which we require that each event not only passes the experimental cuts but continues to do so when the decay plane is rotated around the boson production axis. This avoids the introduction of a new directional dependence since we restrict ourselves to only those events which could never overlap the forbidden regions of the detector regardless of orientation. However, these cuts are very inefficient: the cuts on LEP-II data preserve only 12% of the original events, while the cuts for the Tevatron leave less than 1%.

The CDF cuts are very inefficient due to the small allowed $|\eta|$ region for the central electron (see Table 4.3). Recent preliminary CDF measurements have demonstrated that the cuts can be relaxed while still maintaining a background level of less than 5% [96]. These loosened cuts are identical to those in Table 4.3 for p_T and η of the jet and the invariant mass of $m_{\ell\ell}$. However, the central lepton is allowed $E_T > 20$ GeV and $|\eta| < 2.6$, while the second electron must have $E_T > 10$ GeV and $|\eta| < 2.6$. If both leptons have

	LEP-II		
	$\Delta R = 0.75$	$\Delta R = 0.5$	$\Delta R = 0.2$
A_1/A_0	-0.082 ± 0.025	-0.082 ± 0.026	-0.082 ± 0.025
A_2/A_0	-0.293 ± 0.026	-0.302 ± 0.027	-0.308 ± 0.026
A_3/A_0	0.110 ± 0.027	0.114 ± 0.028	0.117 ± 0.028
A_4/A_0	-0.099 ± 0.028	-0.099 ± 0.029	-0.096 ± 0.029

	Tevatron
A_1/A_0	0.029 ± 0.012
A_2/A_0	-0.277 ± 0.012
A_3/A_0	-0.021 ± 0.013
A_4/A_0	-0.123 ± 0.014

Table 4.5: Fits of the differential distribution of $e^- e^+ \to W^+ W^- \to q\bar{q}\ell^\pm\nu$ (LEP-II) with the cuts in Table 4.4 and $p\bar{p} \to Z^0 + j \to \ell^-\ell^+ + j$ (Tevatron) with the cuts in Table 4.3 to parameters A_n in Eq. (4.2). Luminosities are as in Table 4.2. 1σ errors for each parameter are obtained by marginalizing over the other four parameters in the fit.

$2.6 > |\eta| > 1.0$, E_T must be greater than 25 GeV. Finally, ΔR_{ej} must be greater than 0.4. With these relaxed numbers, the total number of events in the simulated sample is 5821 and the efficiency of the rotationally invariant cuts is 18%.

The result of these rotationally invariant cuts on the LEP-II and Tevatron data are shown in Fig. 4.5 (compare to Fig. 4.2). Table 4.6 confirms that this technique restores the ϕ dependence expected by the interference argument.

In the case of the Tevatron results with loosened cuts, the data are clearly consistent with the Z being a spin-1 vector boson. The A_1 parameter is non-zero at 1.8σ, the A_2 parameter is non-zero at nearly 4σ, and the higher modes are consistent with zero. It is important to recall that a lower bound on the spin is obtained from the *highest* non-zero mode, therefore the 4σ signal in A_2 is far more important then the 1.8σ deviation from zero in A_1.

From these results there is always the possibility that the parent Z is a higher spin particle and that some conspiracy amongst the matrix elements in Eq. (4.1) prevents the A_3 and A_4 terms from appearing in the sum. In this interpretation, we can still state unambiguously that the Z is *at least* spin-1, and that the data suggest it is not of higher spin.

Higher statistics would allow a reduction of error bars and increase our confidence in the result correspondingly. Using, for example, the estimated total integrated luminosity of 8 fb^{-1} for the Tevatron, the parameters have the values shown in Table 4.7. Another possibility is to use the muon decays of the Z^0. However, the rotationally invariant cuts will likely take a high toll on such events, as the muon tracking system at CDF extends only up to $|\eta| = 1.5$ [97].

The situation with the LEP-II simulation is more complicated. While the A_1 parameters are non-zero at over 3σ, the A_2 parameters differ from zero by only one standard deviation.

	LEP-II		
	$\Delta R = 0.75$	$\Delta R = 0.5$	$\Delta R = 0.2$
A_1/A_0	-0.215 ± 0.069	-0.214 ± 0.060	-0.207 ± 0.053
A_2/A_0	-0.068 ± 0.071	-0.071 ± 0.062	-0.072 ± 0.055
A_3/A_0	0.000 ± 0.073	0.000 ± 0.064	0.000 ± 0.057
A_4/A_0	0.000 ± 0.075	0.000 ± 0.065	0.000 ± 0.058

	Tevatron
A_1/A_0	0.039 ± 0.022
A_2/A_0	0.083 ± 0.021
A_3/A_0	0.000 ± 0.022
A_4/A_0	0.000 ± 0.023

Table 4.6: Fits of the differential distribution of $e^-e^+ \to W^+W^- \to q\bar{q}\ell^\pm\nu$ (LEP-II) and $p\bar{p} \to Z^0 + j \to \ell^-\ell^+ + j$ (Tevatron) to the parameters A_n in Eq. (4.2), requiring events that pass the cuts in Tables 4.4 and 4.3 (with relaxed E_T, $|\eta|$, and ΔR cuts as described in the text) after rotation about the momentum axis of the decaying vector boson. The luminosities are the same as in Tables 4.2 and 4.5. 1σ errors for each parameter are obtained by marginalizing over the other four parameters in the fit.

A larger data set would of course solve this problem. As all four LEP-II experiments (ALEPH, DELPHI, L3, and OPAL) have approximately equal statistics available, a two-fold increase in the statistical significance could be achieved by combining the events from these collaborations; the resulting ratios A_n/A_0 are shown in Table 4.7.

Another possibility is that some reduction in required cuts would increase the efficiency of the rotationally invariant cuts without greatly degrading the sample purity. A likely candidate for this in our analysis is the ΔR cut, which was introduced as a stop-gap measure to approximate the jet-lepton proximity cut used in the OPAL analysis. However, even with the value of $\Delta R = 0.2$, the efficiency of the cut is lower than the 85% reported by OPAL. Setting $\Delta R = 0$ is clearly an unrealistic cut, but as demonstrated in Table 4.7 indicates the possibilities offered by higher statistics.

4.5 Conclusion

In conclusion, we have demonstrated that the quantum interference among the matrix elements of different helicity states provides a model-independent probe of particle spin. Using realistic data sets, rotationally invariant cuts can be implemented which correct for the spurious high-frequency noise introduced by the cuts imposed by detector geometry and background reduction. Though these techniques come at a price in terms of efficiency, it seems possible to relax the cuts in such a way that the weak gauge boson spins can be measured at sufficient significance at current colliders.

Measurements of the spin of new particles is expected to be a critical discriminator of new physics at the LHC. As a result, techniques such as the one proposed here are very important. Though the spins of the W and Z bosons are not in doubt, we find it encouraging that this new method can be tested on the available data. Such work would be of great use as we embark upon the LHC era.

	LEP-II		Tevatron
	Combined	$\Delta R = 0$	$\mathcal{L} = 8$ fb^{-1}
A_1/A_0	-0.207 ± 0.027	-0.211 ± 0.050	0.039 ± 0.010
A_2/A_0	-0.072 ± 0.028	-0.081 ± 0.052	0.083 ± 0.010
A_3/A_0	0.000 ± 0.028	0.000 ± 0.053	0.000 ± 0.010
A_4/A_0	0.000 ± 0.029	0.000 ± 0.054	0.000 ± 0.010

Table 4.7: Fits of the differential distribution to the parameters A_n in Eq. (4.2) for $e^-e^+ \to W^+W^- \to q\bar{q}\ell^\pm\nu$ with the jet-lepton cut parameter $\Delta R = 0.2$ and combining the data sets of ALEPH, DELPHI, L3, and OPAL (LEP-II, Combined), $e^-e^+ \to W^+W^- \to q\bar{q}\ell^\pm\nu$ with the OPAL data set and ΔR set to zero (LEP-II, $\Delta R = 0$), and $p\bar{p} \to Z^0 + j \to \ell^-\ell^+ + j$ with 8 fb^{-1} integrated luminosity (Tevatron). We require that all events pass the cuts in Tables 4.4 (with ΔR as indicated) and 4.3 (with relaxed E_T and $|\eta|$ cuts as described in the text) after rotation about the momentum axis of the decaying vector boson. 1σ errors for each parameter are obtained by marginalizing over the other four parameters in the fit.

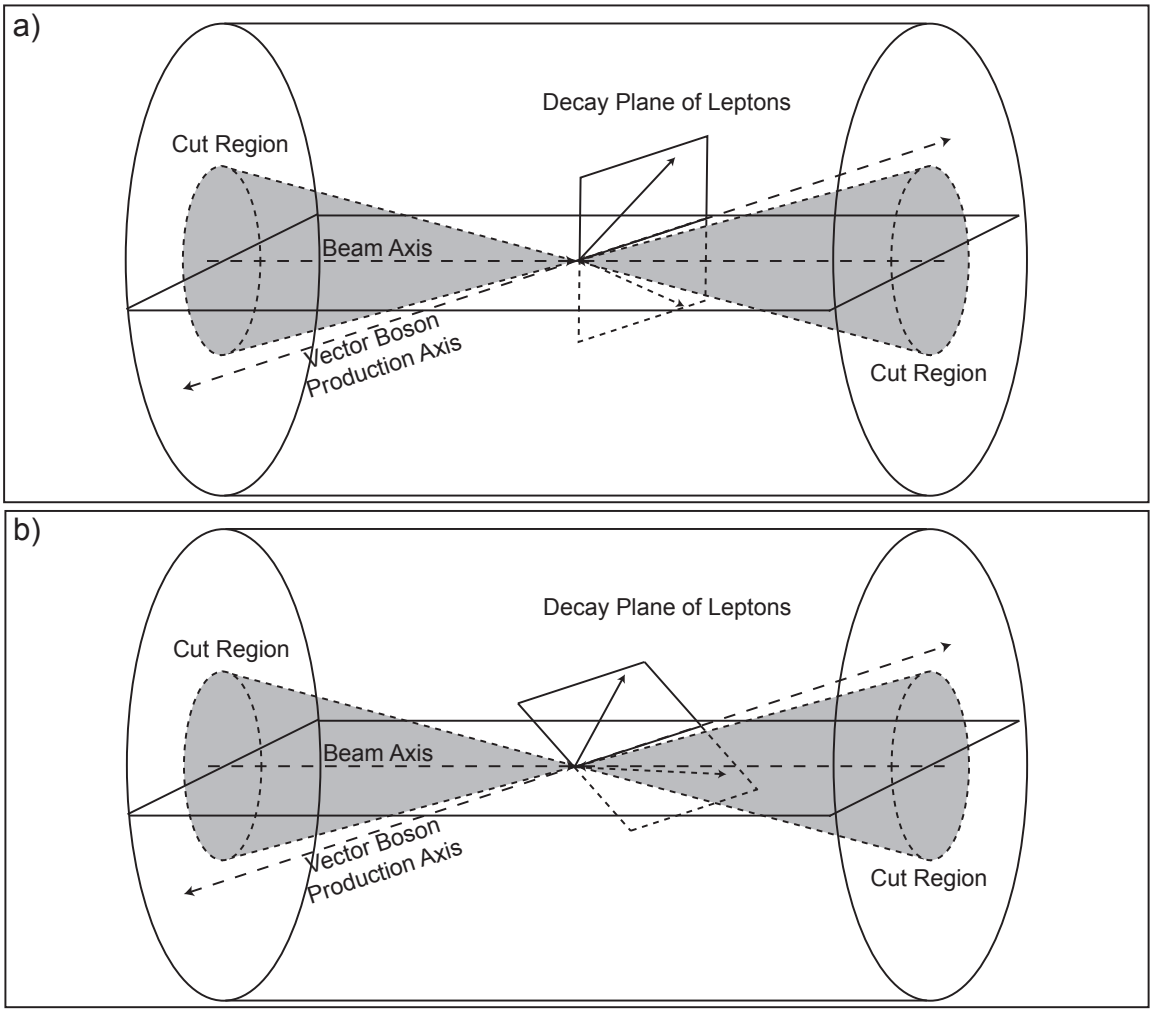

Figure 4.3: A depiction of the detector volume demonstrating the rotational dependence induced by the cuts. The shaded forward regions (large values of $|\eta|$ and $|\cos\theta|$) are inaccessible due to detector geometry and background cuts. Two sample events are depicted in a) and b). These events are kinematically identical in the boson rest frame save for a rotation in ϕ. Event a) survives the cuts, while event b) fails.

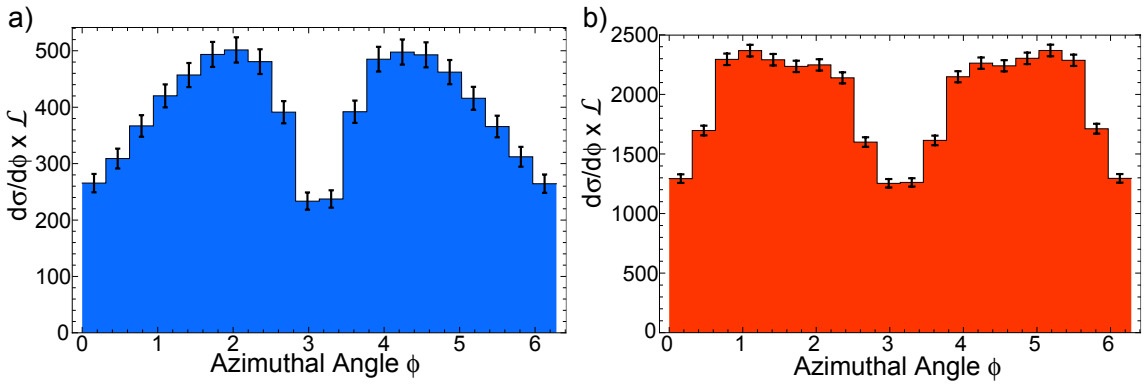

Figure 4.4: Differential distributions for a) $e^-e^+ \to W^+W^- \to q\bar{q}\ell^\pm\nu$ with the cuts in Table 4.4 and $\Delta R = 0.75$ and b) $p\bar{p} \to Z^0 + j \to e^-e^+ + j$ with the cuts from Table 4.3. Luminosities are as in Fig. 4.2.

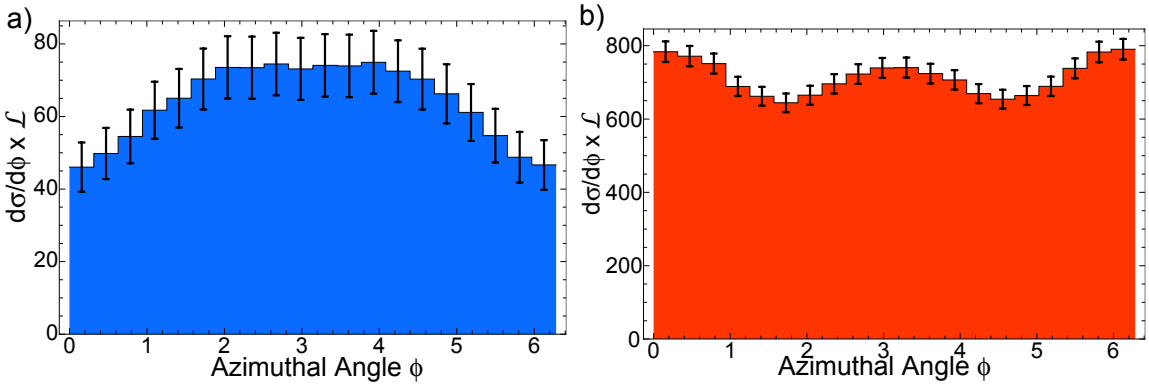

Figure 4.5: Differential distributions for a) $e^-e^+ \to W^+W^- \to q\bar{q}\ell^\pm\nu$ and b) $p\bar{p} \to Z^0 + j \to e^-e^+ + j$ requiring rotationally invariant cuts. Luminosities are as in Fig. 4.2.

Chapter 5

Color Sextet Scalars at the CERN Large Hadron Collider

We now turn from model-independent techniques for measuring the properties of new particles to dedicated searches. In this chapter, taking a phenomenological approach, we study a color sextet scalar at the LHC. We focus on the QCD production of a color sextet pair $\Phi_6\bar{\Phi}_6$ through gg fusion and $q\bar{q}$ annihilation. Its unique coupling to $\bar{\psi}^c\psi$ allows the color sextet scalar to decay into same-sign diquark states, such as $\Phi_6 \to tt/tt^*$. We propose a new reconstruction in the multijet plus same-sign dilepton with missing transverse energy samples ($bb + \ell^\pm\ell^\pm + \not{E}_T + Nj$, $N \geq 6$) to search for on-shell $tt\bar{t}\bar{t}$ final states from sextet scalar pair production. Thanks to the large QCD production, the search covers the sextet mass range up to 1 TeV for 100 fb^{-1} integrated luminosity.

5.1 Introduction

The Large Hadron Collider (LHC) at CERN now provides a great opportunity for exploring physics at the TeV scale. As a proton-proton collider with a target center-of-mass energy of 14 TeV, the LHC is truly a Quantum Chromodynamics (QCD) machine. We therefore wish to study color exotics, since any accessible new physics in the strong interaction sector will appear in the early stages of LHC operation. Many models of physics beyond the standard model (SM) naturally require the presence of color exotics, such as gluinos and squarks in supersymmetric extensions of Standard Model (SM), KK-gluons and KK-quarks in extra dimensional models, or the top-prime in Little Higgs or twin Higgs models. All of these are either quark or gluon partners which belong to the fundamental and adjoint representations of the QCD gauge group $SU(3)_C$, respectively. It is natural to consider colored particles in other representations; in this paper, we focus on a scalar which is in the sextet(6) representation of $SU(3)_C$. Color sextet particles have been widely discussed in nuclear physics as diquark condensate states; in the SSC era, sextet quarks were discussed in [98].

Color sextet scalars are naturally present in partial unification [99], grand unification [100] and composite models; in some cases they may be present around the weak scale. For instance, in a supersymmetric Pati-Salam $SU(2)_R \times SU(2)_L \times SU(4)_C$ model, light color sextet scalars can be realized around the weak scale, even though the scale of $SU(2)_R \times SU(4)_C$ symmetry breaking is around 10^{10} GeV due to existence of accidental symmetries with the masses of color sextet Higgs arising only through high-dimension operators [101, 102]. In this case, the introduction of a color sextet Higgs will not lead to proton decay but only to neutron-anti-neutron ($n - \bar{n}$) oscillation and is fully compatible with present limits [101, 102]. In a similar framework, light color sextet scalars also help in Post-Sphaleron baryogenesis [103]. In this paper, however, we will take a purely phenomenological approach toward the sextet scalar without assuming any model a priori.

Among all the color exotics, the color sextet scalar is unique in its coupling to quarks. In group theory language, the color sextet lies in $3 \otimes 3 = 6 \oplus \bar{3}$ as a symmetric $2^{\rm nd}$ rank tensor under $SU(3)_C$. The Lorentz structure for this scalar coupling to quarks is given by $\psi^T C^{-1} \psi \phi$, where ψ is a Dirac spinor and ϕ is the scalar. Under the SM gauge group $SU(3)_C \times SU(2)_L \times U(1)_Y$, the sextet scalar can be Δ_6, a $SU(2)_L$ adjoint $(6, 3, 1/3)$; Φ_6, a $SU(2)_L$ singlet $(6, 1, 4/3)$; ϕ_6, a $SU(2)_L$ singlet $(6, 1, -2/3)$; or δ_6, a $SU(2)_L$ singlet $(6, 1, +1/3)$. The color sextet scalars are also charged under the global baryon symmetry $U(1)_B$ and the electromagnetic symmetry $U(1)_{\rm EM}$. To avoid breaking $U(1)_{\rm EM}$, these scalar fields should not develop a non-zero vacuum expectation value. This condition removes any possibility of $n - \bar{n}$ oscillation in the minimal model involving color sextet scalars. We may write down the flavor independent Lagrangian of such a minimal model by only considering SM gauge invariants and keeping $U(1)_{\rm EM}$ unbroken,

$$
\begin{aligned}
\mathcal{L} &= \mathrm{Tr}[(D_\mu \Delta_6)^\dagger (D^\mu \Delta_6)] - M_\Delta^2 \mathrm{Tr}[\Delta_6^\dagger \Delta_6] + f_\Delta Q_L^T C^{-1} \tau_2 \Delta_6^\dagger Q_L \\
&+ (D_\mu \Phi_6)^\dagger (D^\mu \Phi_6) - M_\Phi^2 \Phi_6^\dagger \Phi_6 + f_\Phi u_R^T C^{-1} u_R \Phi_6^\dagger \\
&+ (D_\mu \phi_6)^\dagger (D^\mu \phi_6) - M_\phi^2 {\phi_6}^\dagger \phi_6 + f_\phi d_R^T C^{-1} d_R \phi_6^\dagger \\
&+ (D_\mu \delta_6)^\dagger (D^\mu \delta_6) - M_{\delta_6}^2 {\delta_6}^\dagger \delta_6 + f_\delta d_R^T C^{-1} u_R \delta_6^\dagger \\
&- \lambda_\Delta (\mathrm{Tr}[\Delta_6^\dagger \Delta_6])^2 - \lambda_\Phi (\Phi_6^\dagger \Phi_6)^2 - \lambda_\phi ({\phi_6}^\dagger \phi_6)^2 - \lambda_\delta ({\delta_6}^\dagger \delta_6)^2 \\
&- \lambda'_\Delta \mathrm{Tr}[\Delta_6^\dagger \Delta_6 \Delta_6^\dagger \Delta_6] - \mathrm{Tr}[\Delta_6^\dagger \Delta_6](\lambda_1 {\Phi_6}^\dagger \Phi_6 + \lambda_2 {\phi_6}^\dagger \phi_6 + \lambda_3 {\delta_6}^\dagger \delta_6) \\
&- \lambda_4 {\Phi_6}^\dagger \Phi_6 {\phi_6}^\dagger \phi_6 - \lambda_5 {\Phi_6}^\dagger \Phi_6 {\delta_6}^\dagger \delta_6 - \lambda_6 {\phi_6}^\dagger \phi_6 {\delta_6}^\dagger \delta_6 \,, \qquad (5.1)
\end{aligned}
$$

where the QCD covariant derivative is defined as $D_\mu = \partial_\mu - i g_s G_\mu^a T_r^a$, and the T_r^a are the representation matrices for the sextet; M_i^2, λ_i and f_i are all positive-definite model parameters.

If we consider the $SU(2)_L$ adjoint sextet scalar Δ_6 , there will be three physical sextet scalar states that couple to up-type quark pairs, down-type quark pairs, and up-down-type quark pairs. When the sextet scalar decays into light quark states, the existing search strategies for massive octet scalars or vectors [104] may be employed. Δ_6, Φ_6, and δ_6 may all contribute to the single top plus jet signal and $t\bar{t} + Nj$ signal from pair production. Here we consider the scenario in which a color sextet scalar decays into a top quark pair so that

one can use the leptons from the top quark decay to determine the features of the sextet. The signature that contains multi-top final states has been discussed in the context of many new physics models as resonance decaying into top quarks or top composite [102, 105]. To illustrate this and simplify our search, our study will focus on the color sextet $SU(2)$ singlet scalar Φ_6 that only couples to right-handed up-type quarks.

5.2 Decay of the Color Sextet Scalar

The decay of the Φ_6 depends on its mass, M_{Φ_6}, and its couplings to quarks, f_{ij} $(i,j = u,c,t)$. To illustrate our reconstruction algorithm in the discussion of discovery, we consider the case where $M_{\Phi_6} > 350$ GeV and the Φ_6 decays into two onshell top quarks; other mass ranges are discussed in the conclusion section. Above threshold, the general expression for the decay partial widths of the sextet scalar are

$$\begin{aligned} \Gamma_{ii} &= \frac{3}{16\pi}|f_{ii}|^2 M_{\Phi_6}\lambda^{1/2}(1, r_i^2, r_i^2)(1-4r_i^2), \\ \Gamma_{ij} &= \frac{3}{8\pi}|f_{ij}|^2 M_{\Phi_6}\lambda^{1/2}(1, r_i^2, r_j^2)(1-r_i^2-r_j^2), \end{aligned} \tag{5.2}$$

where $\lambda(x,y,z) = (x-y-z)^2 - 4yz$ and $r_i = m_i/M_{\Phi_6}$.

By far, the most stringent bounds on these parameters come from $D^0 - \bar{D}^0$ mixing, to which Φ_6 would make a tree-level contribution proportional to $f_{11}f_{22}/M_{\Phi_6}^2$. The off-diagonal coupling f_{ij} will contribute to flavor violation processes, for instance $D \to \pi\pi$ which is proportional to $f_{12}f_{11}/M_{\Phi_6}^2$. The current bounds require that

$$f_{11}f_{22} \lesssim 10^{-6}; f_{11}f_{12} \lesssim 10^{-2}, \tag{5.3}$$

for M_{Φ_6} of a few hundred GeV to TeV mass range [102, 106, 107]. One will also expect less stringent constraints from one loop processes such as $c \to u\gamma$. To escape from the bound, for accessible values of M_{Φ_6} we expect at least one of the couplings, f_{11} or f_{22}, to be negligible. However, from our purely phenomenological perspective, we take the decay branching fraction BR$(\Phi_6 \to tt)$ to be a completely free parameter whose value may be determined at the LHC.

Because the sextet is a colored object, we need to consider the possibility of it hadronizing before decaying. For example, it may form a tetraquark-like bound state with $\bar{3}\bar{3}$, such as $\Phi_6\bar{u}\bar{u}$, $\Phi_6\bar{u}\bar{d}$, or $\Phi_6\bar{d}\bar{d}$, with charges $0, 1,$ or 2, respectively. If the total width is less than $\Lambda_{\rm QCD} \approx m_\pi$, then the colored object will hadronize before it decays. To determine the constraint imposed by the possibility of hadronization, in Fig. 5.1 we plot the contour for which decay width of Φ_6 is equal to $\Lambda_{\rm QCD}$ as a function of the couplings and the mass. Setting $f_{uu} = 0.001$, $f_{ut} = 0.001$, and eliminating any coupling to c, we see the possibility that a large portion of our parameter space will be protected from the risk of hadronization.

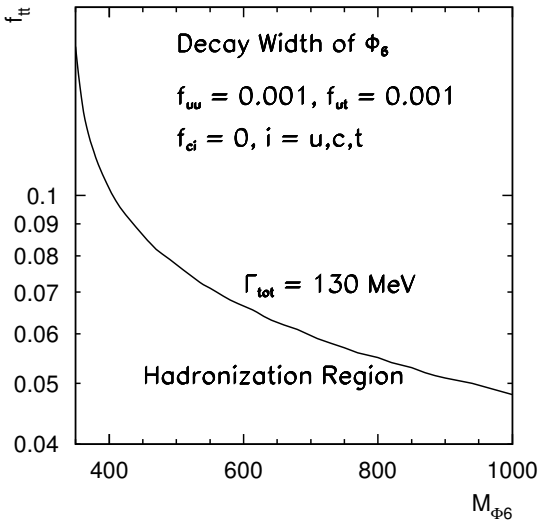

Figure 5.1: Decay width contour for Φ_6 in the mass and coupling plane.

5.3 Production of Φ_6

Because it carries color, Φ_6 can be produced directly through the QCD strong interaction at the LHC. The pair of $\bar{\Phi}_6\Phi_6$ is produced from gluon-gluon fusion or $q\bar{q}$ annihilation:

$$\begin{aligned} g(p_1) + g(p_2) &\to \bar{\Phi}_6(k_1) + \Phi_6(k_2) \\ q(p_1) + \bar{q}(p_2) &\to \bar{\Phi}_6(k_1) + \Phi_6(k_2). \end{aligned} \tag{5.4}$$

The total production cross section depends only on the mass of Φ_6, since the vertex is just the strong coupling, g_s, as shown in Eq. (5.6). By comparison, the electroweak production of $\bar{\Phi}_6\Phi_6$ is small enough to be neglected in our search.

From the scalar QCD gauge interaction

$$(D_\mu\Phi_6)^\dagger(D^\mu\Phi_6), \quad \text{where} \quad D_\mu = \partial_\mu - ig_sG_\mu^aT^a, \tag{5.5}$$

one may obtain the Feynman rules

$$\begin{aligned} G_\mu^a\Phi_6\bar{\Phi}_6 &: ig_s(p_1 - p_2)_\mu T^a \\ G_\mu^aG_\nu^b\Phi_6\bar{\Phi}_6 &: -ig_s^2g_{\mu\nu}(T^aT^b + T^bT^a). \end{aligned} \tag{5.6}$$

The momenta are assigned according to $V_\mu S(p_1)\bar{S}(p_2)$ and all momenta are outgoing. In group theory langauge, this is $6 \otimes \bar{6} = 27 \oplus 8 \oplus 1$.

The parton level cross sections for color sextet pair production are given by

$$\sigma(q\bar{q} \to \bar{\Phi}_6\Phi_6) = \pi C(3)C(R)\frac{d_8}{d_3^2}\frac{\alpha_s^2}{3s}\beta^3 = \frac{10\pi}{27s}\alpha_s^2\beta^3 \tag{5.7}$$

d_R	3	6	8
$C(R)$	$1/2$	$5/2$	3
$C_2(R)$	$4/3$	$10/3$	3

Table 5.1: Normalization factor $C(R)$ and quadratic Casimir $C_2(R)$ for $d_R = 3, 6, 8$ under $SU(3)$.

and

$$\begin{aligned}\sigma(gg \to \bar{\Phi}_6\Phi_6) &= d_R C_2(R)\pi\frac{\alpha_s^2}{6s}\frac{1}{d_8^2}[3\beta(3-5\beta^2) - 12C_2(R)\beta(\beta^2-2) \\ &+ \ln|\frac{\beta+1}{\beta-1}|(6C_2(R)(\beta^4-1) - 9(\beta^2-1)^2] \\ &= \frac{5\pi}{96s}\alpha_s^2[\beta(89-55\beta^2) + \ln|\frac{\beta+1}{\beta-1}|(11\beta^4+18\beta^2-29)]\ , \quad (5.8)\end{aligned}$$

where $\sqrt{s}$ is the total energy, $\beta = \sqrt{1-4M_{\Phi_6}^2/s}$ and R is 6 with the normalization factor C and Casimir C_2 satisfying

$$\text{Tr}[T_R^a T_R^b] = C(R)\delta^{ab} \text{ and } T_R^a T_R^a = C_2(R)\mathbf{1}. \quad (5.9)$$

We list the values for different representations under $SU(3)$ as in Table 5.1.

The QCD production cross sections for the color sextet scalar pair $\bar{\Phi}_6\Phi_6$ at both LHC and Tevatron are plotted in Fig. 5.2 with factorization scale $\mu_F = M_{\Phi_6}$, renormalization scale $\mu_R = m_Z$ and the CTEQ6L [108] parton distribution function (PDF). The matrix elements in our calculations here and elsewhere are generated by SUSY-Madgraph [109] with modified color factors. For comparison, we also show the pair production cross sections for $SU(3)_C$ triplet and octet scalars at the LHC. As we can see, the total production cross section of the sextet scalar is similar to that of the octet scalar, but is about one order maginitude larger than that of the triplet scalar, which can be understood from values of C and C_2 for different reprensentations in Table 5.1.

As discussed in the introduction, the color sextet scalar Φ_6 only couples to the right-handed up-type quark quark pair. Thus we may also have single production of a Φ_6 through

$$uu(cc) \to \Phi_6. \quad (5.10)$$

However, the production cross section is proportional to the coupling $|f_{uu}|^2$ and $|f_{cc}|^2$, and may therefore be suppressed due to the $D^0 - \bar{D}^0$ mixing constraint. Some studies of the single Φ_6 production at the Tevatron and the LHC have been done in Ref. [102].

5.4 Searching for the Color Sextet Scalar through $tt\bar{t}\bar{t}$

As discussed in the previous sections, the most distinct feature of the color sextet scalar is its decay mode $\Phi_6 \to tt$, which leads to a same-sign dilepton signature in the final state

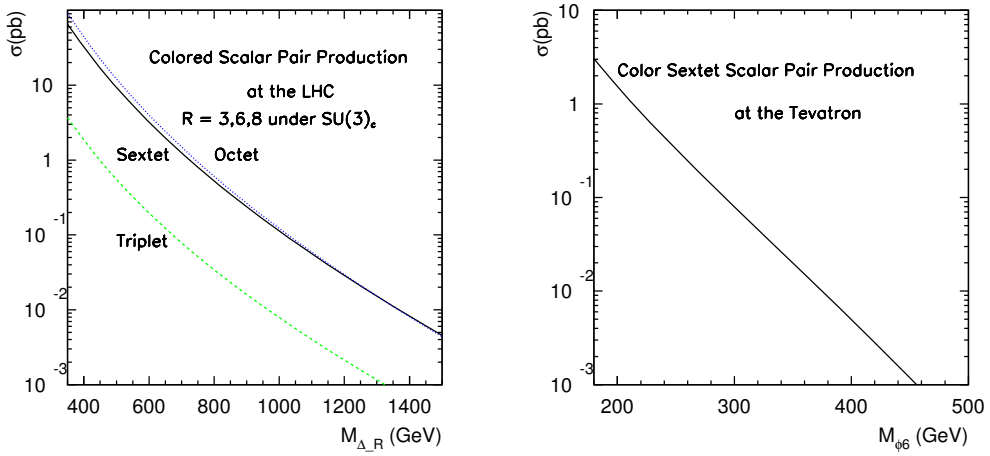

Figure 5.2: Production of $\bar{\Phi}_6\Phi_6$ at the LHC and Tevatron with $\mu_F = M_{\Phi_6}$, fixed scale $\alpha_S(\mu_R)$ with $\mu_R = m_Z$. The PDF set CTEQ6L has been used in all calculations.

if both top quarks decay semileptonically, i.e., $t \to W^+b \to \ell^+\nu b$. To avoid ambiguities in lepton assignments during reconstruction, we require the anti-top quark pair from the $\bar{\Phi}_6$ to decay hadronically. Hence, the final state of $\bar{\Phi}_6\Phi_6$ is

$$pp \to \bar{\Phi}_6\Phi_6 \to tt\bar{t}\bar{t} \to 4b + \ell^\pm\ell^\pm + \not{E}_T + Nj, \tag{5.11}$$

where $\ell = e$ and μ and $N \geq 4$ to allow initial and final state QCD radiation. In our study, however, the QCD radiation is not included. To get this final state, the decay branching ratio will be

$$\text{BR} = \text{BR}^2(\Phi_6 \to tt) \times \left(\frac{2}{9}\right)^2 \times \left(\frac{2}{3}\right)^2 \times 2, \tag{5.12}$$

where the situation that the top quark decays hadronically and the anti-top quark decays semileptonically is also included. Figure 5.2 also clearly shows that a color sextet with $M_{\Phi_6} \geq 350$ GeV will not be bounded by Tevatron data, as the same-sign dilepton plus multi-jet final state from $tt\bar{t}\bar{t}$ will be less than one event for 2 fb^{-1} luminosity.

To illustrate the kinematic features of the color sextet scalar pair, we consider the decay process $\Phi_6\bar{\Phi}_6 \to tt\bar{t}\bar{t} \to bb\bar{b}\bar{b}\ell^+\ell'^+ + 4jets$ and take $M_{\Phi_6} = 600$ GeV. The leading and second-leading jet p_T distributions are shown in Fig. 5.3. The typical hardness of these jets is the basis for one of our selection cuts introduced later in this section. In order to simulate the detector effects on the energy-momentum measurements, we smear the electromagnetic energy and the muon momentum by a Gaussian distribution whose width is parameterized

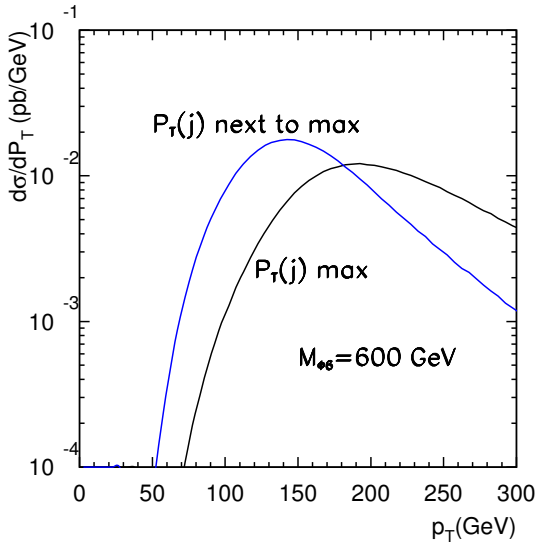

Figure 5.3: max$\{p_T^J\}$ and next-to-max$\{p_T^J\}$

as [110]

$$\frac{\Delta E}{E} = \frac{a_{cal}}{\sqrt{E/\mathrm{GeV}}} \oplus b_{cal}, \quad a_{cal} = 5\%, b_{cal} = 0.55\%, \tag{5.13}$$

$$\frac{\Delta p_T}{p_T} = \frac{a_{track} p_T}{\mathrm{TeV}} \oplus \frac{b_{track}}{\sqrt{\sin\theta}}, \quad a_{track} = 15\%, b_{track} = 0.5\%. \tag{5.14}$$

The jet energies are also smeared using the same Gaussian formula as in Eq. (5.13), but with [110]

$$a_{cal} = 100\%, \quad b_{cal} = 5\%. \tag{5.15}$$

We first reconstruct the two on-shell hadronically decaying Ws. Our procedure is to consider all dijet invariant masses except for those containing one of the two tagged b-jets, since we require b-tagging in the event selection discussed later, and choose the two closest M_{jj} combinations, which we then require to lie within the mass window

$$|M_{jj} - m_W| < 15 \text{ GeV}. \tag{5.16}$$

From this, we get the two reconstructed W momenta. We then consider all combinations of reconstructed p_W with all jets and again choose the two closest invariant masses M_{jW}. In this way, we reconstruct the two hadronically decaying anti-top quarks. The distributions of these reconstructed invariant masses are shown in Fig. 5.4.

Once we have the reconstructed two anti-top quarks, the reconstruction of the sextet $(\bar{\Phi})$ can be done using the 6-jet invariant mass M_{6j} for the two hadronic anti-top quarks.

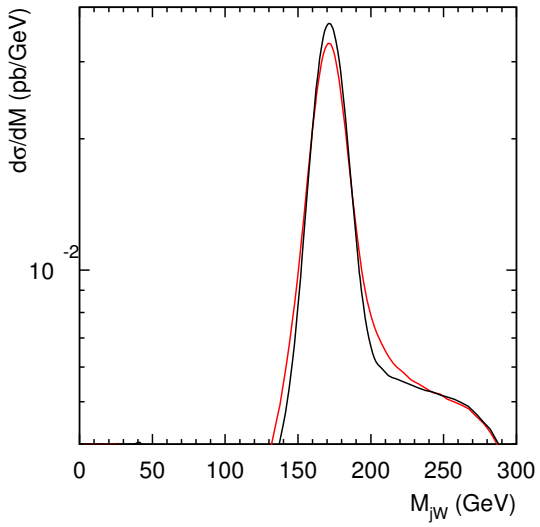

Figure 5.4: Reconstructed hadronic top pair. The black (red) line represents the first (second) reconstructed hadronically decaying anti-top quark.

Although the production of neutrinos prevents us from fully reconstructing the sextet which produces the leptonic decays, we may reconstruct the transverse mass M_T for the remaining two jets plus same-sign dilepton and $\not{E}_T$ as

$$M_T = \sqrt{(\sum_j E_T + \sum_\ell E_T + \not{E}_T)^2 - (\sum \vec{p}(j) + \sum \vec{p}(\ell) + \vec{\not{p}})_T^2}. \tag{5.17}$$

As seen in Fig. 5.5, our reconstruction shows a clear resonance in both the M_{6j} and M_T distributions.

Finally, since the two anti-top quarks may be fully reconstructed, we can boost back to the rest frame of the $\bar{\Phi}_6$ and study its spin. As shown in Fig. 5.6, the angular distribution of the anti-quark clearly shows that the $\bar{\Phi}_6$ is a scalar. Since there are two missing neutrinos from the decay of two top quarks, it is challenging to fully reconstruct the top quark's momentum and study the spin information of top quarks, which can be used to check this model, since Φ_6 only decays into a right-handed top quark pair. We leave this for future work.

We next consider the backgrounds for our signal. We require at least 2 tagged b-jets plus a same-sign dilepton and multijet. The irreducible SM background for this final state consists of $t\bar{t}W^\pm{+}Nj$, $bb{+}W^\pm W^\pm{+}Nj$ and $t\bar{t}t\bar{t}$. We estimate the QCD $bb{+}W^\pm W^\pm{+}Nj$ background by computing $jjW^\pm W^\pm$ production. This is only 14 fb, and one expects the $bb + W^\pm W^\pm + Nj$ is about three orders of magnitude lower and therefore < 0.1 fb. The SM 4-top $t\bar{t}t\bar{t}$ is less than 0.1 fb to start with. The leading background thus comes from

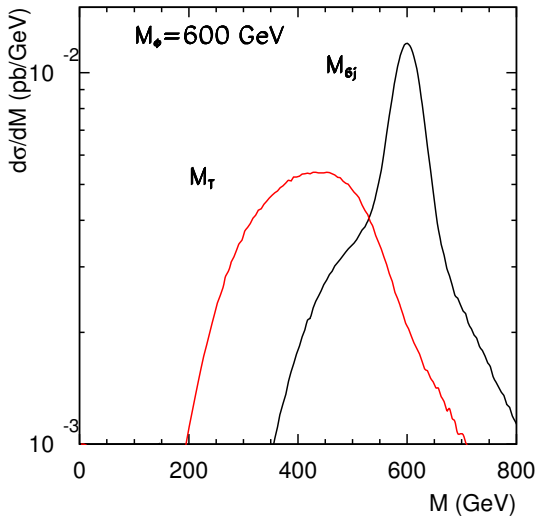

Figure 5.5: Reconstructed Sextet from m_{6j} and M_T.

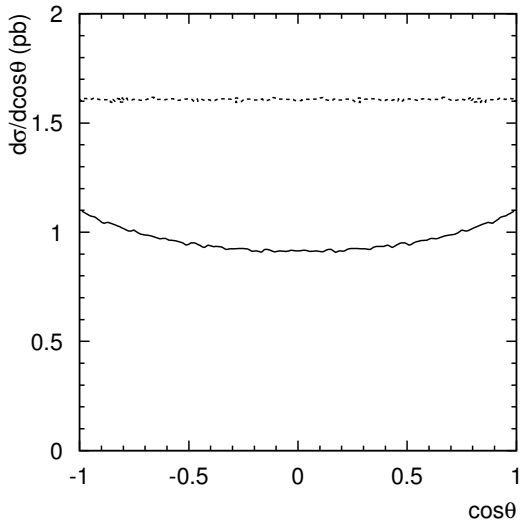

Figure 5.6: Distribution of $\cos\theta$ between reconstructed top momentum and reconstructed sextet momentum. Dashed (solid) line shows the distribution without (with) smearing effects and kinematic cuts.

$t\bar{t}W^{\pm}$ with one hadronic top decay and one semileptonic top decay with the same sign as $W^{\pm}$ leptonic decay.

We propose the following selection cuts:

- min$\{p_T(j)\} > 15$ GeV, max$\{p_T(j)\} > 100$ GeV, next-to-max$\{p_T(j)\} > 75$ GeV, $|\eta(j) < 3.0|$
- same-sign dilepton with $p_T(\ell) > 15$ GeV, $|\eta(\ell) < 2.8|$
- $\Delta R_{jj},\ \Delta R_{jl},\ \Delta R_{ll} > 0.4$
- at least two b-tagged jets
- $\not{E}_T > 25$ GeV.

Since the production rate of our signal only depends on the mass M_{Φ_6} and branching ratio of Φ_6 decay to a top quark pair, we scan these two parameters to study the discovery potential. We summarize our results in Fig. 5.7 as the signal production rate for $bb\bar{b}\bar{b} + \ell^\pm\ell^\pm + \not{E}_T + 4j$ from $\Phi_6\bar{\Phi}_6$ with SM $t\bar{t}W^\pm$ background included. We use a factor of 25% in both plots in Fig. 5.7 for tagging two b jets with 50% effeciency to tag each b-jet. The SM background is taken as 1 fb in the significance contour. As we can see in the left plot of Fig. 5.7, for 100 fb^{-1} luminosity, the statistical significance can surpass the 5σ level for $M_{\Phi_6} \lesssim 800\text{GeV}$ if BR($\Phi \to tt$) is about 0.5. Also note that the mass of the sextet scalar can be determined by reconstructing two hadronically decaying top (or anti-top) quarks, and the branching ratio of $\Phi_6 \to tt$ can be roughly estimated from the total signal event rate if one can understand the backgorund sufficiently well. No reconstruction selection has been implemented since we did not simulate the events with initial state/final state radiation and the reconstruction efficiency is thus unknown. In principle, we expect that the $S/\sqrt{B}$ can be further improved by including reconstruction.

5.5 Conclusion

In this paper, we discuss the production of a new exotic particle, a color sextet scalar, at the CERN Large Hadron Collider. Taking a purely phemenological approach, we discuss the discovery of the color sextet scalar through its decay into a top-top quark pair. The unique feature of same-sign dilepton plus multijet makes it easy to identify and reconstruct the color sextet scalar object. Due to its large QCD production, it is possible to cover the color sextet scalar up to a mass range of 1 TeV for 100 fb^{-1} integrated luminosity.

In the text, we only consider the case of $M_{\Phi_6} > 2m_t$, where Φ_6 decays into two on-shell top quarks. In the case $2M_{\Phi_6} < m_Z$, there is a possiblity of a Z decaying into a sextet pair, since Φ_6 carries a $U(1)_Y$ charge, which we expect is highly constrained by LEP data. We also expect to find strong constraints from Tevatron data. For example, for M_{Φ_6} just above $m_t + m_b$ threshold, the $\bar{\Phi}_6\Phi_6$ signal will directly contribute to the $t\bar{t}X$ sample as the offshell top decay products are soft.

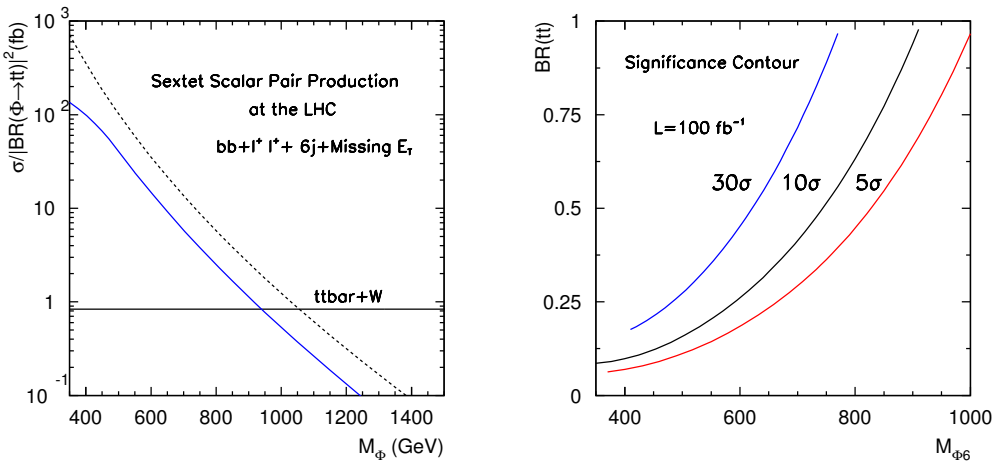

Figure 5.7: Production rate normalized by BR$(\Phi_6 \to tt)^2$ and significance contour. Dashed (solid) curves in the left plot represent production before (after) selection cuts.

Chapter 6

Conclusions

The standard model, described in Section 1.1, has been a great success of modern physics – with a few modest assumptions, it has been consistently able to describe phenomena observed below the electroweak scale. With the LHC now in operation, we are in an exciting era of the exploration of physics at the TeV scale. As we discussed in Section 1.2, we have good reason to expect new physics at this energy scale, and the LHC may help us to understand the hierarchy problem and the nature of dark matter. We may find the remaining unobserved ingredient in the SM, the Higgs boson, and we may produce new physics beyond the standard model, possibly in the form of superpartners, Kaluza-Klein excitations of SM particles, or something entirely different and as yet theoretically unexplored.

In order to make the most of the many high-energy collisions that will take place at the LHC and future colliders, we must know which events to look for and how to extract information about the new particles we produce from the experimental data. In Chapter 2 we proposed a new technique for mass measurement in boosted decay systems. As discussed in Section 1.3, this is a task which is made more difficult for BSM physics, as many scenarios provide a dark matter candidate which goes unseen in the detector. Focusing on the transverse direction is a common approach to this challenge, and the sensitivity of the M_{CT2} variable on boosts from upstream decays and radiation makes it a useful tool for mass determination in short decay chains. In Chapter 2, we demonstrated the effectiveness of our technique for a specific SUSY model, but it could be useful in many BSM scenarios.

In Chapters 3 and 4, we introduced a new technique for measuring spins of particles produced in collider experiments. This is important for distinguishing models such as SUSY and UED, which provide particles with similar masses but different spins, which we demonstrated in Chapter 3. In order to show that this technique is really experimentally feasible, we demonstrated in Chapter 4 that the spins of weak gauge bosons could be determined using existing data from both an e^+e^- collider, LEP, and a hadron collider, Tevatron. This required careful treatment of the real effects of selection cuts, and we proposed a technique for extracting a clean signal from the data.

Finally, in Chapter 5, we proposed a search at the LHC for color sextet scalars. Because

of their QCD interactions, TeV scale sextet scalars could be produced in great abundance at hadron colliders such as the LHC, and their unique couplings to quarks allow them to generate a final state containing same-sign dileptons, which has a relatively small background. Our final state contains several jets, and we have determined a scheme which allows us to reconstruct the sextet. Ultimately, we find that searching in this channel at the LHC is feasible for a large range of masses and couplings.

We have embarked upon the LHC era, and the coming years are certain to be challenging but ultimately rewarding.

Bibliography

[1] C. A. Baker, D. D. Doyle, P. Geltenbort, K. Green, M. G. D. van der Grinten, P. G. Harris, P. Iaydjiev, S. N. Ivanov *et al.*, "An Improved experimental limit on the electric dipole moment of the neutron," Phys. Rev. Lett. **97**, 131801 (2006). [hep-ex/0602020].

[2] L. Wolfenstein, "Parametrization of the Kobayashi-Maskawa Matrix," Phys. Rev. Lett. **51**, 1945 (1983).

[3] R. Barate *et al.* [LEP Working Group for Higgs boson searches and ALEPH and DELPHI and L3 and OPAL Collaborations], "Search for the standard model Higgs boson at LEP," Phys. Lett. **B565**, 61-75 (2003). [hep-ex/0306033].

[4] T. Aaltonen *et al.* [CDF and D0 Collaboration], "Combined CDF and D0 Upper Limits on Standard Model Higgs Boson Production with up to 8.2 fb^{-1} of Data," [arXiv:1103.3233 [hep-ex]].

[5] B. W. Lee, C. Quigg, H. B. Thacker, "Weak Interactions at Very High-Energies: The Role of the Higgs Boson Mass," Phys. Rev. **D16**, 1519 (1977).

[6] B. W. Lee, C. Quigg, H. B. Thacker, "The Strength of Weak Interactions at Very High-Energies and the Higgs Boson Mass," Phys. Rev. Lett. **38**, 883-885 (1977).

[7] T. Hambye, K. Riesselmann, "SM Higgs mass bounds from theory," [hep-ph/9708416].

[8] P. Langacker, "Introduction to the Standard Model and Electroweak Physics," [arXiv:0901.0241 [hep-ph]].

[9] [ALEPH, CDF, D0, DELPHI, L3, OPAL, SLD, the LEP Electroweak Working Group, the Tevatron Electroweak Working Group, and the SLD electroweak and heavy flavour groups Collaboration], "Precision electroweak measurements and constraints on the Standard Model" (2010).

[10] S. Weinberg, "The Cosmological Constant Problem," Rev. Mod. Phys. **61**, 1-23 (1989).

[11] G. G. Raffelt, "Dark matter: Motivation, candidates and searches," [hep-ph/9712538].

[12] G. Bertone, D. Hooper, J. Silk, "Particle dark matter: Evidence, candidates and constraints," Phys. Rept. **405**, 279-390 (2005). [hep-ph/0404175].

[13] H. Murayama, "Physics Beyond the Standard Model and Dark Matter," [arXiv:0704.2276 [hep-ph]].

[14] F. Zwicky, "Spectral displacement of extra galactic nebulae," Helv. Phys. Acta **6**, 110-127 (1933).

[15] E. Komatsu *et al.* [WMAP Collaboration], "Seven-Year Wilkinson Microwave Anisotropy Probe (WMAP) Observations: Cosmological Interpretation," Astrophys. J. Suppl. **192**, 18 (2011) [arXiv:1001.4538 [astro-ph.CO]].

[16] R. H. Cyburt, B. D. Fields, K. A. Olive, E. Skillman, "New BBN limits on physics beyond the standard model from He-4," Astropart. Phys. **23**, 313-323 (2005). [astro-ph/0408033].

[17] W. J. Percival, S. Cole, D. J. Eisenstein, R. C. Nichol, J. A. Peacock, A. C. Pope, A. S. Szalay, "Measuring the Baryon Acoustic Oscillation scale using the SDSS and 2dFGRS," Mon. Not. Roy. Astron. Soc. **381**, 1053-1066 (2007). [arXiv:0705.3323 [astro-ph]].

[18] C. .Kraus, B. Bornschein, L. Bornschein, J. Bonn, B. Flatt, A. Kovalik, B. Ostrick, E. W. Otten *et al.*, "Final results from phase II of the Mainz neutrino mass search in tritium beta decay," Eur. Phys. J. **C40**, 447-468 (2005). [hep-ex/0412056].

[19] S. Tremaine, J. E. Gunn, "Dynamical Role of Light Neutral Leptons in Cosmology," Phys. Rev. Lett. **42**, 407-410 (1979).

[20] D. N. C. Lin, S. M. Faber, "Some implications of nonluminous matter in dwarf spheroidal galaxies," Astrophys. J. **266**, L21-L25 (1983).

[21] S. Hannestad, G. G. Raffelt, "Neutrino masses and cosmic radiation density: Combined analysis," JCAP **0611**, 016 (2006). [astro-ph/0607101].

[22] P. Tisserand *et al.* [EROS-2 Collaboration], "Limits on the Macho Content of the Galactic Halo from the EROS-2 Survey of the Magellanic Clouds," Astron. Astrophys. **469**, 387 (2007) [arXiv:astro-ph/0607207].

[23] S. P. Martin, "A Supersymmetry primer," In *Kane, G.L. (ed.): Perspectives on supersymmetry* 1-98. [hep-ph/9709356].

[24] H. Nishino *et al.* [Super-Kamiokande Collaboration], "Search for Proton Decay via p $\rightarrow$ e+ pi0 and p $\rightarrow$ mu+ pi0 in a Large Water Cherenkov Detector," Phys. Rev. Lett. **102**, 141801 (2009). [arXiv:0903.0676 [hep-ex]].

[25] B. A. Dobrescu, "Particle physics in extra dimensions," in *The Dawn of the LHC Era,* Proceedings of the 2008 Theoretical Advanced Study Institute in Elementary Particle Physics, ed. T. Han (World Scientific, New Jersey, 2010).

[26] D. Hooper, S. Profumo, "Dark matter and collider phenomenology of universal extra dimensions," Phys. Rept. **453**, 29-115 (2007). [hep-ph/0701197].

[27] K. Nakamura *et al.* [Particle Data Group Collaboration], "Review of particle physics," J. Phys. G **G37**, 075021 (2010).

[28] N. Arkani-Hamed, S. Dimopoulos, G. R. Dvali, "The Hierarchy problem and new dimensions at a millimeter," Phys. Lett. **B429**, 263-272 (1998). [hep-ph/9803315].

[29] D. J. Kapner, T. S. Cook, E. G. Adelberger, J. H. Gundlach, B. R. Heckel, C. D. Hoyle and H. E. Swanson, "Tests of the gravitational inverse-square law below the dark-energy length scale," Phys. Rev. Lett. **98**, 021101 (2007) [arXiv:hep-ph/0611184].

[30] L. Randall, R. Sundrum, "A Large mass hierarchy from a small extra dimension," Phys. Rev. Lett. **83**, 3370-3373 (1999). [hep-ph/9905221].

[31] T. Appelquist, H. -C. Cheng, B. A. Dobrescu, "Bounds on universal extra dimensions," Phys. Rev. **D64**, 035002 (2001). [hep-ph/0012100].

[32] W. S. Cho, K. Choi, Y. G. Kim and C. B. Park, Phys. Rev. Lett. **100**, 171801 (2008) [arXiv:0709.0288]; W. S. Cho, K. Choi, Y. G. Kim and C. B. Park, J. High Energy Phys. **02**, 035 (2008) [arXiv:0711.4526].

[33] B. Gripaios, J. High Energy Phys. **02**, 053 (2008) [arXiv:0709.2740]; A. J. Barr, B. Gripaios and C. G. Lester, J. High Energy Phys. **02**, 014 (2008), J. High Energy Phys. **11**, 096 (2009) [arXiv:0711.4008]; M. Burns, K. Kong, K. T. Matchev and M. Park, J. High Energy Phys. **03**, 143 (2009) [arXiv:0810.5576].

[34] C. G. Lester and D. J. Summers, Phys. Lett. B **463**, 99 (1999) [hep-ph/9906349]; A. Barr, C. G. Lester and P. Stephens, J. Phys. **G29** (2003) 2343 [hep-ph/0304226].

[35] W. S. Cho, J. E. Kim and J. H. Kim Phys. Rev. D **81**, 095010 (2010) [arXiv:0912.2354]; A. J. Barr, C. Gwenlan, C. G. Lester, C. J. Young, [arXiv:1006.2568].

[36] R. Tovey, J. High Energy Phys. **04**, 034 (2008) [arXiv:0802.2879]; M. Serna, J. High Energy Phys. **06**, 004 (2008) [arXiv:0804.3344]; G. Polesello and D. R. Tovey, J. High Energy Phys. **03**, 030 (2010) [arXiv:0910.0174].

[37] S. K. Mandal, M. Nojiri, M. Sudano, T. T. Yanagida, [arXiv:1004.4164].

[38] T. Sjostrand, S. Mrenna, and P. Skands, J. High Energy Phys. **05**, 026 (2006).

[39] PGS 4, J. Conway, http://www.physics.ucdavis.edu /∼conway/research /software/pgs/pgs4-general.htm.

[40] The ATLAS Collaboration, CERN-OPEN-2008-020.

[41] W. S. Cho, W. Klemm, S. Mandal, M. M. Nojiri, Work in progress.

[42] S. Weinberg, "Implications of dynamical symmetry breaking," Phys. Rev. D **13**, 974 (1976).

[43] S. Weinberg, "Implications Of Dynamical Symmetry Breaking: An Addendum," Phys. Rev. D **19**, 1277 (1979).

[44] L. Susskind, "Dynamics of spontaneous symmetry breaking in the Weinberg-Salam theory," Phys. Rev. D **20**, 2619 (1979).

[45] G. t Hooft, in *Recent developments in gauge theories,* Proceedings of the NATO Advanced Summer Institute, Cargese 1979, ed. G. t Hooft *et al.* (Plenum, New York 1980).

[46] J. Wess and B. Zumino, "Supergauge Transformations in Four-Dimensions," Nucl. Phys. B **70**, 39 (1974).

[47] N. Arkani-Hamed, S. Dimopoulos and G. R. Dvali, "Phenomenology, astrophysics and cosmology of theories with sub-millimeter dimensions and TeV scale quantum gravity," Phys. Rev. D **59**, 086004 (1999) [arXiv:hep-ph/9807344].

[48] I. Antoniadis, N. Arkani-Hamed, S. Dimopoulos and G. R. Dvali, "New dimensions at a millimeter to a Fermi and superstrings at a TeV," Phys. Lett. B **436**, 257 (1998) [arXiv:hep-ph/9804398].

[49] I. Antoniadis, "A Possible new dimension at a few TeV," Phys. Lett. B **246**, 377 (1990).

[50] I. Antoniadis and K. Benakli, "Limits on extra dimensions in orbifold compactifications of superstrings," Phys. Lett. B **326**, 69 (1994) [arXiv:hep-th/9310151].

[51] L. Randall and R. Sundrum, "An alternative to compactification," Phys. Rev. Lett. **83**, 4690 (1999) [arXiv:hep-th/9906064].

[52] M. Weinstein, "Conserved Currents, Their Commutators And The Symmetry Structure Of Renormalizable Theories Of Electromagnetic, Weak And Strong Interactions," Phys. Rev. D **8**, 2511 (1973).

[53] N. Arkani-Hamed, A. G. Cohen and H. Georgi, "Electroweak symmetry breaking from dimensional deconstruction," Phys. Lett. B **513**, 232 (2001) [arXiv:hep-ph/0105239].

[54] H. C. Cheng, K. T. Matchev and M. Schmaltz, "Bosonic supersymmetry? Getting fooled at the LHC," Phys. Rev. D **66**, 056006 (2002) [arXiv:hep-ph/0205314].

[55] K. Kong and K. T. Matchev, "Phenomenology of universal extra dimensions," AIP Conf. Proc. **903**, 451 (2007) [arXiv:hep-ph/0610057].

[56] M. Battaglia, A. K. Datta, A. De Roeck, K. Kong and K. T. Matchev, "Contrasting supersymmetry and universal extra dimensions at colliders," *In the Proceedings of 2005 International Linear Collider Workshop (LCWS 2005), Stanford, California, 18-22 Mar 2005, pp 0302* [arXiv:hep-ph/0507284].

[57] G. Burdman, B. A. Dobrescu and E. Ponton, "Resonances from Two Universal Extra Dimensions," Phys. Rev. D **74**, 075008 (2006) [arXiv:hep-ph/0601186].

[58] M. Battaglia, A. Datta, A. De Roeck, K. Kong and K. T. Matchev, "Contrasting supersymmetry and universal extra dimensions at the CLIC multi-TeV e+ e- collider," JHEP **0507**, 033 (2005) [arXiv:hep-ph/0502041].

[59] S. Y. Choi, K. Hagiwara, H. U. Martyn, K. Mawatari and P. M. Zerwas, "Spin analysis of supersymmetric particles," Eur. Phys. J. C **51**, 753 (2007) [arXiv:hep-ph/0612301].

[60] L. T. Wang and I. Yavin, "Spin Measurements in Cascade Decays at the LHC," JHEP **0704**, 032 (2007) [arXiv:hep-ph/0605296].

[61] A. J. Barr, "Using lepton charge asymmetry to investigate the spin of supersymmetric particles at the LHC," Phys. Lett. B **596**, 205 (2004) [arXiv:hep-ph/0405052].

[62] A. J. Barr, "Measuring slepton spin at the LHC," JHEP **0602**, 042 (2006) [arXiv:hep-ph/0511115].

[63] J. M. Smillie and B. R. Webber, "Distinguishing spins in supersymmetric and universal extra dimension models at the Large Hadron Collider," JHEP **0510**, 069 (2005) [arXiv:hep-ph/0507170].

[64] A. Alves and O. Eboli, "Unravelling the sbottom spin at the CERN LHC," Phys. Rev. D **75**, 115013 (2007) [arXiv:0704.0254 [hep-ph]].

[65] H. Murayama, "Confusing Signals of Supersymmetry," International Linear Collider Workshop (LCWS2000), Oct. 24-28, 2000, Fermilab

[66] R. Schwitters *et al.*, "Azimuthal Asymmetry In Inclusive Hadron Production By E+ E- Annihilation," Phys. Rev. Lett. **35**, 1320 (1975).

[67] D. Berdine, N. Kauer and D. Rainwater, "Breakdown of the Narrow Width Approximation for New Physics," Phys. Rev. Lett. **99**, 111601 (2007) [arXiv:hep-ph/0703058].

[68] T. Tsukamoto, K. Fujii, H. Murayama, M. Yamaguchi and Y. Okada, "Precision study of supersymmetry at future linear e+ e- colliders," Phys. Rev. D **51**, 3153 (1995).

[69] H. C. Cheng, J. F. Gunion, Z. Han, G. Marandella and B. McElrath, "Mass Determination in SUSY-like Events with Missing Energy," arXiv:0707.0030 [hep-ph].

[70] P. B. Wilson, "Future e+e- Linear colliders and beam-beam effects," SLAC-PUB-3985, May 1986.

[71] A. Freitas *et al.*, "Sleptons at e+ e- linear colliders," arXiv:hep-ph/0211108.

[72] J. L. Feng and M. E. Peskin, "Selectron studies at e- e- and e+ e- colliders," Phys. Rev. D **64**, 115002 (2001) [arXiv:hep-ph/0105100].

[73] T. Behnke, S. Bertolucci, R. D. Heuer and R. Settles, "TESLA: The superconducting electron positron linear collider with an integrated X-ray laser laboratory. Technical design report. Pt. 4: A detector for TESLA," `http://tesla.desy.de/new_pages/TDR_CD/start.html`

[74] H. Murayama and M. E. Peskin, "Physics opportunities of e+ e- linear colliders," Ann. Rev. Nucl. Part. Sci. **46**, 533 (1996) [arXiv:hep-ex/9606003].

[75] N. Ghodbane and H. U. Martyn, "Compilation of SUSY particle spectra from Snowmass 2001 benchmark models," in *Proc. of the APS/DPF/DPB Summer Study on the Future of Particle Physics (Snowmass 2001)* ed. N. Graf, arXiv:hep-ph/0201233.

[76] B. C. Allanach *et al.*, "The Snowmass points and slopes: Benchmarks for SUSY searches," in *Proc. of the APS/DPF/DPB Summer Study on the Future of Particle Physics (Snowmass 2001)* ed. N. Graf, *In the Proceedings of APS / DPF / DPB Summer Study on the Future of Particle Physics (Snowmass 2001), Snowmass, Colorado, 30 Jun - 21 Jul 2001, pp P125* [arXiv:hep-ph/0202233].

[77] H. C. Cheng, K. T. Matchev and M. Schmaltz, "Radiative corrections to Kaluza-Klein masses," Phys. Rev. D **66**, 036005 (2002) [arXiv:hep-ph/0204342].

[78] `http://home.fnal.gov/~kckong/mued/`

[79] A. Pukhov, "CalcHEP 3.2: MSSM, structure functions, event generation, batchs, and generation of matrix elements for other packages," arXiv:hep-ph/0412191.

[80] H. Murayama, I. Watanabe and K. Hagiwara, "HELAS: HELicity Amplitude Subroutines for Feynman diagram evaluations."

[81] S. Kawabata, "A New Monte Carlo Event Generator For High-Energy Physics," Comput. Phys. Commun. **41**, 127 (1986).

[82] F. E. Paige, "Supersymmetry signatures at the CERN LHC," arXiv:hep-ph/9801254.

[83] C. Csáki, C. Grojean, H. Murayama, L. Pilo and J. Terning, "Gauge theories on an interval: Unitarity without a Higgs," Phys. Rev. D **69**, 055006 (2004) [arXiv:hep-ph/0305237].

[84] C. Csáki, C. Grojean, L. Pilo and J. Terning, "Towards a realistic model of Higgsless electroweak symmetry breaking," Phys. Rev. Lett. **92**, 101802 (2004) [arXiv:hep-ph/0308038].

[85] K. Gottfried and J. D. Jackson, "On the Connection between Production Mechanism and Decay of Resonances at High Energies," Il Nouvo Cimento **33**, 309 (1964).

[86] A. Heister *et al.* [ALEPH Collaboration], "Measurement of W pair production in e+ e- collisions at centre-of-mass energies from 183-GeV to 209-GeV," Eur. Phys. J. C **38**, 147 (2004).

[87] G. Abbiendi *et al.* [OPAL Collaboration], "Measurement of the mass and width of the W boson," Eur. Phys. J. C **45**, 307 (2006) [arXiv:hep-ex/0508060].

[88] J. Abdallah *et al.* [DELPHI Collaboration], "Measurement of the W pair production cross-section and W branching ratios in e+ e- collisions at s**(1/2) = 161-GeV to 209-GeV," Eur. Phys. J. C **34**, 127 (2004) [arXiv:hep-ex/0403042].

[89] P. Achard *et al.* [L3 Collaboration], "Measurement of the cross section of W-boson pair production at LEP," Phys. Lett. B **600**, 22 (2004) [arXiv:hep-ex/0409016].

[90] T. Aaltonen *et al.* [CDF - Run II Collaboration], "Measurement of Inclusive Jet Cross Sections in $Z/g * *(\rightarrow ee)+$ jets Production in $p\bar{p}$ Collisions at $\sqrt{s} = 1.96$ TeV," arXiv:0711.3717 [hep-ex].

[91] V. M. Abazov *et al.* [D0 Collaboration], "Measurement of the ratios of the Z/G* + ¿= n jet production cross sections to the total inclusive Z/G* cross section in ppbar collisions at sqrt(s) = 1.96 TeV," Phys. Lett. B **658**, 112 (2008) [arXiv:hep-ex/0608052].

[92] M. R. Whalley, D. Bourilkov and R. C. Group, "The Les Houches accord PDFs (LHAPDF) and LHAGLUE," arXiv:hep-ph/0508110.

[93] M. L. Mangano, M. Moretti, F. Piccinini, R. Pittau and A. D. Polosa, "ALPGEN, a generator for hard multiparton processes in hadronic collisions," JHEP **0307**, 001 (2003) [arXiv:hep-ph/0206293].

[94] A. de Gouvêa, A. Friedland and H. Murayama, "Seasonal variations of the Be-7 solar neutrino flux," Phys. Rev. D **60**, 093011 (1999) [arXiv:hep-ph/9904399].

[95] K. Ackerstaff *et al.* [OPAL Collaboration], "Measurement of the mass of the W boson in e+ e- collisions at s**(1/2) = 161-GeV," Phys. Lett. B **389**, 416 (1996).

[96] CDF Collaboration, "Measurements of Differential Cross Sections for b-jet Production in Assosiation with Z-bosons at $\sqrt{s} = 1.96$ TeV", to be published.

[97] C. M. Ginsburg [Representing the CDF Collaboration], "CDF Run 2 muon system," Eur. Phys. J. C **33**, S1002 (2004).

[98] S. Errede and S. H. H. Tye, "Stable / Exotic Particle Production And Detection At The Ssc," Summary Report of the Stable/Exotic Particles Working Group on SSC, Snowmass, 1984. H. Tanaka and I. Watanabe, "Color sextet quark productions at hadron colliders," Int. J. Mod. Phys. A **7**, 2679 (1992).

[99] J. C. Pati and A. Salam, "Lepton Number As The Fourth Color," Phys. Rev. D **10**, 275 (1974) [Erratum-ibid. D **11**, 703 (1975)]. R. N. Mohapatra and R. E. Marshak, "Local B-L Symmetry Of Electroweak Interactions, Majorana Neutrinos And Neutron Oscillations," Phys. Rev. Lett. **44**, 1316 (1980) [Erratum-ibid. **44**, 1643 (1980)].

[100] P. Fileviez Perez, "Renormalizable Adjoint SU(5)," Phys. Lett. B **654**, 189 (2007) [arXiv:hep-ph/0702287].

[101] Z. Chacko and R. N. Mohapatra, "Supersymmetric SU(2)L x SU(2)R x SU(4)c and observable neutron antineutron oscillation," Phys. Rev. D **59**, 055004 (1999) [arXiv:hep-ph/9802388].

[102] R. N. Mohapatra, N. Okada and H. B. Yu, "Diquark Higgs at LHC," Phys. Rev. D **77**, 011701 (2008) [arXiv:0709.1486 [hep-ph]].

[103] K. S. Babu, R. N. Mohapatra and S. Nasri, "Post-sphaleron baryogenesis," Phys. Rev. Lett. **97**, 131301 (2006) [arXiv:hep-ph/0606144].

[104] L. J. Hall and A. E. Nelson, "Heavy Gluons And Monojets," Phys. Lett. B **153**, 430 (1985). R. S. Chivukula, M. Golden and E. H. Simmons, "Multi - jet physics at hadron colliders," Nucl. Phys. B **363**, 83 (1991). M. I. Gresham and M. B. Wise, "Color Octet Scalar Production at the LHC," Phys. Rev. D **76**, 075003 (2007) [arXiv:0706.0909 [hep-ph]]. B. A. Dobrescu, K. Kong and R. Mahbubani, "Massive color-octet bosons and pairs of resonances at hadron colliders," arXiv:0709.2378 [hep-ph]. M. Gerbush, T. J. Khoo, D. J. Phalen, A. Pierce and D. Tucker-Smith, "Color-octet scalars at the LHC," Phys. Rev. D **77**, 095003 (2008) [arXiv:0710.3133 [hep-ph]].

C. Kilic, T. Okui and R. Sundrum, "Colored Resonances at the Tevatron: Phenomenology and Discovery Potential in Multijets," JHEP **0807**, 038 (2008) [arXiv:0802.2568 [hep-ph]]. M. V. Martynov and A. D. Smirnov, "Colored scalar particles production in pp-collisions and possible mass limits for scalar gluons from future LHC data," arXiv:0807.4486 [hep-ph]. P. Fileviez Perez, R. Gavin, T. McElmurry and F. Petriello, "Grand Unification and Light Color-Octet Scalars at the LHC," arXiv:0809.2106 [hep-ph]. C. Kilic, S. Schumann and M. Son, "Searching for Multijet Resonances at the LHC," arXiv:0810.5542 [hep-ph].

[105] See for example: V. Barger, T. Han and D. G. E. Walker, "Top Quark Pairs at High Invariant Mass - A Model-Independent Discriminator of New Physics at the LHC," Phys. Rev. Lett. **100**, 031801 (2008) [arXiv:hep-ph/0612016]. B. Lillie, L. Randall and L. T. Wang, "The Bulk RS KK-gluon at the LHC," JHEP **0709**, 074 (2007) [arXiv:hep-ph/0701166]. A. L. Fitzpatrick, J. Kaplan, L. Randall and L. T. Wang, "Searching for the Kaluza-Klein graviton in bulk RS models," JHEP **0709**, 013 (2007) [arXiv:hep-ph/0701150]. B. Lillie, J. Shu and T. M. P. Tait, "Top Compositeness at the Tevatron and LHC," JHEP **0804**, 087 (2008) [arXiv:0712.3057 [hep-ph]]. T. Han, "The 'Top Priority' at the LHC," arXiv:0804.3178 [hep-ph]. Y. Bai and Z. Han, "Top-antitop and Top-top Resonances in the Dilepton Channel at the CERN LHC," arXiv:0809.4487 [hep-ph]. T. Plehn and T. M. P. Tait, "Seeking Sgluons," arXiv:0810.3919 [hep-ph].

[106] M. Staric *et al.* [Belle Collaboration], "Evidence for $D^0 - \bar{D}^0$ Mixing," Phys. Rev. Lett. **98**, 211803 (2007) [arXiv:hep-ex/0703036].

[107] C. Amsler *et al.* [Particle Data Group], "Review of particle physics," Phys. Lett. B **667**, 1 (2008).

[108] J. Pumplin, D. R. Stump, J. Huston, H. L. Lai, P. M. Nadolsky and W. K. Tung, "New generation of parton distributions with uncertainties from global QCD analysis," JHEP **0207**, 012 (2002) [arXiv:hep-ph/0201195].

[109] G. C. Cho, K. Hagiwara, J. Kanzaki, T. Plehn, D. Rainwater and T. Stelzer, "Weak boson fusion production of supersymmetric particles at the LHC," Phys. Rev. D **73**, 054002 (2006) [arXiv:hep-ph/0601063].

[110] CMS TDR: CMS Physics: Technical Design Report V.2: Physics Performance, CERN-LHCC-2006-021. ATLAS TDR: ATLAS detector and physics performance. Technical design report. Vol. 2, CERN-LHCC-99-15

Appendix A

Chapter 3 Appendices

A.1 Reconstruction

The two charged leptons in the events shown in Fig. 3.1 have momenta p_1 and p_2, respectively. We define the perpendicular momentum in the event $\vec{p}_\perp = \vec{p}_1 \times \vec{p}_2$. We refer to the pair produced unstable particles as A (for μ^-_{1R} or $\tilde{\mu}^-_R$) and B (μ^+_{1R} or $\tilde{\mu}^+_R$). The missing 4-momentum from the decay of A is $\not{p}_1$, while $\not{p}_2$ is the missing momentum from the decay of B. Both the particles escaping the detector have mass m, which is assumed to be known.

Since the pair produced particles A and B (with mass M) are back to back, it suffices to solve for p_A, as $\vec{p}_A = -\vec{p}_B$. The final-state leptons are effectively massless, so $p_1^2 = p_2^2 = 0$. For the massive particles, we have

$$p_A^2 = p_B^2 = M^2 \tag{A.1}$$
$$\not{p}_1^2 = \not{p}_2^2 = m^2. \tag{A.2}$$

Finally, since p_A (p_B) decays into $\not{p}_1$ ($\not{p}_2$) and p_1 (p_2),

$$\begin{aligned} \not{p}_1 &= p_A - p_1 \\ \not{p}_2 &= p_B - p_2. \end{aligned} \tag{A.3}$$

At the ILC, the energy of the beams E is known, and for pair production the total energy in the event must be split equally, so $p_A^0 = p_B^0 = E$. Therefore, using Eqs. (A.1), (A.2) and (A.3), we may define the following variables:

$$c_1 \equiv \vec{p}_A \cdot \vec{p}_1 = \frac{1}{2}(m^2 - M^2 + 2Ep_1^0) \tag{A.4}$$
$$c_2 \equiv \vec{p}_A \cdot \vec{p}_2 = -\frac{1}{2}(m^2 - M^2 + 2Ep_2^0) \tag{A.5}$$
$$b_2 \equiv \vec{p}_A \cdot \vec{p}_A = E^2 - M^2 \tag{A.6}$$
$$a_{ij} \equiv \vec{p}_i \cdot \vec{p}_j \ (i,j = 1,2). \tag{A.7}$$

We can write the momentum $\vec{p}_A$ as

$$\vec{p}_A = t_1\vec{p}_1 + t_2\vec{p}_2 + y\vec{p}_\perp. \tag{A.8}$$

Using this definition in Eq. (A.4) and (A.5), we find

$$\begin{aligned} c_1 &= t_1 a_{11} + t_2 a_{12} \\ c_2 &= t_1 a_{12} + t_2 a_{22} \\ t_1 &= \frac{a_{22}c_1 - a_{12}c_2}{a_{11}a_{22} - a_{12}^2} \qquad \text{(A.9)} \\ t_2 &= \frac{a_{11}c_2 - a_{12}c_1}{a_{11}a_{22} - a_{12}^2}. \qquad \text{(A.10)} \end{aligned}$$

Finally, using Eqs. (A.6), (A.9), and (A.10),

$$\begin{aligned} b_2 &= (t_1^2 a_{11} + 2t_1 t_2 a_{12} + t_2^2 a_{22}) + y|\vec{p}_\perp|^2 \\ y &= \pm\sqrt{\frac{b_2 - (t_1^2 a_{11} + 2t_1 t_2 a_{12} + t_2^2 a_{22})}{|\vec{p}_\perp|^2}}. \end{aligned} \tag{A.11}$$

The $\pm$ sign in this last equation is the two-fold ambiguity in the reconstruction.

A.2 Amplitudes

The matrix elements for right-handed smuon pair production from polarized e^-e^+ beams are

$$\begin{aligned} \mathcal{M}(e_L^- e_R^+ \to \tilde{\mu}_R^- \tilde{\mu}_R^+) &= (-ie^2)\sqrt{1 - \frac{4m_{\tilde{\mu}}^2}{s^2}}\sin\theta \times \\ &\left(1 + \frac{s(-1/2 + s_W^2)}{c_W^2(s - 4m_Z^2)}\right) \qquad \text{(A.12)} \\ \mathcal{M}(e_R^- e_L^+ \to \tilde{\mu}_R^- \tilde{\mu}_R^+) &= (-ie^2)\sqrt{1 - \frac{4m_{\tilde{\mu}}^2}{s^2}}\sin\theta \times \\ &\left(1 + \frac{s_W^2 s}{c_W^2(s - 4m_Z^2)}\right). \end{aligned}$$

Here, $\sqrt{s}$ is the center-of-mass energy and $m_{\tilde{\mu}}$ is the mass of the right-handed smuon. The angle θ is defined as in Fig. 3.2.

The decaying $\tilde{\mu}^\pm$ goes to $\mu_R^\pm$ and a right-handed $\tilde{\chi}_1^0$. We make the approximation that the neutralino is primarily bino, and so the decay matrix element is

$$\mathcal{M}(\tilde{\mu}^\pm \to \mu^\pm \tilde{\chi}_1^0) = -\sqrt{2}g'\sqrt{m_{\tilde{\mu}}^2 - m_{\tilde{\chi}}^2}. \tag{A.13}$$

Here g' is the hypercharge gauge coupling $g' = e/\cos\theta_w$. Making the narrow width approximation, the cross section for the four-body final state is simply the incoherent sum over initial helicities

$$\begin{aligned} d\sigma &= \frac{d\Phi_4}{4}\sum_{L,R}\Big|\mathcal{M}(e^-_{L/R}e^+_{R/L}\to\tilde{\mu}^-\tilde{\mu}^+)\mathcal{M}(\tilde{\mu}^-_R\to\mu^-_R\tilde{\chi}^0_1)\times \\ &\quad \mathcal{M}(\tilde{\mu}^+_R\to\mu^+_R\tilde{\chi}^0_1)\Big|^2 2\pi\delta(s_{\mu^+\tilde{\chi}^0_1}-m^2_{\tilde{\mu}})\times \\ &\quad 2\pi\delta(s_{\mu^-\tilde{\chi}^0_1}-m^2_{\tilde{\mu}})\frac{1}{(2m_{\tilde{\mu}}\Gamma)^2}, \end{aligned} \tag{A.14}$$

where Γ is the total width of the $\tilde{\mu}_{1R}$. Note the lack of dependence on ϕ_1 and ϕ_2, in accordance with Eq. (3.4).

Pair production for right-handed μ_1 requires four helicity combinations for the μ_{1R}s. Recall that KK states of the chiral muons are massive particles; as such, they can have

either helicity. Thus, the production matrix elements are

$$\begin{aligned}
\mathcal{M}(e_L^- e_R^+ \to \mu_{1R}^-(\downarrow)\mu_{1R}^+(\uparrow)) &= (ie^2)(1-\cos\theta)\times \\
&\quad \left(1+\frac{s(-1/2+s_W^2)}{c_W^2(s-m_Z^2)}\right) \\
\mathcal{M}(e_R^- e_L^+ \to \mu_{1R}^-(\downarrow)\mu_{1R}^+(\uparrow)) &= (-ie^2)(1+\cos\theta)\times \\
&\quad \left(1+\frac{s_W^2 s}{c_W^2(s-m_Z^2)}\right) \\
\mathcal{M}(e_L^- e_R^+ \to \mu_{1R}^-(\downarrow)\mu_{1R}^+(\downarrow)) &= (-ie^2)\frac{2m_{\mu_1}}{\sqrt{s}}\sin\theta \\
&\quad \left(1+\frac{s(-1/2+s_W^2)}{c_W^2(s-m_Z^2)}\right) \\
\mathcal{M}(e_R^- e_L^+ \to \mu_{1R}^-(\downarrow)\mu_{1R}^+(\downarrow)) &= (-ie^2)\frac{2m_{\mu_1}}{\sqrt{s}}\sin\theta \\
&\quad \left(1+\frac{s_W^2 s}{c_W^2(s-m_Z^2)}\right) \\
\mathcal{M}(e_L^- e_R^+ \to \mu_{1R}^-(\uparrow)\mu_{1R}^+(\downarrow)) &= (-ie^2)(1+\cos\theta)\times \\
&\quad \left(1+\frac{s(-1/2+s_W^2)}{c_W^2(s-m_Z^2)}\right) \\
\mathcal{M}(e_R^- e_L^+ \to \mu_{1R}^-(\uparrow)\mu_{1R}^+(\downarrow)) &= (ie^2)(1-\cos\theta)\times \\
&\quad \left(1+\frac{s_W^2 s}{c_W^2(s-m_Z^2)}\right) \\
\mathcal{M}(e_L^- e_R^+ \to \mu_{1R}^-(\uparrow)\mu_{1R}^+(\uparrow)) &= (ie^2)\frac{2m_{\mu_1}}{\sqrt{s}}\sin\theta \\
&\quad \left(1+\frac{s(-1/2+s_W^2)}{c_W^2(s-m_Z^2)}\right) \\
\mathcal{M}(e_R^- e_L^+ \to \mu_{1R}^-(\uparrow)\mu_{1R}^+(\uparrow)) &= (ie^2)\frac{2m_{\mu_1}}{\sqrt{s}}\sin\theta \\
&\quad \left(1+\frac{s_W^2 s}{c_W^2(s-m_Z^2)}\right).
\end{aligned} \tag{A.15}$$

Here, $\uparrow$ corresponds to right-handed helicity, while $\downarrow$ is left-handed.

In the rest frame of the decaying μ_{1R}, there are two possible helicities ($\uparrow$ and $\downarrow$) decaying to right-handed muons and three possible polarization vectors for the B_1 (ϵ_λ, $\lambda = \pm 1, 0$).

For the decay of the μ_{1R}^-, the matrix elements are

$$\begin{aligned}
\mathcal{M}(\mu_{1R}^-(\uparrow) \to \mu_R^- B_1(-1)) &= 0 \\
\mathcal{M}(\mu_{1R}^-(\uparrow) \to \mu_R^- B_1(0)) &= g' \frac{m_{\mu_1}}{m_{B_1}} \sqrt{m_{\mu_1}^2 - m_{B_1}^2} \times \\
&\quad e^{+i\phi_1/2} \cos\frac{\theta_1}{2} \\
\mathcal{M}(\mu_{1R}^-(\uparrow) \to \mu_R^- B_1(+1)) &= -\sqrt{2} g' \sqrt{m_{\mu_1}^2 - m_{B_1}^2} \times \\
&\quad e^{+i\phi_1/2} \sin\frac{\theta_1}{2} \\
\mathcal{M}(\mu_{1R}^-(\downarrow) \to \mu_R^- B_1(-1)) &= 0 \\
\mathcal{M}(\mu_{1R}^-(\downarrow) \to \mu_R^- B_1(0)) &= g' \frac{m_{\mu_1}}{m_{B_1}} \sqrt{m_{\mu_1}^2 - m_{B_1}^2} \times \\
&\quad e^{-i\phi_1/2} \sin\frac{\theta_1}{2} \\
\mathcal{M}(\mu_{1R}^-(\downarrow) \to \mu_R^- B_1(+1)) &= \sqrt{2} g' \sqrt{m_{\mu_1}^2 - m_{B_1}^2} \times \\
&\quad e^{-i\phi_1/2} \cos\frac{\theta_1}{2}.
\end{aligned} \tag{A.16}$$

We see here the dependence on the helicity of the μ_{1R} as in Eq. (3.5). Similar equations hold for the decay of μ_{1R}^+, with $\phi_1 \to \phi_2$ and $\theta_1 \to \theta_2$.

The total cross section for the event is the coherent sum over μ_{1R} helicities and the incoherent sum over the helicities h of the electrons and polarizations λ of the KK photons:

$$\begin{aligned}
d\sigma &= \frac{d\Phi_4}{4} \sum_{L,R,\lambda\lambda'} \left| \sum_{hh'} \mathcal{M}(e_{L/R}^- e_{R/L}^+ \to \mu_{1R}^-(h)\mu_{1R}^+(h')) \right. \\
&\quad \left. \mathcal{M}(\mu_{1R}^-(h) \to \mu_R^- B_1(\lambda)) \mathcal{M}(\mu_{1R}^+(h') \to \mu_R^+ B_1(\lambda')) \right|^2 \\
&\quad 2\pi\delta(s_{\mu^+ B_1} - m_{\mu_1}^2) 2\pi\delta(s_{\mu^+ B_1} - m_{\mu_1}^2) \frac{1}{(2m_{\mu_1}\Gamma)^2}.
\end{aligned} \tag{A.17}$$

Once again, Γ is the total width of μ_{1R} and there is an implied momentum conserving δ function.